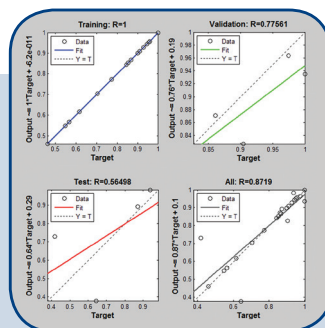
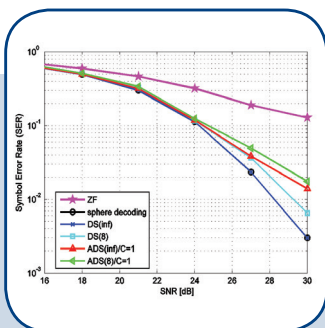
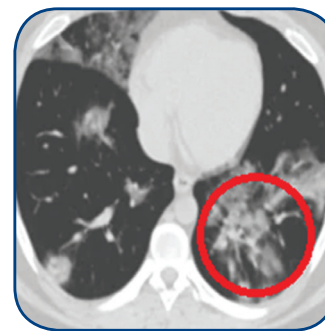
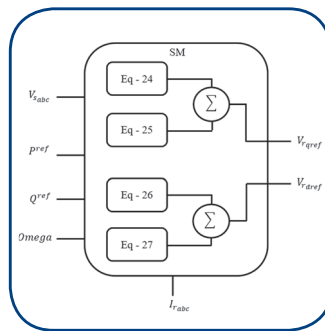
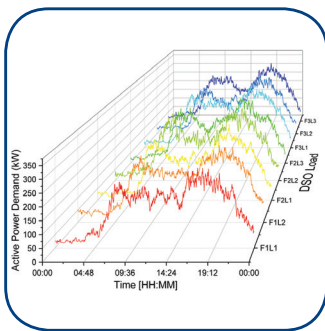


International Journal of Electrical and Computer Engineering Systems



Output Class	001	002	003	004	005	006	007	008	009	010	100%
001	3 10.0%	0 0.0%	1 3.3%	0 0.0%	0 0.0%	0 0.0%	0 0.0%	1 3.3%	0 0.0%	0 0.0%	60.0%
002	0 0.0%	3 10.0%	0 0.0%	0 0.0%	0 0.0%	0 0.0%	0 0.0%	0 0.0%	0 0.0%	0 0.0%	100%
003	0 0.0%	0 0.0%	2 6.7%	0 0.0%	0 0.0%	0 0.0%	0 0.0%	0 0.0%	0 0.0%	0 0.0%	100%
004	0 0.0%	0 0.0%	0 0.0%	3 10.0%	0 0.0%	0 0.0%	0 0.0%	0 0.0%	0 0.0%	0 0.0%	100%
005	0 0.0%	0 0.0%	0 0.0%	0 0.0%	3 10.0%	0 0.0%	0 0.0%	0 0.0%	0 0.0%	0 0.0%	100%
006	0 0.0%	0 0.0%	0 0.0%	0 0.0%	0 0.0%	10 33.3%	0 0.0%	0 0.0%	0 0.0%	0 0.0%	100%
007	0 0.0%	0 0.0%	0 0.0%	0 0.0%	0 0.0%	0 0.0%	3 10.0%	0 0.0%	0 0.0%	0 0.0%	100%
008	0 0.0%	0 0.0%	0 0.0%	0 0.0%	0 0.0%	0 0.0%	0 0.0%	2 6.7%	0 0.0%	0 0.0%	100%
009	0 0.0%	0 0.0%	0 0.0%	0 0.0%	0 0.0%	0 0.0%	0 0.0%	0 0.0%	3 10.0%	0 0.0%	100%
010	0 0.0%	0 0.0%	0 0.0%	0 0.0%	0 0.0%	0 0.0%	0 0.0%	0 0.0%	0 0.0%	10 33.3%	100%
100%	100%	100%	88.7%	100%	100%	100%	86.7%	100%	100%	83.3%	83.3%
100%	10.0%	10.0%	33.3%	10.0%	10.0%	33.3%	10.0%	10.0%	10.0%	33.3%	6.7%

INTERNATIONAL JOURNAL OF ELECTRICAL AND COMPUTER ENGINEERING SYSTEMS

Published by Faculty of Electrical Engineering, Computer Science and Information Technology Osijek,
Josip Juraj Strossmayer University of Osijek, Croatia

Osijek, Croatia | Volume 13, Number 1, 2022 | Pages 1-86

The International Journal of Electrical and Computer Engineering Systems is published with the financial support
of the Ministry of Science and Education of the Republic of Croatia

CONTACT

**International Journal of Electrical
and Computer Engineering Systems
(IJECS)**

Faculty of Electrical Engineering, Computer
Science and Information Technology Osijek,
Josip Juraj Strossmayer University of Osijek, Croatia
Kneza Trpimira 2b, 31000 Osijek, Croatia
Phone: +38531224600, Fax: +38531224605
e-mail: ijeces@ferit.hr

Subscription Information

The annual subscription rate is 50€ for individuals,
25€ for students and 150€ for libraries.
Giro account: 2390001 - 1100016777,
Croatian Postal Bank

EDITOR-IN-CHIEF

Tomislav Matić
J.J. Strossmayer University of Osijek,
Croatia

MANAGING EDITOR

Goran Martinović
J.J. Strossmayer University of Osijek,
Croatia

EXECUTIVE EDITOR

Mario Vranješ
J.J. Strossmayer University of Osijek, Croatia

ASSOCIATE EDITORS

Krešimir Fekete
J.J. Strossmayer University of Osijek, Croatia

Damir Filko
J.J. Strossmayer University of Osijek, Croatia

Davor Vinko
J.J. Strossmayer University of Osijek, Croatia

EDITORIAL BOARD

Marinko Barukčić
J.J. Strossmayer University of Osijek, Croatia

Leo Budin
University of Zagreb, Croatia

Matjaz Colnarič
University of Maribor, Slovenia

Aura Conci
Fluminense Federal University, Brazil

Bojan Čukić
West Virginia University, USA

Radu Dobrin
Malardalen University, Sweden

Irena Galić
J.J. Strossmayer University of Osijek, Croatia

Radoslav Galić
J.J. Strossmayer University of Osijek, Croatia

Ratko Grbić
J.J. Strossmayer University of Osijek, Croatia

Marijan Herceg
J.J. Strossmayer University of Osijek, Croatia

Darko Huljenić
Ericsson Nikola Tesla, Croatia

Željko Hocenski
J.J. Strossmayer University of Osijek, Croatia

Gordan Ježić
University of Zagreb, Croatia

Dražan Kozak
J.J. Strossmayer University of Osijek, Croatia

Sven Lončarić
University of Zagreb, Croatia

Tomislav Kilić
University of Split, Croatia

Ivan Maršić
Rutgers, The State University of New Jersey, USA

Kruno Miličević
J.J. Strossmayer University of Osijek, Croatia

Tomislav Mrčela
J.J. Strossmayer University of Osijek, Croatia

Srete Nikolovski
J.J. Strossmayer University of Osijek, Croatia

Davor Pavuna

Ecole Polytechnique Fédérale de
Lausanne, Switzerland

Nedjeljko Perić
University of Zagreb, Croatia

Marjan Popov
Delft University, The Netherlands

Sasikumar Punnekkat
Mälardalen University, Sweden

Chiara Ravasio
University of Bergamo, Italy

Snježana Rimac-Drlje
J.J. Strossmayer University of Osijek, Croatia

Gregor Rozinaj
Slovak University of Technology, Slovakia

Imre Rudas
Budapest Tech, Hungary

Ivan Samardžić
J.J. Strossmayer University of Osijek, Croatia

Dražen Slišković
J.J. Strossmayer University of Osijek, Croatia

Marinko Stojkov
J.J. Strossmayer University of Osijek, Croatia

Cristina Secleanu
Mälardalen University, Sweden

Siniša Srblić
University of Zagreb, Croatia

Zdenko Šimić
University of Zagreb, Croatia

Damir Šljivac
J.J. Strossmayer University of Osijek, Croatia

Domen Verber
University of Maribor, Slovenia

Dean Vučinić
Vrije Universiteit Brussel, Belgium
J.J. Strossmayer University of Osijek, Croatia

Joachim Weickert
Saarland University, Germany

Drago Žagar
J.J. Strossmayer University of Osijek, Croatia

Proofreader

Ivanka Ferčec
J.J. Strossmayer University of Osijek, Croatia

Editing and technical assistance

Davor Vrandečić
J.J. Strossmayer University of Osijek, Croatia

Stephen Ward
J.J. Strossmayer University of Osijek, Croatia

Dražan Bajer
J.J. Strossmayer University of Osijek, Croatia

Journal is referred in:

- Scopus
- Web of Science Core Collection
(Emerging Sources Citation Index - ESCI)
- Google Scholar
- CiteFactor
- Genamics
- Hrčak
- Ulrichweb
- Reaxys
- Embase
- Engineering Village

Bibliographic Information

Commenced in 2010.
ISSN: 1847-6996
e-ISSN: 1847-7003
Published: quarterly
Circulation: 300

IJECS online
<https://ijeces.ferit.hr>

Copyright

Authors of the International Journal of Electrical
and Computer Engineering Systems must transfer
copyright to the publisher in written form.

TABLE OF CONTENTS

A Vivaldi Antenna with Improved Bandwidth and Gain 1

Original Scientific Paper

Mohamed Elhefnawy | Frank Podd

Adaptive Dijkstra’s Search Algorithm for MIMO detection..... 9

Original Scientific Paper

Karima Boukari

A Lightweight Authentication Framework for Wireless Sensor Networks 19

Original Scientific Paper

Hakeem I Mhaibes | Shahnawaz Qadir

**Environmental impact estimation of ceramic tile industry
using modeling with neural networks 29**

Original Scientific Paper

Verica Hocenski | Ana Lončarić Božić | Nedjeljko Perić | Denis Klapan | Željko Hocenski

**The impact of collarette region-based
convolutional neural network for iris recognition 37**

Original Scientific Paper

Souheila Tounsi | Karima Boukari | Abdourazek Souahi

**Performance Assessment of TSO–DSO using Volt-Var Control at Smart-Inverters:
Case of Vestfold and Telemark in Norway 48**

Case Study

Victor Astapov | Sergei Trashchenkov | Francisco Gonzalez-Longatt | Danijel Topic

**Electric Energy Management for Plug-in Electric Vehicles
Charging in the Distribution System by a dual cascade scheduling algorithm 63**

Case Study

Supipat Panichtanakom | Kusumal Chalermyanont

**Comparative study of power smoothing techniques
produced by a wind energy conversion system..... 77**

Case Study

Hind Elaimani | Nouredine Elmouhi | Ahmed Essadki | Rachid Chakib

About this Journal

IJECES Copyright Transfer Form

A Vivaldi Antenna with Improved Bandwidth and Gain

Original Scientific Papers

Mohamed Elhefnawy

October 6 University,
Faculty of Engineering, Dept. of Electrical Engineering
Egypt
mmmelhefnawy.eng@o6u.edu.eg

Frank Podd

University of Manchester,
School of Electrical and Electronic Engineering
United Kingdom
frank.podd@manchester.ac.uk

Abstract – In this paper, the radiation characteristics of the conventional Vivaldi antenna are improved by proposing a novel design of a Vivaldi antenna. This proposed Vivaldi antenna is excited through three slots by using the L-probe microstrip feeder. The novel design can provide higher gain and wider bandwidth compared to that of the conventional Vivaldi antenna of the same size. The CST MWS software is used to simulate the proposed Vivaldi antenna. The measured and the simulated S-parameters were compared so that the feasibility of the proposed Vivaldi antenna was validated. The measured S-parameters show that the impedance bandwidth of the proposed Vivaldi antenna was from 1.976 to 7.728 GHz, while the measured maximum gain is 4.9 dBi at the operating frequency of 3 GHz.

Keywords: Vivaldi antenna, Ultra-Wide Band (UWB), tapered slot antenna, traveling wave antennas

1. INTRODUCTION

The Vivaldi antenna was widely studied because of its Ultra-Wide Band (UWB), high gain, end-fire beam with low side lobes, and simple structure. The Vivaldi antenna is used in many applications, such as radar systems, microwave imaging, and wireless communication systems [1, 2, 3, 4, 5, 6, 7, 8]. A tapered slot is etched onto a thin metal film on a substrate to form tapered slot antenna (TSA), the Vivaldi antenna can be classified as a TSA with an exponential taper. TSA belongs to the class of traveling wave antennas [9]. The structure of the conventional Vivaldi antenna consists of the circular slot, the rectangular slot, and the exponential tapered slot. The circular slot can tune the impedance of the antenna to be matched with that of the microstrip feed line. The Electromagnetic wave is coupled from the microstrip feed line to the exponential tapered slot line through the rectangular slot. The required value of the characteristic impedance of the rectangular slot is achieved by changing the width of this slot. This exponential tapered slot provides the guiding path for the radiating Electromagnetic wave. The bandwidth and the directivity of the Vivaldi antenna depend on the exponential function which is used to design the taper of the slot. The length of the exponential tapered slot controls the achievable bandwidth, while the maximum separation

between the conductors of the exponential tapered slot determines the lowest operating frequency. The width of the flare is increased with distance from the throat of the antenna feed. The design of the Vivaldi antenna can be divided into the propagation section and the radiation section. In the propagation section, the electromagnetic wave is propagating from feed line to the rectangular slot. The separation between the conductors of the rectangular slot is small compared to the free-space wavelength, thus the waves will not be radiated. Then the electromagnetic waves travel down the curve path of the flare along the structure of the antenna through the radiation section. In this region, the separation between the conductors is increased and waves will be radiated from the antenna. The radiation will be started when this separation is widened to the order of the free space half wavelength. A Vivaldi antenna comprising of two adjacent Vivaldi exponential tapered slots with a rotated angle of 29° between them was introduced in [5]. This Vivaldi antenna covers a frequency range from 0.7 to 2.7 GHz, and a peak gain of 8.3 dB can be obtained. In [10], a rhomboid shape for the slot cavity is selected to be used with the Vivaldi antenna. This Vivaldi antenna provides a return loss better than 10 dB in the band between 3 and 5 GHz, and maximum gain of 5 dB. An antipodal Vivaldi antenna with exponential tapered slots and slot edges was

presented in [11], this antenna operates at a frequency band from 300 MHz to 2 GHz, and can provide a maximum gain of 11.5 dBi. In [12, 13], a Vivaldi antenna with a double-slot structure was introduced to improve the gain by generating plane-like waves across the exponential tapered slot. The obtained bandwidth is from 2.5 to 15 GHz, and a maximum gain of 14.5 dB can be achieved. In [14], a Vivaldi antenna with semicircular embedment is proposed to increase the bandwidth. This Vivaldi antenna has two bands, from 2.96 to 5.05 GHz and from 5.58 to 8.52 GHz. The maximum gain of 5 dB can be obtained in the band of 2.96-5.05 GHz, while a maximum gain of about 6.5 dB can be achieved in the band of 5.58-8.52 GHz. In [15], an antipodal Vivaldi antenna with elliptically tapered radiators is presented to provide a bandwidth of 1.65-18 GHz. In this paper, the proposed novel Vivaldi antenna provides a higher

gain than that of the conventional Vivaldi antenna of the same size. The improvement of the antenna gain is achieved by using the three-slot structure, which makes the aperture field distribution in the radiation section more uniform and yields plane-like wavefronts. In addition, the use of the three-slot structure improves the matching between the microstrip feeder and the slotline so that a wider bandwidth can be achieved. The proposed Vivaldi antenna has a higher bandwidth than the obtained bandwidth in [5], [10, 11] and [14]. Also, the proposed Vivaldi antenna can reduce the antenna size by 23% and 162.3% compared to those in [12, 13] and in [15], respectively. Table 1 indicates the comparison between these different UWB Vivaldi antennas. This paper is organized as follows: Section 2 describes the antenna configuration. Section 3 presents the results and Section 4 concludes the paper.

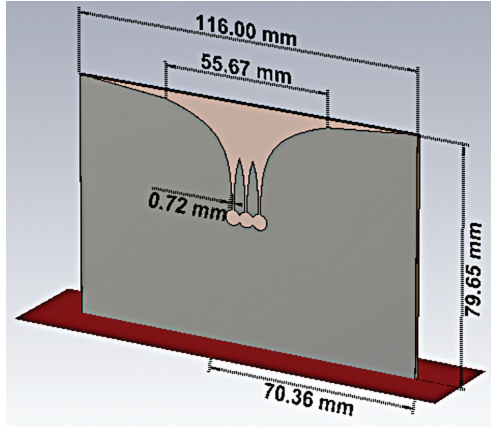
Table 1. Comparison between different UWB Vivaldi antennas.

Ref	Antenna Substrate	Antenna Size	Antenna structure	Frequency range	Max. gain
[5]	Duroid 5880 with permittivity of 2.2 and loss tangent of 0.004	260 × 254 mm ²	Vivaldi antenna with two radiation slots	0.7 - 2.7 GHz	8.3 dBi
[10]	FR4	62 × 32.5 mm ²	Tapered slot Vivaldi antenna	3 - 5 GHz	5 dBi
[11]	Rogers 4350 with permittivity of 3.48 and loss tangent of 0.004	600 × 450 mm ²	Antipodal Vivaldi antenna	0.3 - 2 GHz	11.5 dBi
[12, 13]	F4B 5880 with permittivity of 2.65 and loss tangent of 0.001	150 × 80 mm ²	Double-slot Vivaldi antenna	2.5 - 15 GHz	14.5 dBi
[14]	FR4 5880 with permittivity of 5.2 and loss tangent of 0.038	45 × 40 mm ²	Semicircular patch embedded Vivaldi antenna	Band-1: 2.96 - 5.05 GHz. Band-2: 5.58 - 8.52 GHz	6.5 dBi
[15]	RO4003C with permittivity of 3.38 and loss tangent of 0.0027	202 × 120 mm ²	Elliptically tapered antipodal Vivaldi antenna	1.65 – 18 GHz	14.2 dBi
Current work	FR4 with permittivity of 4.3 and loss tangent of 0.02	116 × 79.65 mm ²	Vivaldi antenna with three exponential tapered slots	1.976 - 7.728 GHz	4.9 dBi

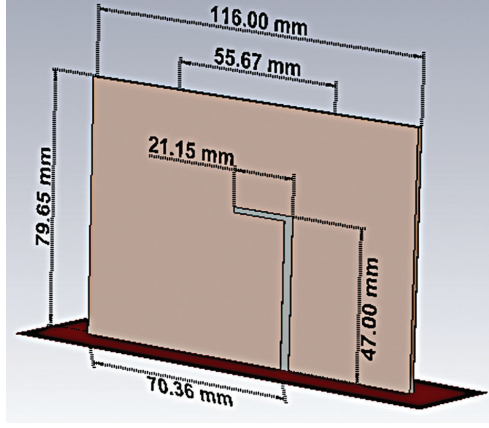
2. ANTENNA CONFIGURATION

The proposed and the conventional Vivaldi antennas are simulated in CST MWS, and their geometrical configurations are shown in Figures 1 and 2, respectively. Both the antennas have a size of 116 × 79.65 mm².

This antenna size was selected in order to get a larger mouth opening so that the value of the lowest frequency of operation can be reduced. The proposed Vivaldi antenna comprises of L-probe microstrip feed line, three circular slots, three rectangular slots and the exponential tapered slot.



(a)



(b)

Fig. 1. Geometry of the simulated proposed Vivaldi antenna (a) front view. (b) back view.

The exponential tapered slot consists of six exponential curves, where the exponential function which is used to design each of these six curves can be deduced by the following equation

$$x(y) = \pm Ae^{Ry} \quad (1)$$

Where R is the exponential taper rate, and A is a constant which was selected to be half the width of the rectangular slot. The value of the exponential tapered slot opening width (w_a) is selected to be greater than $(c/(f_c\sqrt{\epsilon_r}))$ and less than $((c(2M+1))/(2f_{min}\sqrt{\epsilon_r}))$, where M is a positive number (in this paper, $M = 1$), c is the speed of light, ϵ_r is the relative permittivity of the substrate, f_c and f_{min} are the center and the minimum frequencies, respectively [16, 17]. The width (W) and the length (L) of the Vivaldi antenna are designed based on equations (2) and (3), respectively [17]

$$W = \frac{c}{f_{min}\sqrt{\epsilon_r}} \quad (2)$$

$$L = \frac{(2N+1)\lambda_c}{2\sqrt{\epsilon_{eff}}} - 2\Delta L \quad (3)$$

$$\epsilon_{eff} = \frac{\epsilon_r+1}{2} + \frac{\epsilon_r-1}{2} \left(1 + \frac{12 \times h}{W}\right)^{-2} \quad (4)$$

$$\Delta L = 0.421 \times h \left(\frac{-0.3 - \epsilon_{eff}}{0.258 - \epsilon_{eff}} \right) \left[\frac{0.264 + \frac{W}{h}}{0.8 + \frac{W}{h}} \right] \quad (5)$$

Where h and ϵ_{eff} are the thickness and the effective permittivity of the substrate, respectively. N is a positive number (in this work, $N = 3$), λ_c is the wavelength at the center frequency and the increased distance on each end along the Vivaldi antenna is denoted by ΔL . The width of the L-probe microstrip feeder (w_m) is obtained as follow [18]

$$w_m = \frac{h \times 8 e^{H_e}}{e^{(2He)} - 2} \quad (6)$$

$$H_e = \frac{z_{om} \sqrt{2(\epsilon_r+1)}}{120} + \frac{1}{2} \left(\frac{\epsilon_r-1}{\epsilon_r+1} \right) \left[\ln \frac{\pi}{2} + \frac{1}{\epsilon_r} \ln \frac{4}{\pi} \right] \quad (7)$$

Where z_{om} is the characteristic impedance of the L-probe microstrip feeder that was selected to be 50Ω . Also the width of the rectangular slot (w_s) is determined based on the following equation [19]

$$z_{os} = 73.6 - 2.15 \epsilon_r + A + B + C - D \quad (8)$$

$$A = (638.9 - 31.37 \epsilon_r) \left(\frac{w_s}{\lambda_o} \right)^{0.6} \quad (9)$$

$$B = (36.23 \sqrt{\epsilon_r^2 + 41} - 225) \left(\frac{W/h}{\frac{W}{h} + 0.876 \epsilon_r - 2} \right) \quad (10)$$

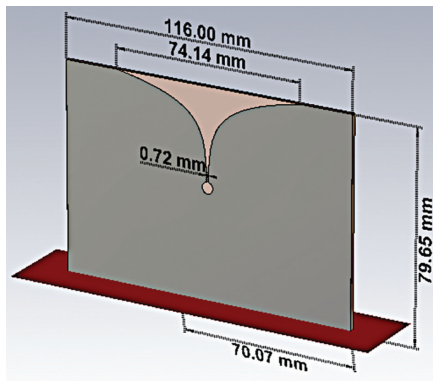
$$C = 0.51(\epsilon_r + 2.12) \left(\frac{W}{h} \right) \ln \left(\frac{100h}{\lambda_o} \right) \quad (11)$$

$$D = \frac{0.753 \epsilon_r (h/\lambda_o)}{\sqrt{w_s/\lambda_o}} \quad (12)$$

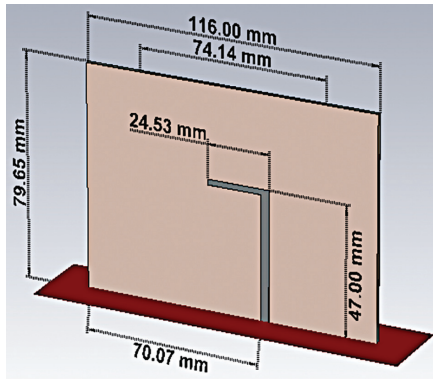
Where λ_o is the free-space wavelength, z_{os} is the characteristic impedance of the slot line. The exponential taper rate (R) can be calculated as follows [16]

$$R = 1/L_a \ln(W/w_s) \quad (13)$$

where (L_a) is the length of the exponential tapered slot length. The structure parameters of the proposed and the conventional Vivaldi antennas are listed in Table 2. The front-view of the fabricated sample of the proposed Vivaldi antenna is shown in Figure 3(a). The L-probe microstrip feeder is used to feed the three rectangular slots of the proposed Vivaldi antenna, as shown in Figure 3(b). The lowest frequency of operation is decreased as the mouth opening of the proposed Vivaldi antenna is increased and vice versa. The size of the fabricated antenna can be reduced by increasing the value of the dielectric constant. Gain of the proposed Vivaldi antenna can be increased by selecting a material with a small loss tangent. FR4 dielectric substrate was selected because of its availability and low-cost. The thickness of the FR-4 substrate is 1.6 mm, and its permittivity and loss tangent are 4.3 and 0.02, respectively. The 50Ω connector is used to feed the proposed Vivaldi antenna.

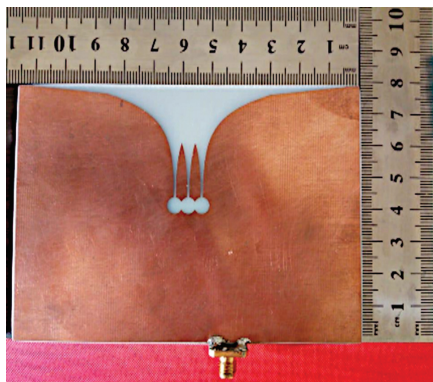


(a)

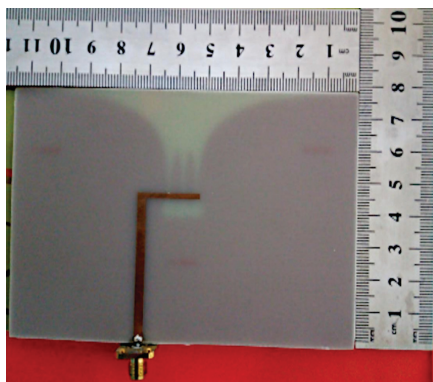


(b)

Fig. 2. Geometry of the simulated conventional Vivaldi antenna (a) front view. (b) back view.



(a)



(b)

Fig. 3. Geometrical configuration of the fabricated proposed Vivaldi antenna (a) front view. (b) back view.

Table 2. Structure parameters of the proposed and the conventional Vivaldi antennas.

Parameters	Dimensions of proposed Vivaldi antenna [mm]	Dimensions of conventional Vivaldi antenna [mm]
Antenna length (L)	116	116
Antenna width (W)	79.65	79.65
Exponential tapered slot length (La)	25	30
Exponential tapered slot opening width (wa)	55.67	74.14
Exponential Taper rate (R)	0.151825	0.151825
Rectangular slot length	5.097	4.25
Rectangular slot width (w_r)	0.72	0.72
Circular slot radius	2.5485	2.125
L-probe microstrip feeder height	47	47
L-probe microstrip feeder edge length	21.15	24.53
Width of L-probe microstrip feeder height (w_m)	2.8864	3.2
L-probe microstrip feeder edge width	1.702	2
Length from L-probe microstrip feeder to the boarder	70.36	70.07

3. RESULTS

The CST Microwave Studio software was used to simulate the proposed and the conventional Vivaldi antennas. The antenna parameters such as the S-parameters, the radiation pattern and the gain were examined over a range of frequencies 1 to 9 GHz. The Rohde & Schwarz ZVL vector network analyzer (VNA) was used to measure the fabricated prototype of the proposed Vivaldi antenna as shown in Figure 4.



Fig. 4. Measured S-parameters of the fabricated prototype of the proposed Vivaldi antenna

The structure parameters in Table 2 were used to simulate the proposed and the conventional antennas in the CST MWS simulation software. Figure 5 shows the measured and the simulated S-parameters of the proposed Vivaldi antenna, and the simulated S-parameters for the conventional Vivaldi antenna. The measured and the simulated bandwidths of the proposed Vivaldi antenna

are from 1.976 to 7.728 GHz and from 2.109 to 7.799 GHz, respectively, while the simulated bandwidth of the conventional Vivaldi antenna is from 1.651 to 6.204 GHz.

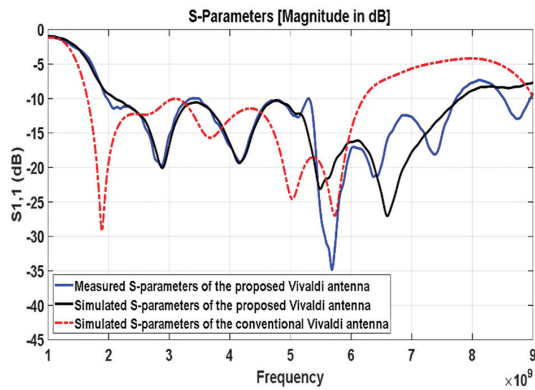


Fig. 5. Measured and simulated S-parameters of the proposed Vivaldi antenna, and simulated S-parameters for the conventional Vivaldi antenna

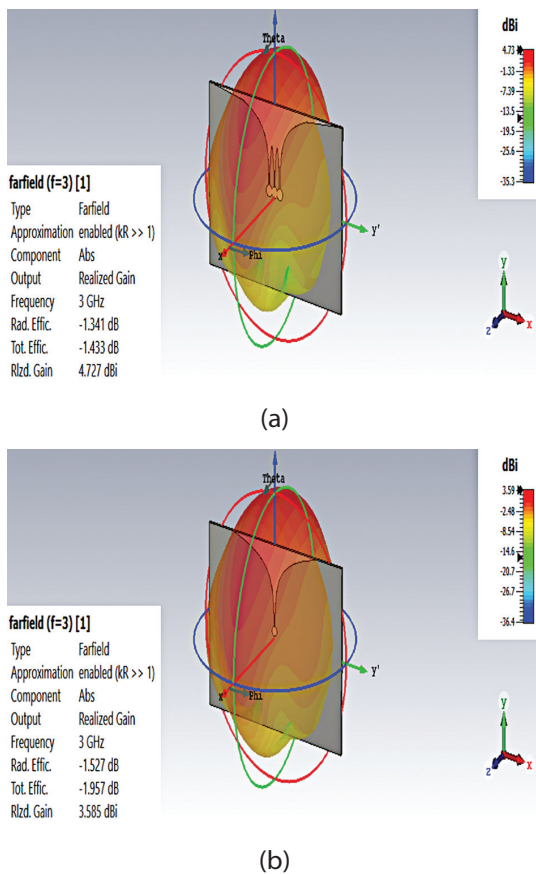


Fig. 6. 3D radiation pattern at the operating frequency of 3 GHz (a) proposed Vivaldi antennas. (b) conventional Vivaldi antenna

The 3D radiation patterns for the proposed and the conventional Vivaldi antennas at the operating frequency of 3 GHz are shown in Figure 6. The proposed Vivaldi structure can provide a radiation pattern with higher gain. Figure 7 shows the measured and the simulated antenna gain versus frequency for the proposed Vivaldi antennas, besides the simulated antenna gain versus

frequency for the conventional Vivaldi antenna. For the proposed Vivaldi antenna, the maximum measured antenna gain of 4.9 dBi is achieved at an operating frequency of 3 GHz. The measured and simulated results show that the proposed Vivaldi structure can increase the bandwidth by about 25% compared to the bandwidth of the conventional structure. Except for the frequency band from 4.7 to 5.4 GHz, the gain also can be improved by implementing the proposed Vivaldi antenna.

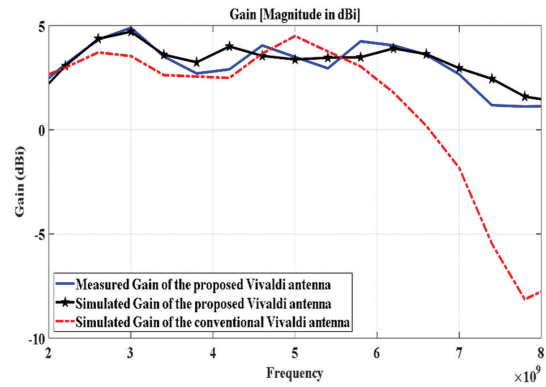


Fig. 7. Measured and simulated gain of the proposed Vivaldi antenna and simulated gain for the conventional Vivaldi antenna

Figure 8 shows that the simulated radiation efficiency is above 70% for the proposed and the conventional Vivaldi antennas within the frequency range of 2–4 GHz. The radiation efficiency of the proposed Vivaldi antenna is equal or higher than that of the conventional Vivaldi antenna, except in the frequency band of 5.1–5.6 GHz.

Figure 9 shows the simulated and the measured E- and H-plane radiation patterns for the proposed Vivaldi antenna at 4 GHz. For the simulated and measured E-plane radiation pattern, the direction of the main beam is at 40°, the HPBW of 134.3° and 120° in the simulated and the measured E-plane, respectively. The main direction at 3° is obtained in the simulated and the measured H-plane, while the HPBW of 90° and 82° are achieved within the simulated and the measured H-plane, respectively.

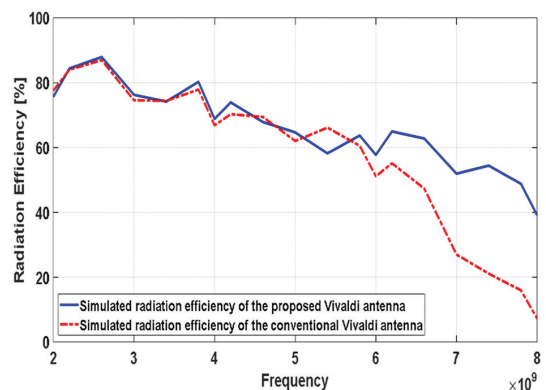


Fig. 8. The simulated radiation efficiency versus frequency for the proposed and the conventional Vivaldi antennas

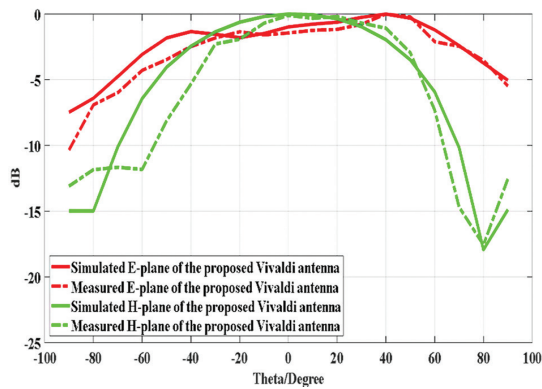


Fig. 9. Simulated and measured E- and H-plane radiation patterns of the proposed Vivaldi antenna

4. CONCLUSIONS

A Vivaldi antenna with improved gain and bandwidth is introduced in this paper. This proposed Vivaldi antenna is based on the three-slot feeding structure. The L-probe microstrip is used to excite the three rectangular slots, and the exponential tapered slot of the proposed Vivaldi antenna can generate plane-like waves rather than the spherical-like waves. This proposed Vivaldi antenna is designed based on a mathematical analysis and simulation using CST MWS. The proposed antenna structure can provide a wide bandwidth with smaller antenna size compared to other UWB Vivaldi antennas. The obtained gain is improved by using the proposed Vivaldi antenna. The simulated and the measured results show that the proposed Vivaldi antenna works well in the frequency range of 1.976 to 7.728 GHz, and its bandwidth is increased by 25% compared to the conventional Vivaldi antenna of the same size. The radiation efficiency of the proposed Vivaldi antenna is higher than that of the conventional Vivaldi antenna. Based on the measured and the simulation results, this proposed Vivaldi antenna provides a wide beamwidth. This proposed Vivaldi antenna can be an excellent candidate for many applications, such as radar and wireless communication systems.

5. REFERENCES:

- [1] W. Wiesbeck, G. Adamiuk, C. Sturm, "Basic Properties and Design Principles of UWB Antennas", *Proceedings of the IEEE*, Vol. 97, No. 2, 2009, pp. 372-385.
- [2] J. M. Felício, J. M. Bioucas-Dias, J. R. Costa, C. A. Fernandes, "Antenna Design and Near-Field Characterization for Medical Microwave Imaging Applications", *IEEE Transactions on Antennas and Propagation*, Vol. 67, No. 7, 2019, pp. 4811-4824.
- [3] Y. Yang, Y. Wang, A. E. Fathy, "Design of compact Vivaldi antenna arrays for UWB see through wall applications", *Progress In Electromagnetics Research*, Vol. 82, 2008, pp. 401-418.
- [4] D. Comite, A. Galli, I. Catapano, F. Soldovieri, "The Role of the Antenna Radiation Pattern in the Performance of a Microwave Tomographic Approach for GPR Imaging", *IEEE Journal of Selected Topics in Applied Earth Observations and Remote Sensing*, Vol. 10, No. 10, 2017, pp. 4337-4347.
- [5] Y. Dong, J. Choi, I. Catapano, T. Itoh, "Vivaldi Antenna With Pattern Diversity for 0.7 to 2.7 GHz Cellular Band Applications", *IEEE Antennas and Wireless Propagation Letters*, Vol. 17, No. 2, 2018, pp. 247-250.
- [6] E. W. Reid, L. Ortiz-Balbuena, A. Ghadiri, K. Moez, "A 324-Element Vivaldi Antenna Array for Radio Astronomy Instrumentation", *IEEE Transactions on Instrumentation and Measurement*, Vol. 61, No. 1, 2012, pp. 241-250.
- [7] R. Natarajan, M. Kanagasabai, J. V. George, "Design of an X-band Vivaldi antenna with low radar cross section", *IET Microwaves, Antennas Propagation*, Vol. 10, No. 6, 2016, pp. 651-655.
- [8] J. Schneider, M. Mrnka, J. Gamec, M. Gamcova, Z. Raida, "Vivaldi antenna for RF energy harvesting", *Radioengineering*, Vol. 25, No. 4, 2016, pp. 666-671.
- [9] J. H. Choi, T. Itoh, Z. Chen, D. Liu, H. Nakano, X. Qing, T. Zwick, "Beam-scanning leaky-wave antennas", *Handbook of antenna technologies*, Springer-Verlag, 2016, pp. 1-33.
- [10] A. Lazaro, R. Villarino, D. Girbau, "Design of tapered slot Vivaldi antenna for UWB breast cancer detection", *Microwave and Optical Technology Letters*, Vol. 53, No. 3, 2011, pp. 639-643.
- [11] G. Jiyu, T. Jisheng, Z. Qing, J. Jiao, H. Jianjian, M. Chunguang, "An ultrawide band antipodal Vivaldi antenna for airborne GPR application", *IEEE Geoscience and Remote Sensing Letters*, Vol. 16, No. 10, 2019, pp. 1560-1564.
- [12] Y. Wang, G. Wang, X. Gao, C. Zhou, "Double-slot Vivaldi antenna with improved gain", *Electronics letters*, Vol. 49, No. 18, 2013, pp. 1119-1121.
- [13] Y. Wang, G. Wang, B. F. Zong, "Directivity improvement of Vivaldi antenna using double-slot structure", *IEEE Antennas and Wireless Propagation Letters*, Vol. 12, 2013, pp. 1380-1383.

- [14] J. Seo, J. H. Kim, J. Oh, "Semicircular Patch-Embedded Vivaldi Antenna for Miniaturized UWB Radar Sensors", *Sensors*, Vol. 20, No. 21, 2020, pp. 5988.
- [15] M. Moosazadeh, S. Kharkovsky, Z. Esmati, B. Samali, "UWB elliptically-tapered antipodal Vivaldi antenna for microwave imaging applications", *Proceedings of the IEEE-APS Topical Conference on Antennas and Propagation in Wireless*, Cairns, QLD, Australia, 19-23 September 2016, pp.102-105.
- [16] A. B. Constantine, "Antenna theory: analysis and design", 4th Ed. John Wiley & Sons, 2015.
- [17] R. K. Kushwaha, P. Karuppanan, "Design and analysis of Vivaldi antenna with enhanced radiation characteristics for mm-wave and THz applications", *Optical and Quantum Electronics*, Vol. 51, No. 9, 2019, pp.1-19.
- [18] G. Fang, M. Sato, "Optimization of Vivaldi antenna for demining by GPR", *Proceedings of the International Symposium on Antennas and Propagation*, 2002, pp. 263-266.
- [19] V. Tseng, C. Y. Chang, "Linear tapered slot antenna for ultra-wideband radar sensor: Design consideration and recommendation", *Sensors*, Vol. 19, No. 5, 2019, pp.1212.

Adaptive Dijkstra's Search Algorithm for MIMO detection

Original Scientific Papers

Karima Boukari

Badji-Mokhtar University
Faculty of Engineering, Department of electronics,
Laboratory for Study and Research in Instrumentation
and Communication Annaba (LERICA),
Annaba University P.B. 12, 23000, Annaba, Algeria.
boukkarima@yahoo.fr

Abstract – Employing Maximum Likelihood (ML) algorithm for signal detection in a large-scale Multiple-Input- Multiple-Output (MIMO) system with high modulation order is a computationally expensive approach. In this paper an adaptive best first search detection algorithm is proposed. The proposed Adaptive Dijkstra's Search (ADS) algorithm exploits the resources available in the search procedure to reduce the required number of nodes to be visited in the tree. A tunable parameter is used to control the number of the best possible candidate nodes required. Unlike the conventional DS, the ADS algorithm results in signal detection with low computation complexity and quasi-optimal performance for systems under low and medium SNR regimes. Simulation results demonstrate a 25% computational complexity reduction, compared to the conventional DS.

Keywords: Adaptive Dijkstra's algorithm, Maximum likelihood (ML) decoding, multiple-input, multiple-output (MIMO) systems, tree-search detection, optimization.

1. INTRODUCTION

In multiple-input multiple-output (MIMO) communication systems, each the transmitters and receivers are equipped with many antennas which can facilitate in achieving high gains in spectral, power, and energy potency compared to standard single-input single-output (SISO) systems wherever both the transmitters and receivers have just one antenna each. As a matter of fact, the MIMO systems have the power to show multipath propagation and multipath delay unfold into a profit for the receiver. Multiple Input Multiple Output (MIMO) system [1] is one of the major technologies adopted by current wireless communication standards such as Third Generation Partnership Project Long-Term Evolution (3GPP LTE), IEEE 802.11n, IEEE 802.16e as well as IEEE 802.11ac. Moreover, MIMO techniques will be used for the next generation of wireless technology systems (i.e., 5G), by increasing the number of antennas at the base station end. Employing the MIMO technology results in an increased data rate and reliability of the communication systems [2], without compromising the bandwidth or the signal power. The key advantage of MIMO systems is the many orders of magnitude of the signal-to-noise ratio (SNR) at no additional bandwidth. However, it results in additional signal processing and computations in the receiver. At the receiver side, coming up with reliable and energy-efficient MIMO detectors is a difficult task, as a result

of the complexness of the implementation of the reception due to the interfering sub-streams. The signal detection problem refers to finding the most probable transmitted symbols based on the perfect channel state information available at the receiver and the received signal. Hence, the application of MIMO technology in real-time systems is expanded and has to be constrained with such additional computational complexity, while providing an intended quality of service (QoS) [3]. To attain a possible enhancement in data rate, the detection problem of spatially multi-plexed MIMO signals has attracted many researchers' attention in recent years. The main aim of the reported research is to optimally recover the transmitted signals with a reasonable complexity for hardware implementation. In response to that, a wide range of detection techniques has been proposed in the existing literature, [4-6]. By an exhaustive search over all the possible combinations of the transmitted signals, the Maximum likelihood (ML) detection scheme, can be argued to be the best detection technique which may not be feasible for a higher dimension of MIMO system or high modulation order [7,8].

To overcome the increasing computation complexity during detection, some techniques such as the linear detection algorithm family such as Zero-Forcing (ZF) Minimum Mean Squared Error (MMSE) [2] or the iterative detection using the Vertical Bell Laboratories

Layered Space-Time (VBLAST) technique have been proposed. Using these techniques decreases dramatically the detection complexity compared to the ML technique, but at the expense of a significant decrease in the detection performance. Sphere detectors (SD) can be represented using a tree-like structure to examine candidates nearby to an initial first guess. This first guess is used as the center point of the sphere to examine points within a small radius of this point. Sphere detectors typically have complexity sub-exponentially proportional to the constellation set size and number of antennas [9]. Optimal massive detectors such as ML or SD are considered infeasible given their high computational complexity [10].

By representing the MIMO signal detection as a tree search [11], a wide range of optimal and suboptimal techniques have been proposed in the literature with different tradeoff results between performance and complexity. The tree representation reformulates the MIMO signal detection problem to find the shortest possible branch from the top to the bottom of the tree within the optimal detection schema. Some algorithms initially based on finding the shortest path [12], are now adapted for the MIMO detection problem. These techniques can be classified into three different categories of tree search: depth-first, breadth-first and best first. In the MIMO signal detection, based on a tree search, all the proposed algorithms aimed at reducing the number of visited nodes and the total computation cost required for establishing the optimal solution [13]. Dijkstra's algorithm [14,15] reduces the number of visited nodes by maintaining a list of candidate nodes and equally search among them in the order of the best first. Despite the optimal performance obtained, the search involves visiting unnecessary nodes with equal importance to each node. Hence, the number of visited nodes and the memory requirement remain high for practical implementation of such an algorithm in systems with high modulation order.

In this paper, a new MIMO signal detection algorithm is proposed based on the best first search. The proposed algorithm is adaptive; it defines some criteria to reduce the number of the combinations to be evaluated and visits only the most likely combination to result in an optimal solution and hence, a large amount of calculation can be avoided. The proposed algorithm is an adaptive version of Dijkstra's algorithm with respect to transmit-receive antenna and modulation constellation dimension. The complexity reduction within the proposed algorithm is directly proportional to the modulation order with quasi-optimal performance in the low SNR regime.

The rest of the paper is organized as follows. Section 2 presents the system model and conventional Dijkstra's algorithm. Then, the proposed algorithm is presented in section 3. Simulation results and discussions are presented in section 4. Finally, some conclusions are given in section 5.

2. SYSTEM MODEL AND DIJKSTRA'S ALGORITHM

2.1 SYSTEM MODEL

We consider a spatial multiplexed MIMO system with N_t transmitter antennas and N_r receiver antennas with Rayleigh fading channel, the received signal vector can be expressed as:

$$y_c = H_c \times s_c + v_c \quad (1)$$

where y_c is an $(N_r \times 1)$ -dimensional vector representing the received signal and s_c is an $(N_t \times 1)$ -dimensional vector representing the transmitted signal. Its elements are drawn from a set of complex elements such as the M-QAM constellation, where M is the modulation order, H_c is an $(N_r \times N_t)$ matrix representing the channel with independent and are identically distributed (i.i.d.) Gaussian entries with zero mean and unitary variance and v_c is $(N_r \times 1)$ -dimensional vector of noise with an i.i.d. complex entries with zero mean and variance σ_n^2 . For simplicity, the numbers of transmitting and receiving antennas are assumed to be symmetrical, i.e. $N_t = N_r$, the channel state information is assumed to be known to the receiver.

The equivalent real presentation of the system (1) is defined by

$$\begin{bmatrix} \Re(y_c) \\ \Im(y_c) \end{bmatrix} = \begin{bmatrix} \Re(H_c) & -\Im(H_c) \\ \Im(H_c) & \Re(H_c) \end{bmatrix} \times \begin{bmatrix} \Re(s_c) \\ \Im(s_c) \end{bmatrix} + \begin{bmatrix} \Re(v_c) \\ \Im(v_c) \end{bmatrix}, \quad (2)$$

where $\Re(*)$ and $\Im(*)$ denote the real and imaginary parts of its elements. The equivalent real representation of the system model in (2) is presented as follows

$$y = H \times s + v, \quad (3)$$

where $y \in \mathbb{R}^n$, $s \in \mathbb{R}^m$, $H \in \mathbb{R}^{n \times m}$ and $v \in \mathbb{R}^n$ with $n=2 \times N_r$ and $m=2 \times N_t$.

2.2. MIMO DETECTION BASED ON TREE SEARCH

In the MIMO detection, the maximum likelihood ML detection achieves the optimal bit error rate performance by solving the minimization problem

$$\hat{s} = \arg \min_{s \in \Omega^m} \| y - Hs \|^2, \quad (4)$$

where Ω is the constellation in the real-valued system model, for example, in 16-QAM $\Omega = \{+3, +1, -1, -3\}$.

The ML detection makes an exhaustive search over all the candidates of "s". Hence, the complexity of the detection increases exponentially with the number of antennas and the modulation order M , making it impractical for real-time implementations.

By applying the QR decomposition on the channel matrix, expression (4) is reformulated by the equivalent expression

$$\hat{s} = \arg \min_{s \in \Omega^m} \|y - Hs\|^2, \quad (5)$$

with $P(s) = \|y' - Rs\|^2$ and $y' = Q^H y$, where Q is a unitary matrix and R is an upper triangular matrix.

Because of the upper triangular matrix R , the quantity $P(s)$ in (5) can be calculated in a recursive process as shown in (6). Thus, that is the MIMO detection is reformulated as follows:

$$P(s_k^l) = P(s_{k-1}^l) + B(s_k^l), \quad (6)$$

with $B(s_k^l) = (y_k' - \sum_{j=k}^m r_{k,j} s_j)^2$, where y_k' and s_j are the real elements of y and s respectively, and $r_{k,j}$ is the (k, j) -entry of R .

The minimization problem represented in Eq. (5) is solved by a tree search with m layer(s) as depicted in Fig. 1. Each node in Fig. 1. represents a partial candidate symbol vector s_k^l which is weighted by two metrics; path metric $P(s_k^l)$ and branch metric $B(s_k^l)$. As illustrated in Fig. 1., the tree search procedure starts from layer $l=0$, denoted with a dotted circle. It is named as a root node, which acts as a reference to calculate branch metric at layer $l=1$. Solid circled nodes and shaded-circle represent the visited nodes and the leaf nodes respectively, where an estimation of the path metric is required to make a decision on a partial candidate vector or a candidate vector. In the tree search procedure, it is expected to visit the node and expand towards the child nodes if required.

For conventional ML signal detection with such a tree search algorithm, all the possible candidate nodes are required to be visited. A final decision on the detected symbol vector is the leaf node with the smallest path metric and is referred to herein as the ML solution. The objective of the optimization is to reduce the number of visited nodes and output the ML solution.

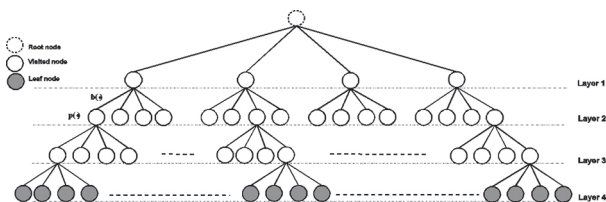


Fig. 1. Tree search for 2x 2 MIMO system with 16-QAM modulation $m=2 \times N_t$ and $\Omega = \{+3, +1, -1, -3\}$.

2.3 DIJKSTRA'S TREE SEARCH ALGORITHM:

Dijkstra's Search algorithm (DS) has been proposed initially for graph search [12]; later it has been applied to

MIMO signal detection [16-18]. As shown in Fig. 2., the conventional Dijkstra's algorithm visits all the nodes, at first layer ($l=1$), by estimating their respective path metrics; then it selects the node with the smallest path metric to be the mother node, while the rest of the nodes are the siblings. All the possible nodes expanded from the mother node at $l=2$ are considered as child nodes and their respective path metrics are calculated. In the next iteration of the search procedure, all the candidate nodes, consisting of the sibling's nodes and the new child nodes, are considered in the search of the new mother node. The new mother node is then expanded to its child nodes. This procedure continues until the selection of the mother node at the last layer $l=m$ which constitutes the detectable symbol of interest.

The DS algorithm was also proposed for systems with memory constraints [16]. In these systems, the size of the candidate nodes list is explicitly assigned and is equal to the maximum memory available to the system. The nodes with an index superior to the maximum list size are discarded. For the systems with memory constraint, a relevant of the Dijkstra's algorithm has been proposed in [19]. The algorithm limits the list of the candidate to choose from the mother node. and it is named in this paper DS(U) with U is the memory.

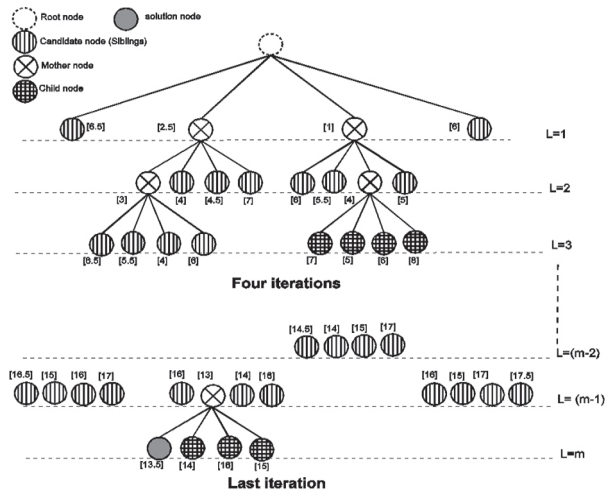


Fig. 2. Illustration of Dijkstra's search algorithm (DS) for MIMO signal detection based on tree search. The number between brackets represents the path metric $P(s_k^l)$ of the node.

Algorithm 1: DS(L)

A0. (Initialization) Given an initial node list C that contains the root node only, and node list size constraint L .

A1. (Selecting the best node) Select the first node (the best node in this iteration) from C . If this node is in layer 1, stop the algorithm and output this node as the solution.

A2. (Expanding the best node) Expand the best node by adding all its children nodes to C and removing itself from C .

A3. (Maintaining and sorting the node list) Order the nodes in C in ascending order of their path metric. Retain the first $\min(|C|, L)$ nodes and discard others. Go to A1.

3. PROPOSED ADAPTIVE DIJKSTRA'S ALGORITHM (ADS)

The computational complexity of the conventional DS algorithm is exponentially proportional to the number of nodes required to visit in the detection process. In this paper, we propose a novel candidate search that requires a lower number of nodes to be visited; subsequently, It's expected that the computational complexity is reduced. The proposed algorithm is based on an adaptation criterion to select the optimum nodes to be visited and is referred to herein as Adaptive Dijkstra's Search algorithm (ADS).

For each iteration, the ADS performs three new steps:

- **STEP 1: Defining the number of child nodes**

The degree of closeness between the path metric of the mother node and the siblings is used as a selection criterion to define the number of child nodes to be visited and it is evaluated by exploiting two estimated parameters: γ and μ calculated by

$$\gamma = \frac{P_i(3) - P_i(1)}{2}, \quad (7)$$

$$\mu = P_i(2) - P_i(1). \quad (8)$$

In the case of $\mu \geq \gamma$, the mother node is too small compared to the second smallest node in the candidate list (first sibling). It means that the current mother node and its child nodes are the most promising nodes while the siblings are less likely to lead to the ML solution. From this point of view, all the child nodes have to be visited. Otherwise ($\mu < \gamma$), the mother node is comparable to the first sibling. In this case, each sibling is also expected to be viewed as a promising node to lead to the ML solution. To enhance the possibility for the siblings to be expanded, the ADS is designed to reduce the number of child nodes that correspond to the selected mother.

The number of child nodes w to be visited is defined by:

$$w = \begin{cases} |\Omega| & \text{if } \mu \geq \gamma \\ 0.25 \times c \times |\Omega| & \text{if } \mu < \gamma \end{cases} \quad (9)$$

where $c = \{1, 2, 3\}$ is a tunable parameter used to pre-define the number of child nodes to be visited in the ADS search procedure.

- **STEP 2: Ordering the child nodes**

If the number of child nodes required to be visited is less than $|\Omega|$, only the best child nodes will be concerned. A Symbol estimator is performed using the re-

ceived signal vector, the channel state information, and the just detected signal to obtain an estimated symbol \hat{s}_k expressed in (10). The output of the estimator for the respective mother node leads towards sorting the child nodes in the order of the nearest first as presented in Fig. 3.

$$\hat{s}_k = \begin{cases} y_k / r_{k,k} \\ \left(y_k - \sum_{i=k+1}^m r_{k,i} s_i \right) / r_{k,k} \end{cases} \quad (10)$$

To avoid the additional computations of the sorting, a predefined look-up table (LUT), based on the output of the estimator, can be designed to select better/fitter child nodes.

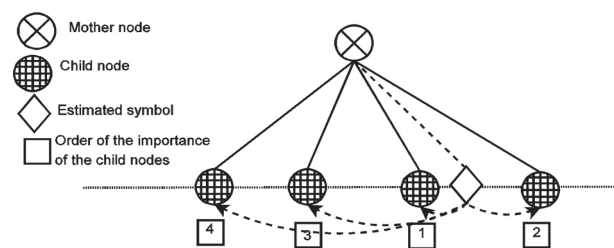


Fig. 3. Ordering the child nodes based on the estimated symbol exp: 16-QAM

- **STEP 3: Visiting the child nodes**

From the ordered child nodes, the proposed ADS algorithm visits only the w best nodes.

Fig. 4. depicts the tree expansion of ADS algorithm. In the first iteration, the number of visited child nodes is reduced to two, while it is maintained to four in the second iteration. The search continues by defining the number of child nodes in each iteration until reaching the last layer.

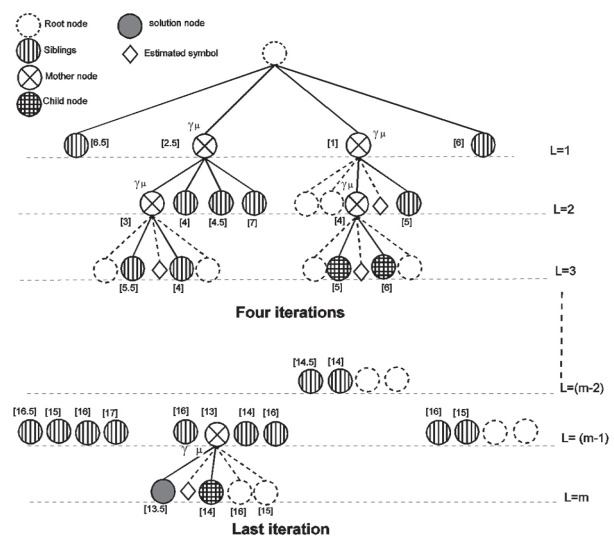


Fig. 4. Illustration of the Adaptive Dijkstra's search algorithm (ADS) for MIMO signal detection based on tree search. The number between brackets represents the path metric $P(s_k^l)$ of the node.

The proposed ADS is based on an adaptive search on each expanded node. It is more suitable for transmitted signals with high modulation order and with a given SNR, which result in an increased number of expanding nodes. Unlike the conventional DS, which visits all the child nodes, ADS visits adaptively a reduced number of child nodes. Subsequently, the ADS algorithm is expected to outperform the conventional DS algorithm in terms of computation complexity especially for systems with high modulation order.

The reduction of computational complexity due to the elimination of one child node is equal to the additional computational requirement due to the mother node expansion. In ADS algorithm, many more child nodes are more likely to be discarded by adjusting the proposed tunable parameter. Hence the reduction in computational complexity is expected to be significant compared to the conventional DS algorithm. These statements will be further demonstrated by our simulation results, presented in the following section.

Algorithm II: ADS(L)

A0–A1. Same as Algorithm I.

A2. (Defining the number of child nodes) calculate γ and μ by (7) and (8). If $\mu \geq \gamma$, then all the child nodes have to be visited. Conversely, the number of child nodes w to be visited is defined by (9).

A3. (Ordering the child nodes) an estimated symbol s_k expressed in (10) leads towards sorting the child nodes in the order of the nearest first.

A4. (Expanding the best node) Expand the best node by adding its w children nodes to C and removing itself from C .

A5. (Maintaining and sorting the node list) Order the nodes in C in ascending order of their path metric.

Retain the first $\min(|C|, L)$ nodes and discard others. Go to A1.

4. SIMULATION RESULTS AND DISCUSSIONS

4.1. EXPERIMENT DESIGN

This section aims to experimentally compare the efficiency of the proposed ADS algorithm over the conventional DS algorithm in MIMO signal detection, in terms of Symbol Error Rate (SER) performance (achieving the optimal solution for signal detection) and the associated computational complexity. MATLAB simulation environment is used to realize the simulations. Table I presents the different parameter settings for the experiments. The SER is employed to compare the performance of the systems with different signal detection schemes, while the average number of visited nodes and flops is calculated to evaluate the computational complexity.

In this experiment, a 4x4 MIMO system with 64-QAM modulation order is considered. Four detection algo-

rithms were tested on this system, ZF, SD (Sphere Detection), DS and ADS. As for the memory, two scenarios were considered for both DS and ADS algorithms ($U=1$ and $U=8$).

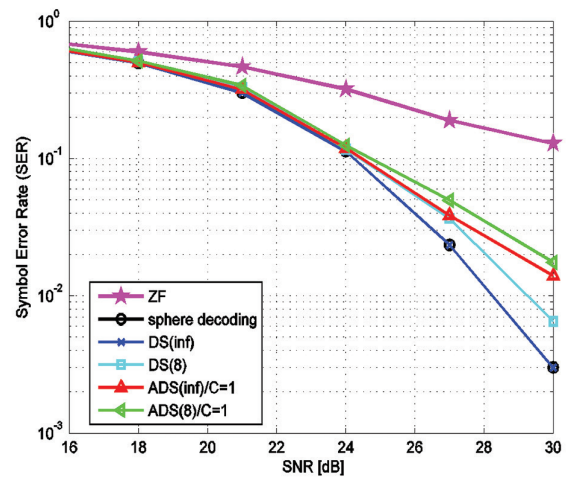
4.2. RESULTS AND DISCUSSIONS

In our study, we carried two experimentations, the first one, with $c=1$, where only 25% of nodes are visited and the second one with $c=3$, where 75% of nodes are visited.

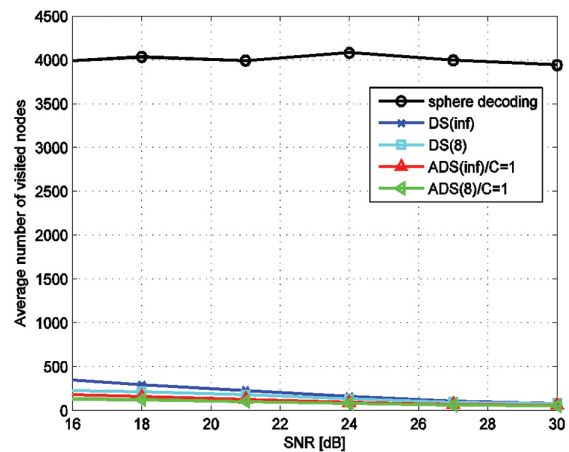
Table 1. Simulated MIMO systems

Parameters	Values
Number of transmit antennas	4
Number of receive antennas	4
Modulation order (M-QAM)	64
Tunable Parameter (c)	1 (25%), 2 (50%), 3 (75%)
Channel	Rayleigh

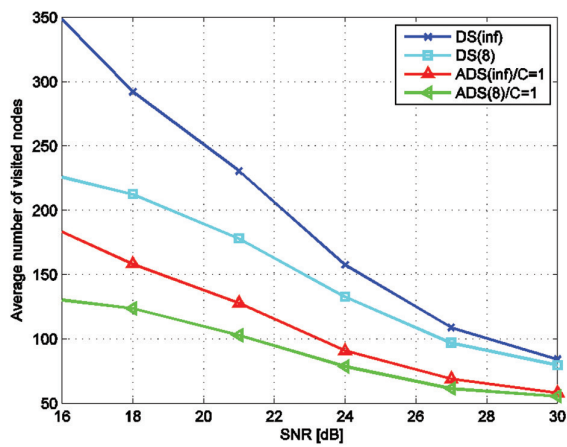
Figures 5 and 6 resume our results for $c=1$ and $c=3$ respectively. As shown in the two figures, the SD algorithm was employed to verify that the conventional DS has an optimal error performance.



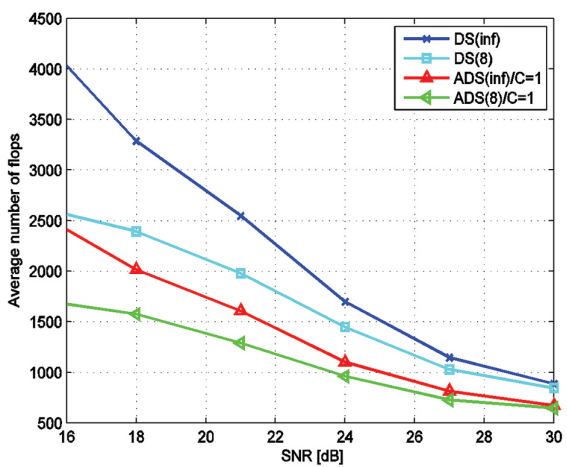
(a) SER performance



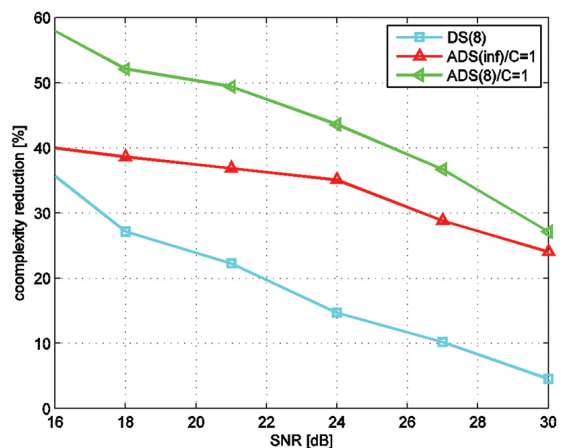
(b) Computation complexity



(c) Computation complexity (number of visited nodes)



(d) Computation complexity (number of flops)



(e) Reduction of computation complexity

Fig. 5. Performance comparison of the ADS algorithm with $c=1$ in 4×4 MIMO system and 64-QAM modulation.

• Experiment with $c=1$

It is interesting to notice that in Fig. 5-a for $\text{SNR} < 24$ dB, the performance of the conventional DS and the

proposed ADS with constrained ($U=8$) and unconstrained memory ($U=1$) is almost the same, with negligible differences. It is only when $\text{SNR} > 24$ dB that the performances of the different algorithms start to differentiate but gradually and only slightly following this sequence from best to worst: DS(1), followed by DS(8), then ADS(1), and lastly ADS(8). For $\text{SER} = 10^{-2}$, the performance of ADS(1) is degraded by about 3 dB compared to the DS(1) while the performance of ADS(8) is degraded by about 2,5 dB compared to DS(8).

As presented in Fig. 5-b, the DS(1) reduces the number of visited nodes required to achieve the best solution by an average of 4200 nodes compared to sphere decoding. Fig. 5-c and Fig. 5-d present the number of visited nodes and flops, respectively, required to output the detected signal. The four graphs follow a similar trend with a large number of visited nodes and flops for low SNR and lower for high SNR. The proposed ADS(8) has the lowest number of flops, while ADS(1) requires fewer flops than DS(8) and ADS(8).

By referring to the computational complexity of the conventional DS(1), in Fig. 5-e, the proposed ADS(1) reduces the complexity by 25% to 40% While the ADS(8) reduces the computational complexity by 20% compared to DS(8).

The optimal curves of the SER and computational complexity are presented in contrast to the curves of the SER and the number of flops of the conventional DS(1) respectively.

For low and medium SNR:

- 1) The noise affects the transmitted symbols, which appear in the tree as nodes equally probable leading to the optimal solution and their path metrics are relatively close. Therefore, a large number of nodes have to be visited as presented in Fig. 5-c. Due to the equally searching of the DS(1) algorithm, all the child nodes are visited, even the weakest nodes, for example, 350 nodes are visited for $\text{SNR} = 16$ dB.
- 2) On the contrary, the ADS(1) visits the strongest child nodes (25% in this experiment) and discards a large number of the weakest child nodes (75%). As a result, the total visited nodes is 180 for $\text{SNR} = 16$ dB.
- 3) Given a large number of the visited nodes, the probability associated with each node leading to the optimal solution has to be small, which results in a negligible SER degradation for discarding the weakest child nodes.
- 4) On the other hand, this pruning task reduces the computational cost (about 40% compared to DS(1)) by conserving the calculations of the path metrics of the discarded child nodes.

For the memory constraint, the ADS inherits also the behavior of the conventional DS. The ADS(8) has the same SER performance as DS(8) while reducing the computations by 21%.

For high SNR:

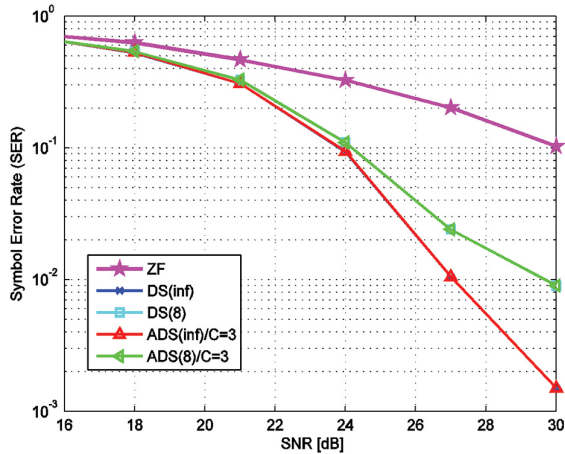
- 1) The degraded performance of the ADS(1) compared to the DS(1) is caused by discarding the child nodes. Knowing that the mother node in this region of SNR is the most likely to end to the ML solution, reducing the number of its child nodes enhances the probability to discard the optimal solution. As a result, a high degradation of SER performance is observed where 75% of child nodes are discarded.

It is important to note that in cases when SNR is less

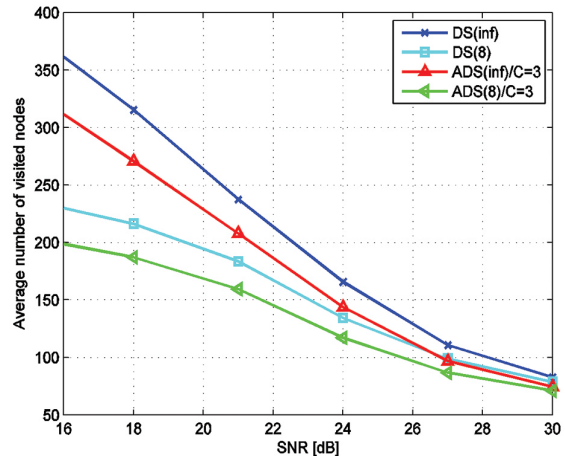
than 24 dB, visiting only 25% of child nodes, ADS(1) with $c=1$, seems to be sufficient to outperform the DS(1) with quasi-optimal performance as well as a significant reduction of computation complexity by up to 40% observed.

- **Experiment with $c=3$**

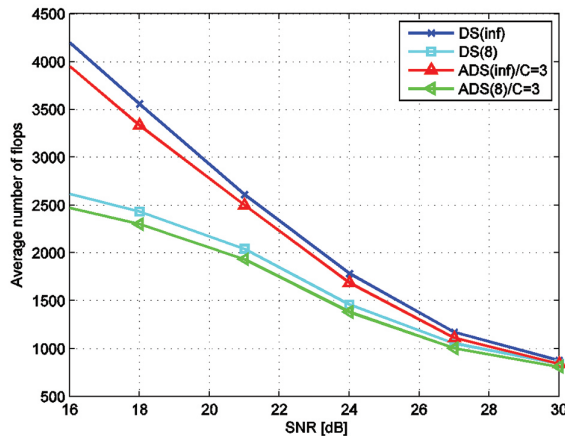
In Fig. 6, the SER performance and the computation complexity are calculated for the ADS algorithm with $c=3$ (75% of child nodes are visited).



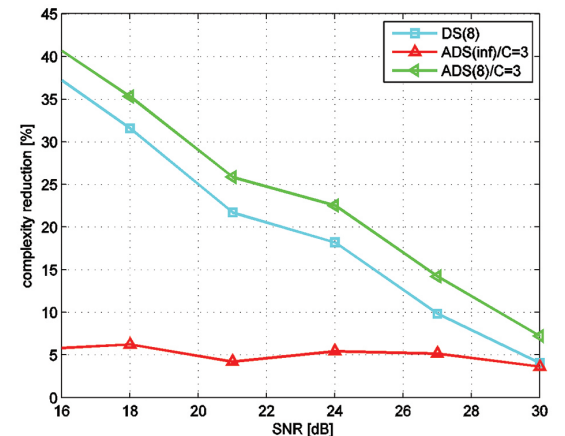
(a) SER performance



(b) Computation complexity (number of visited nodes)



(c) Computation complexity (number of flops)



(d) Reduction of computation complexity

Fig. 6. Performance comparison of the ADS algorithm with $c=3$ in 4x4 MIMO system and 64-QAM modulation.

As presented in Fig. 6-a, both the performances of ADS(1) and ADS(8) are the same as the performances of DS(1) and DS(8), respectively, across all SNR levels. Fig. 6-b and Fig. 6-c present the number of visited nodes and flops, respectively, required to output the detected signal. The two graphs follow a similar trend with a large number of visited nodes and flops for low SNR and lower for high SNR. As an example, let's compare the number of nodes for $c=1$ it goes from 350 (for DS(1)) to 180 (for ADS(1)), while for $c=3$ it changes from 360 (for DS(1)) to 320 (for ADS(1)). As expected, the spread is smaller for the number of nodes and for the flops. Hence the reduction in computational complexity is less significant. As

presented in Fig. 6-d, The complexity reduction is about 5% for both ADS(1) and ADS(8) compared to DS(1) and DS(8), respectively. In summary, visiting 75% of the best child nodes conserves the optimality of the DS(1) algorithm and reduces its complexity by 5%.

5. CONCLUSION

Due to the growing interest in large-scale MIMO systems for the future generation of wireless communication systems, the reduction of the computational complexity within ML detection schemes has been addressed in this paper. A tunable adaptation param-

eter has been introduced while attaining the intended application-specific quality of service (QoS) as a trade-off with computational complexity. More specifically, a novel tree search procedure has been proposed. The simulation results have been fairly consistent with the theoretical expectations and shows the potential superiority of the proposed ADS over the conventional DS. For real-world applications, the MIMO systems operate in low to medium SNR; where the proposed ADS proved to outperform the conventional DS. In this case, the results show that searching only 25% of the child nodes is sufficient to achieve an acceptable quasi-optimal solution, resulting in a computational complexity reduction of up to 40%. For high SNR regions, such reduction in computational complexity is attained at a minimum cost of additional SNR. However, in the case of 75% of the tree search, the ADS outperforms the conventional DS across all SNR levels, yet again with some reduction in computational complexity. Adaptation of the dynamic modulation resolution as well as dynamic selectivity of active antennas within large scale MIMO system potential focus to attain an intended QoS consistently using the proposed detection scheme. This work focuses on the uncoded MIMO systems. It will also be interesting to adapt this work in the coded MIMO systems in the category of the soft MIMO detection algorithms. These algorithms are based on iterative detection by using the information of channel decoder. Such integration can be investigated to maximize the benefits of the MIMO systems.

In addition, even if the algorithms derived in this paper do not consider OFDM modulated techniques as an option. it may be included in future works. Finally, it's worth noting that any novel detection algorithm, that do not use the heuristic weight, is of great interest.

6. REFERENCES:

- [1] A. Paulraj, D. Gore, R. Nabar, H. Bolcskei, "An overview of mimo communications - a key to gigabit wireless", *Proceedings of the IEEE*, Vol. 92, No. 2, 2004, pp. 198–218.
- [2] F. Rusek, D. Persson, B. K. Lau, E. G. Larsson, T. L. Marzetta, challenges with very large arrays", *IEEE Signal Processing Magazine*, Vol. 30, No. 1, 2013, pp. 40–60.
- [3] S. Yang, L. Hanzo, "Fifty years of MIMO detection: The road to large-scale MIMOs", *IEEE Communications Surveys and Tutorials*, Vol. 17, No. 4, 2015, pp. 1941–1988.
- [4] F. Jiang, C. Li, Z. Gong, "Low Complexity and Fast Processing Algorithms for V2I Massive MIMO Uplink Detection," *IEEE Transactions on Vehicular Technology*, 2018, pp.1–15.
- [5] J. Zeng, J. Lin, Z. Wang, "Low Complexity Message Passing Detection Algorithms for Large-Scale MIMO Systems", *IEEE Wireless Communications Letters*, 2018, pp. 1–4.
- [6] S. Wu et al, "Low-Complexity Iterative Detection for Large-Scale Multiuser MIMO-OFDM Systems Using Approximate Message Passing", *IEEE Journal of Selected Topics in Signal Processing*, Vol. 8, No. 5, 2014, pp. 902–915.
- [7] X. Zhu and R. Murch, "Performance analysis of maximum likelihood detection in a mimo antenna system", *Communications, IEEE Transactions on*, Vol. 50, No. 2, 2002, pp. 187–191.
- [8] M.-O. Damen, H. El-Gamal, G. Caire, "On maximum likelihood detection and the search for the closest lattice point", *IEEE Transactions on Information Theory*, Vol. 49, No. 10, 2003, pp. 2389–2402.
- [9] G. Romano, D. Ciuonzo, P. SalvoRossi, F. Palmieri, "Low-complexity dominance-based sphere decoder for MIMO systems", *Signal processing*, Vol. 93, No. 9, 2013, pp. 2500–2509.
- [10] B. Trotobas, A. Nafkha, Y. Louët, "A review to massive MIMO detection algorithms: Theory and implementation", *Advanced Radio Frequency Antennas for Modern Communication and Medical Systems*, IntechOpen, London, UK, 2020.
- [11] E. Larsson, "Mimo detection methods: How they work", *IEEE Signal Processing Magazine*, Vol. 26, No. 3, 2009, pp. 91–95.
- [12] E. W. Dijkstra, "A note on two problems in connexion with graphs", *Numerische mathematik*, Vol. 1, No. 1, 1959, pp. 269–271.
- [13] T. Datta, N. Srinidhi, A. Chockalingam, B. S. Rajan, "Random-restart reactive tabu search algorithm for detection in large-MIMO systems", *IEEE Communications Letters*, Vol.14, No. 12, 2010, pp.1107–1109.
- [14] K. Su, "Efficient maximum likelihood detection for communication over multiple input multiple output channels", *Department of Engineering, University of Cambridge*, 2005.
- [15] T. Fukatani, R. Matsumoto, T. Uyematsu, "Two methods for decreasing the computational complexity of the mimo ml decoder", *IEICE Transac-*

tions on Fundamentals of Electronics, Communications and Computer Sciences, Vol. 87, No. 10, 2004, pp. 2571–2576.

- [16] A. Okawado, R. Matsumoto, T. Uyematsu, “Near ml detection using dijkstra’s algorithm with bounded list size over mimo channels”, Proceedings of the IEEE International Symposium on Information Theory, Toronto, ON, Canada, 6-11 July 2008, pp. 2022–2025.
- [17] R. Chang, W.-H. Chung, “Best-first tree search with probabilistic node ordering for mimo detection: Generalization and performance-complexity tradeoff”, Wireless Communications, IEEE Transactions on, Vol. 11, No. 2, 2012, pp. 780–789.
- [18] T.-H. Kim, I.-C. Park, “High-throughput and area-efficient mimo symbol detection based on modified dijkstra’s search”, IEEE Transactions on Circuits and Systems I: Regular Papers, Vol. 57, No. 7, 2010, pp. 1756–1766.
- [19] W. Hou, T. Fujino, T. Kojima, “Adaptive candidate selection scheme in qrm-ml algorithm for mimo detection”, Proceedings of the IEEE 8th International Conference on Wireless and Mobile Computing, Networking and Communications, Barcelona, Spain, 8-10 October 2012, pp. 502–506.

A Lightweight Authentication Framework for Wireless Sensor Networks

Original Scientific Paper

Hakeem I Mhaibes

Middle Technical University,
Kut Technical Institute, Computer Center
Kut, Wassit, Iraq
hakeem.emade@mtu.edu.iq

Shahnawaz Qadir

University of Kashmir,
IT Department
Hazratbal, Srinagar, J & k, India
sqadir@uok.edu.in

Abstract – *Wireless Sensor Network (WSN) is emerging as a dominant technology with its applications in areas like agriculture, communication, environment monitoring, and surveillance. The inherited vulnerability and resource-constrained nature of sensor nodes led researchers to propose many lightweight cryptographic protocols for WSN. These sensors are low-cost, low energy, have low processing capability and have low storage restrictions. WSN suffers from many risks because of these unique constraints. This paper proposes a new lightweight security framework for WSNs and covers different lightweight cryptographic schemes for WSN applications. The aim is to provide cryptographic primitives for integrity, confidentiality, and protection from the man-in-the-middle and replay attacks. The work is based solely on symmetric cryptography and it has four phases; Network Initialization, Node Initialization, Nodes Communication, and Node Authentication. This work adopts the Low-Energy Adaptive Clustering Hierarchy (LEACH) framework, which deploys random rotation to distribute the energy among a group of nodes. The probability of attacking in LEACH is higher at cluster head and member nodes. Therefore, data transmission among communicated nodes is encrypted over multiple levels of protection by dynamic session keys to provide a high level of security. In addition, an authentication ticket is provided by a cluster head for each authenticated node to identify another node. The session keys are dynamically generated and updated during the communication to prevent compromising or capturing the keys. Through simulation and evaluation of the system, the results showed less energy consumption and efficient cryptographic primitive were compared with existing schemes.*

Keywords: Information Security, Lightweight Cryptography, Key Management, WSN, LEACH, Mutual Authentication

1. INTRODUCTION

In recent years, WSN applications have become well-known modern technologies and developed rapidly. Applications such as home automation [1], smart cities [2], healthcare applications, RFID tags [3], and sensor networks [4] led many companies to shift from general-purpose devices to resource-constrained devices [5].

WSN consists of numerous sensor nodes arranged in an organized manner called a cluster. Sensors collect information from the environment which may include buildings, people, transportation pathways, electrical lines, weather, health care etc. Highly confidential information is collected by these sensors and passed on through insecure channels for emergency response [6] and decision making.

In General, these sensors are low-cost and low energy, besides having low processing capability, communication restriction and storage restriction. Meanwhile, complex conventional computational data encryption and public-key cryptography systems are not applicable over WSNs due to these limitations [7].

Theoretically, these sensors may expose to multiple attacks (such as eavesdropping, interception, modification, and tampering) due to the nature of their deployment and the communication mode. Therefore, the probability of an attack is higher at WSN nodes [8].

Authentication can be efficiently used to verify identity of nodes in order to ensure that only authorized nodes have access to the data. In most cases, external and non-authenticated nodes could access secure data

[9], and hence, may be alter data and threaten data security. Therefore, it is necessary to build a secure WSN system to keep data secure from access violation and unauthorized access [10].

In this regard, the inherited vulnerability and resource-constrained nature of sensor nodes led researchers to propose many lightweight cryptographic protocols for WSN [11], [12], [13], [14].

The security schemes and algorithms for WSN are mainly focused on in this paper, to design and develop a new lightweight authentication framework (LWAF) that has an effective authentication and key management scheme with low computing and energy cost. This work adopts the Low-Energy Adaptive Clustering Hierarchy (LEACH) which deploys random rotation to distribute the energy among a group of nodes [15] and is based solely on symmetric cryptography [16]. The objective of key management is to dynamically establish and maintain secure channels among communicating sensors.

The symbols used in this paper illustrated in table (1).

Table 1. Notation Symbol Table

Notations	Description
BS, CH	Base Station, Cluster Head
K_M	Master key
CK^R	Cluster key for round R
C_{id}	Cluster id
N	Number of nodes
id	Node id
r	Random number
SK_{AB}	Session key between node A and B
t	timestamp
K_{id}	Symmetric key between CH and a node
$[1]_K$	Encrypted message M with K
$[M]$	Hash of message M
$[M]^j$	Message M is hashed j times

The above notations are used as scientific convention texts for illustration in this paper for node-to-node agreement description.

2. LITERATURE REVIEW AND PROBLEM STATEMENT

This paper presents the results of many existing cryptographic WSN schemes that have been done to secure WSNs.

Authors in [17] propose Localized Combinatorial Keying (LOCK) which is dynamic key management (Exclusion-Based Systems (EBS)) for cluster-based WSN. LOCK uses three keys; administrative key, group session key and cluster session key. LOCK selects a special node as a keys generator. LOCK is suitable for static networks only, whereas, the proposed LWAF is intended for dynamic networks.

Paper [18] presents a WSN protocol that is capable to prevent Denial of Service (DoS) and replay attacks. Their scheme is based on symmetric cryptography, where the sensor nodes shared a common secret key. Any compromised node can threaten the network and can send forged data.

SPINS proposed by authors in [19], which has two security protocols, SNEP and TESLA. Where, SNEP is responsible for authentication, confidentiality, evidence for data, the TESLA is responsible to provide authentication to broadcast fresh data to many nodes in the local cluster. In this scheme, the mobility of nodes leads to a topology change in a random way, that affects the security of the WSN application. This paper adopts symmetric cryptography exchange protocol and HMAC algorithm to authenticate sensor mobility in the network.

Authors in [20] considered DoS attack among multihop data transmission paths. In General, WSN is a tree structure, therefore, an attack on the node path affects the connected branches. They proposed a one-way hash chain (OHC) mechanism to prevent the connected paths and also a secure end-to-end communication of multihop data transmission path by adding a number to OHC to each transmitted message. Therefore, 8 bytes are added that cause an extra overhead on the resources-constrained devices.

Authors in [21] proposed BROadcast Session Key (BROSK) which is established through third party entities and thus lacks trust. This scheme is considered as an adhoc management scheme, where a specific node can communicate with a neighbor node for exchanging a session key. BROSK consumes less energy power by reducing data transmission as compared with SPINS.

Paper [22] developed a protocol to prevent replay attacks by maintaining a monotonical increment counter to keep track of all previous replayed messages. Here, each node has a counter that stores time information. This mechanism requires a huge amount of memory for memory-constrained sensor nodes.

Authors in [23] proposed AKMS, which consists of three phases; a key pre-distribution phase, a network initialization phase, and an authentication phase. AKMS solves the problem of malicious nodes that attack nodes during their transmission processes. The keys are dynamically generated and updated during the network communications to provide more protection and at the same time, it provides the ability for a new node to authenticate and enter into the cluster.

Authors in [24] proposed a key agreement protocol to protect a server from DoS attacks in a hierarchical WSN. In the protocol, the first level hierarchy is made by BS, the second level hierarchy is made by CHs and the third level is made by MNs. Each node in this scheme has its own built-in key used for key generation. The scheme uses timestamp with each mutual authentication and provides node authentication among hierarchy levels. Although the researchers provide node authentication, but other security primitives are not considered.

Meanwhile, battery, communication bandwidth, computation complexities and memory constraints are major concerns in WSN. Therefore, providing security and authentication for these applications is crucial in open channel communications [25]. Authentication can be efficiently used to check reliable, fake and altered communication. In most cases, the external and non-authenticated nodes are interested in the data collected by the sensor node [9]. If these nodes access the data, its integrity and confidentiality can be compromised. Thus, it is necessary to stop data violation and unauthorized access [10]. Many other lightweight cryptographic schemes are proposed to overcome these limitations [26] [27].

3. THE AIM AND OBJECTIVES OF THE STUDY

The study is aimed at providing cryptographic primitives such as integrity, confidentiality and protection from the man-in-the-middle and reply attacks for WSN applications and emphasizes on CH selections to save node battery and make the network more reliable.

To achieve this, the following objectives need to be accomplished:

- Develop a lightweight authentication framework (LWAF), where the secret messages are encrypted by session keys to provide a high level of security. These session keys are dynamically generated and updated during the communication between nodes to prevent compromising or capturing the keys.
- Generate and use an authentication ticket provided by a CH to authenticate every node in the cluster. These tickets are used by a node to identify another node in the cluster.
- Adopt LEACH framework for dynamic WSN, in which the energy is distributed in an equal manner for all connected nodes in the cluster setup to focus on CH selection in order to save energy.

4. MATERIALS AND METHODS

In the proposed LWAF, a BS node can be located far away from the rest of the homogeneous nodes. In Fig. 1, the framework architecture of the proposed scheme is illustrated. The nodes are arranged in groups called clusters, where a specific node is selected as a controller node (CH) based on certain probabilities. The rest of the nodes are called member nodes (MNs) that send data to a corresponding CH, where a CH forwards data to the BS. Here, CH is responsible for the registration of MNs. We employ LEACH framework; the implementation of LEACH can reduce energy up to 8 factors when compared with traditional routing schemes.

Features of LEACH:

- Coordination and control for cluster set-up are done locally.
- Base stations or cluster heads are selected randomly.

- Data is compressed locally to reduce the amount of transmitted data [6].

Clustering is useful in WSN whereas the data travel small distances between the surrounding nodes in the same cluster. In addition, a node can determine the nearest CH and joins the cluster to reduce the amount of energy for data transmission. See Fig. 2.

In general, selecting a node as a CH in WSN applications drains its battery. But with LEACH framework, it dynamically spreads this energy over multiple nodes in the cluster, therefore, the CH nodes are not fixed and self-selected at different time intervals. For example, at time t_1 , a group of nodes might select themselves as cluster-heads and at t_2 a new group of nodes selects themselves as another cluster-heads.

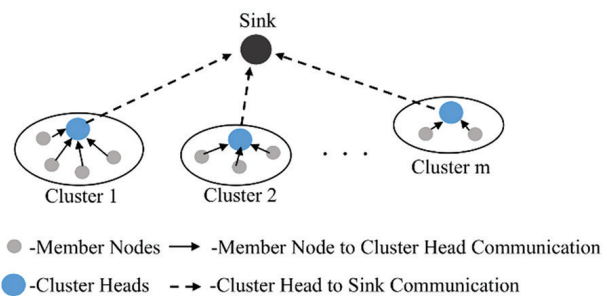


Fig. 1. WSN framework

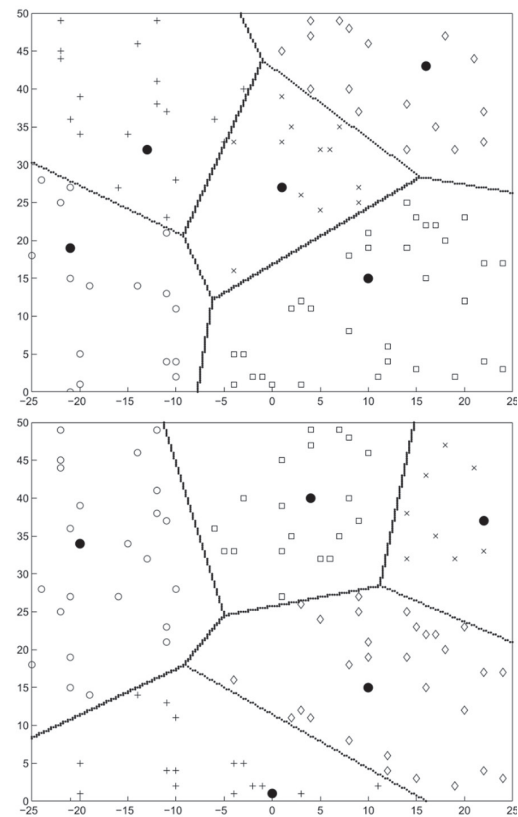


Fig. 2. Clustering in WSN: a - Group of nodes selected themselves as a CHs at time t_1 ; b - Group of nodes selected themselves as a CHs at time t_2 . CH node is marked with a •, and all given symbol belong to same CH [6]

4.1. RESEARCH MATERIAL AND SIMULATION TOOLS

In this work, MATLAB (R2020a) was used as a software platform on Windows 10. Complete WSN system was built using MATLAB/Simulink software. The simulation process consists of building the nodes hardware architecture, model the communication channel, and receive master node architecture to analyze and evaluate the proposed LWAF. Bluetooth is used as a backbone to undertake communication of the physical layer. Bluetooth technology operates in a short-range radio with 2.4 GHz. The clustering techniques of this scheme are based on LEACH framework. The encryption class used in this scheme is based on symmetric cryptography only.

4.2. METHODS OF THE PROPOSED SCHEME

The general architecture of the proposed LWAF scheme includes four phases as given below:

4.2.1 Network Initialization Phase

This phase is enabled during network deployment, where each CH is selected and registered in the network. This phase assumes each node stores a master key K_M and it has to be long enough to tolerate against crack. This master key is 128 bits and is stored securely. At firsts, Round $R=0$;

A BS node starts to select n of CH 's depending on their battery lifetime and positions and marks it with a unique number CH_n .

1. Each CH Sends a message to its BS separately, including the number of its node N and a cluster identity Cid , which is encrypted by a common master key.

$$\{C_{id}, N\}_{k_M}$$

BS now, received the encrypted message separately and uses k_M to decrypt them and generate a cluster key CK^R by hashing $CK^R=[C_{id}, K_M, N]$ and send back to each individual CH an encrypted message containing its id and a private message encrypted by a corresponding cluster key CK^R .

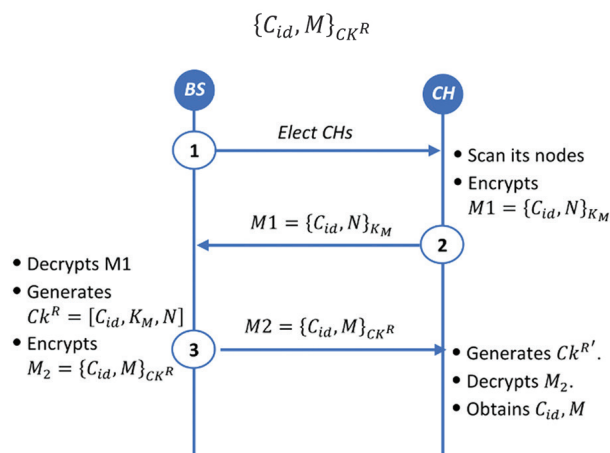


Fig. 3. Network initialization Phase.

2. Each corresponding CH receives an individual encrypt message from BS and uses its information to generate its cluster key. Then it decrypts the incoming message and checks the integrity of its identity and a common master key with a saved key. If it is equal, then the CH start a deployment process and the first phase is done, otherwise it cancels. Fig. 3. illustrates the whole processes of information exchange in this phase.

4.2.2. Node Initialization Phase

This phase is enabled when a node registers itself into the cluster.

1. For each node in the cluster;
 - Every node sends a requested message to its CH, this message contains a random number and its identity encrypted by a common master key such as:

$$\{r_i, id\}_{k_M}$$

2. After receiving message by a CH;
 - It decrypts the incoming message and obtains node identity and a random number.
 - Generates a corresponding node key k_{id} by using a hash function of a requested message and a node id such as

$$k_{id} = [r_i, id].$$

- And then encrypts two messages, the first encrypted message contains the round number, number of nodes, a cluster id and a cluster key which is encrypted by a corresponding key node such as

$$\{R, N, C_{id}, CK^R\}_{k_{id}}$$

- The second encrypted message is a ticket T_{id} . This message contains the node's identity and is used to identify another node. This ticket is encrypted by its cluster key

$$\{Nodes\ identity\}_{CK^R}$$

These messages are sent back to the requesting node.

3. When a specific node received the incoming two messages, it does the following:
 - Generates a corresponding key node k'_{id} using the same hash function and checks the validity.
 - If it is equal, then it proceeds and decrypts the first message and obtains R, N, C_{id} and CK^R .
 - It uses the cluster key to decrypts the authentication ticket and obtains node's identities.
4. At this stage, each node stores other nodes identities, R, CK^R, N, Cid and its kid and can communicate with other nodes in specified cluster.

- After all nodes have been registered and authenticated. Now $R=2$, this means the authentication transmits to next round by hashing CKR and sets $R=R+1$, such as:

$$CK^{R+1} = [CK^R]$$

This obtained key is used for the next authentication round. See fig. 4.

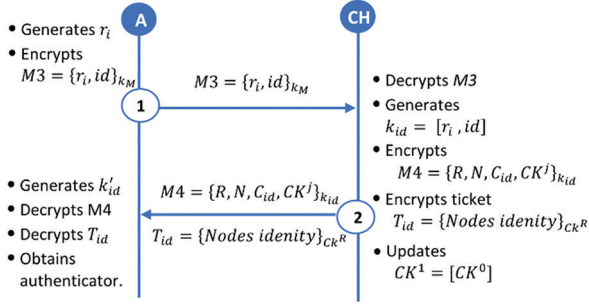


Fig. 4. Node Initialization Phase.

4.2.3 Node Communication Phase

At this stage, each node can find its neighbor and communicate within a safe mode. Mutual authentication protocol and specific excitation/response processes performed as follows:

- If a node, A, wants to communicate with a node B, then a specific operation will perform:
 - Node A generates a common session key with B by hashing its identity, B's identity, and a common C_{id} . This key used to encrypt their further messages. $sk_{AB} = [C_{id}, A, B]$.
 - Generate a nonce and encrypts $M_5 = \{r_i\}_{sk_{AB}}$
 - Send an encrypted message (A, M_5) to B.
 - An attacker wanting to listen to the date being transmitted will get encrypted values.
- When receiving a message from A, B performs the following operations:
 - Checks the identity of A.
 - If A exists, it generates the corresponding common session key using its common information to obtain sk_{AB} .
 - And, it decrypts the $\{r_i\}_{sk_{AB}}$ and obtain a nonce.
 - Then, it encrypts response M_6 , which includes a nonce and timestamp $M_6 = \{r_i, t_1\}_{sk_{AB}}$. This timestamp is used for mutual authentication.
 - Then, B sends M_6 to A.

After receiving M_6 , node A will perform:

- Decrypts M_6 .
- And checks its random number and the timestamp with a specific limit. If the current time

$$t_{(curr)} - t_1 \leq \Delta t, \text{ otherwise stop the connection.}$$

Now, each node can communicate with their neighbor nodes through their common session key.

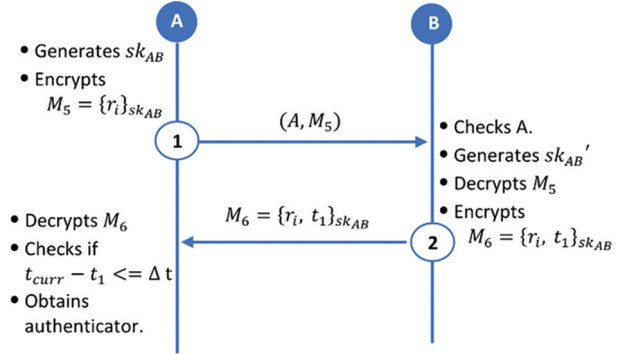


Fig. 5. Nodes Communication Phase.

4.2.4. Node Authentication Phase.

This phase is employed when a new node wants to join a network. Nodes use the authenticated ticket to authenticate and verify a new node. A pre-calculation for excitation/response based on mutual authentication protocol is done to avoid a situation of storing a common cluster key in the internal memory because keeping a common cluster key could face the network to a serious problem. Therefore, the LWAF suggests that a new node is verified using knowledge of the common master key of previous round R. Such that, the authentication of round 2, is constructed using a key derivation of round 1 without storing the previous key.

In this situation, when an attacker destroys a node and obtains its master key of the current round, he cannot compromise the identity and authentication messages of previous operations.

For example, if a new node C, wants to join the network, then it will start at a new round. Suppose a network is at the fourth round. Then the whole operation of this phase is as follows:

- Node generates a random number r_i and send a cipher request message to its surrounding CH. This message contains a random number and its identity encrypted by a common master key such as:

$$M_7 = \{r_i, id\}_{k_M}$$

- CH decrypts M_7 , and obtains node identity and a random number.

$$k_{id} = [r_i, id].$$

- Then, encrypts two messages, the first encrypted message contains a round number, number of nodes, a cluster id, and a cluster key which is encrypted by a corresponding key node such as:

$$M_8 = \{R, N, C_{id}, CK^j\}_{k_{id}}$$

- The second encrypted message is a T_{id} . This ticket is encrypted by its current cluster key CK^R and contains nodes identities in its cluster.

$$\{Nodes\ identity\}_{CK^R}$$

- These messages are sent back to the requesting node.
3. When C receives the two messages, it does the following:
- Generates a corresponding key node k'_{id} using the same hash function and checks the validity of its random number.
 - If it is equal, then it proceeds and decrypts the first message and obtains $R, N, C_{id'}$ and CK^R .
 - Now, C hashes the CK, R times such as $CK^R = [CK]^{R-1}$, to synchronize with the current round.
 - It uses CK^R to decrypts the authentication T_{id} and obtains node's identities.

Now, C has node's identities, R, CK^R, N, C_{id} and its k_{id} and can communicate with other nodes in specified cluster.

Node C acts as a requester and CH as an authenticator in above scenario. T_{id} and R parameters are used by CH to authenticate a node. In above case, the authenticator is at fourth round, but C is at the first round. Therefore, C should hash the key $[CK]^{R-1}$ times to synchronize with the current key. Fig. 6. shows the full operation of this phase.

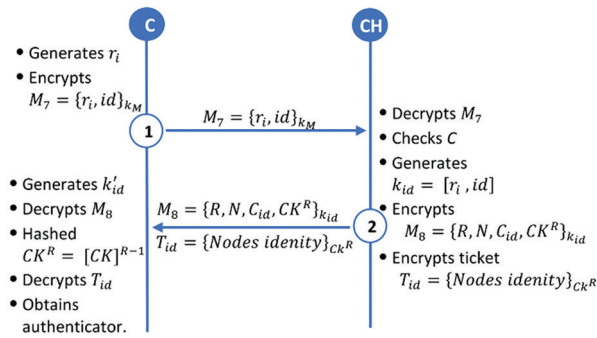


Fig. 6. Authenticate a new node C.

5. RESULTS OF LWAF DEVELOPMENT

The results are illustrated in terms of system simulation. The proposed scheme is based on symmetric cryptography only to overcome the complex computation of public-key cryptography since all nodes are resource constraints. Results are discussed in terms of stated aim and objectives, which encompasses the following:

5.1. DEVELOPING LWAF

Proposed LWAF scans sensors and elects CH s depending on their positions and corresponding battery life. It also creates cluster and scans its nodes and encrypts messages. The secret messages are encrypted by session keys. The session keys are dynamically generated and updated during the communication. This encrypted message contains cluster identity and a number of surrounding nodes. BS receives the encrypted message separately and uses its k_M for decryption,

and creates a cluster key. Each corresponding CH receives an individual encrypt message from BS . Then, it decrypts the incoming message and checks the integrity of its identity and a common master key with a saved key. If it is equal, then the CH starts a deployment process and the first phase is done, otherwise, it cancels.

At the second phase, a node registers itself into the cluster by sending $\{r_i, id\}_{k_M}$. CH obtains node identity and a random number to create a corresponding node key $K_{id} = [r_i, id]$. CH lets a node to know its round, its neighbor nodes, and general cluster information $\{R, N, C_{id}, CK^R\}_{K_{id}}$. The second encrypted message is a ticket T_{id} that contains node's identity $\{node_identity\}_{CK^R}$. A node cannot obtain the ticket unless it is registered in the network. At this stage, each node stores other node's identities, R, CK^R, N, C_{id} and its K_{id} , and can communicate with other nodes in a specified cluster. Then transmits to the next round by hashing CK^R and sets $R=R+1$, such as $CK^{R+1} = [CK^R]$.

The third phase ensures the security of message delivery. If node A wants to send a message to its neighbor B , each node must be updated and be synchronized with the current network round to ensure $CK^R = [CK]^{R-1}$, then, mutual authentication protocol and specific excitation/response processes are performed to generate their common session key $sk_{AB} = [C_{id}, A, B]$ with a specific time $t_{cur} - t_1 \leq \Delta t$.

The fourth phase is enabled when a new node wants to join a network. Ticket authentication and a pre-calculation for excitation/response is done (requester and authenticator) $M_7 = \{r_i, id\}_{k_M}$, $M_8 = \{R, N, C_{id}, CK^R\}_{k_{id}}$ and $T_{id} = \{node_identity\}_{CK^R}$. A new node C , is verified using knowledge of a common master key of previous round $CK^R = [CK]^{R-1}$ and using $k_{id} = [r_i, id]$. Such that, the authentication of a round 2, is constructed using a key derivation of round 1 without storing the previous key.

5.2. USING AUTHENTICATION TICKET

The novelty of this work is by adding an authentication ticket $T_{id} = \{node_identity\}_{CK^R}$. Only registered node has this ticket, this ticket is created by a corresponding CH and sent to the authenticated node to ensure node authentication. It contains all the node identities in its cluster and is used to identify another node. This ticket is encrypted by its cluster key.

5.3. ADOPTING LEACH FRAMEWORK

Since the work is based on LEACH framework, the selection of CH is a major concern to keep a network live and reliable. This scheme emphasizes CH selection by updating the network dynamically. It spreads the CH 's energy selection over multiple nodes, therefore, the CH nodes are not fixed and are self-selected at different time intervals.

Evaluation of this framework is carried out in order to measure the performance of the LWAF scheme, packet delivery rate [28], energy consumption, and access rate in presence of different types of attackers [29].

Simulation of the scheme is performed using MATLAB (R2020a). We considered 500 nodes. 20 runs of the system were carried out for different scenarios. Simulation parameters of the proposed system are shown in Table 2.

Table 2. Simulation Parameters.

Parameters	Values
Area size (m ²)	500 × 500
Wireless bandwidth (Mbps)	2
Simulation duration	(sec) 300
Initial energy (J)	CH = 50, SN = 5
Initial V/BP (J)	CH = 500, SN = 50
Radio range(m)	CH = 150, SN = 50
Number of CHs	6% of nodes

In order to evaluate the proposed work, at first, packet delivery rate (PDR) is simulated based on the mentioned parameters in Table 2, and compared with two existing competing schemes SPINS [19] and LOCK [17], as shown in Fig. 7. Malicious nodes for MNs and CH are eliminated by bidirectional malware detection. LWAF effectively reduces packets errors.

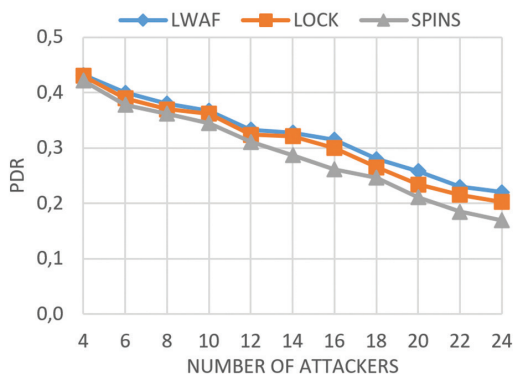


Fig. 7. Packet Delivery Rate.

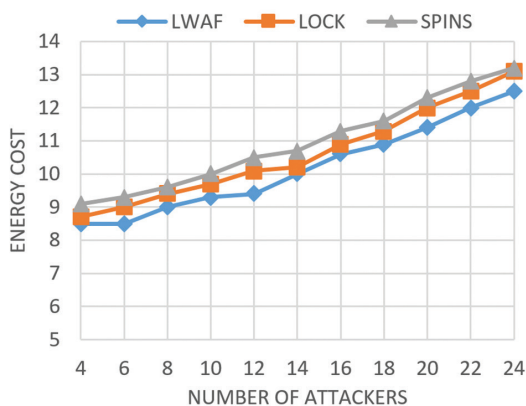


Fig. 8. Average Energy Consumption

As compared with LOCK and SPINS, more packets are sent to a destination sensor.

In Fig. 8 the average energy consumption for all nodes is measured during transmission in terms of sending, receiving and calculation complexity, and compared with LOCK and SPINS.

The average energy consumption increases when the number of attackers will increase and errors increase also, due to increase in error packets.

Fig. 9 shows the evaluation of network resilience ability. Number of nodes being evaluated are 500 and 25 % of them being attackers. The proposed system detects malicious nodes and can exclude them from the network.

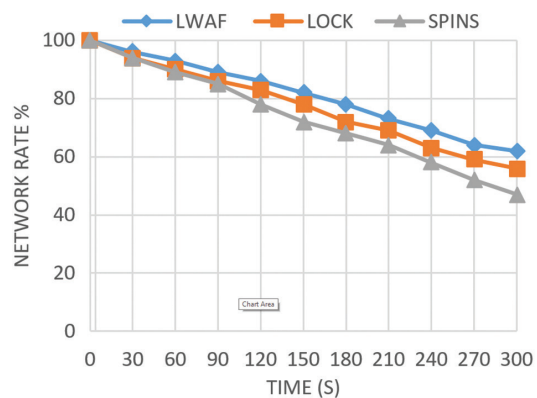


Fig. 9. Access Network Rate.

In addition, session key is dynamically re-generated and distributed to avoid node capturing by malicious nodes. Malicious nodes are unable to compromise other nodes because they don't have the master keys.

6. DISCUSSION OF EXPERIMENTAL RESULTS

Proposed LWAF ensures a CH has all the identities of surrounding nodes and uses a dynamic session key to encrypt each transmitted message. The key is dynamically generated. Therefore, if an attacker tries to compromise the previous key, he cannot either obtain the current session key or cannot synchronize with the current round, this done with the help of a simple calculation timestamp.

In addition, introducing the idea of the ticket increases security level, since it contains all nodes' identities. And hence, a node cannot obtain the ticket unless it is authorized and registered in the network.

Adopting the LEACH framework reduced energy consumption and ensured mobile nodes, therefore, increases system performance.

Practically, the average energy consumption increased when the number of attackers increased on the network, and hence, error packets increased also. A CH in LWAF filters out these errors and avoiding packets spreading to the attackers in the network and hence reduce energy consumption. In contrast with other schemes, they must initiate updating of the keys, which consume more energy.

Through simulation, the performance is better than SPINS and LOCK where it can avoid malicious nodes.

Besides, LWAF adopts multipath propagation routing technology to eliminate the selective forwarding attacks, which makes the PDR even higher.

The limitations of the proposed LWAF are the cryptographic algorithms used in the computation procedures since it is based only on symmetric cryptography. There may be other WSN environments where this framework is not applicable.

The disadvantages of the LWAF scheme includes; the fact that the scheme is affected by the number of nodes. Since the system provides scalability and mobility, increasing sensor nodes is inversely proportional to system performance.

7. CONCLUSION

1. This work emphasizes lightweight cryptographic systems and their important aspects in WSN. We developed LWAF with the intention to provide security primitives in WSN for all phases mentioned above. The system generates fresh random session keys for every authentication between BS, CHs, and MNs to prevent attackers. The simulation showed that; it provides a more efficient security primitive in less power consumption as well as communication complexity overhead as compared with other existing WSN schemes.

2. Generation of ticket is done only by an authorized CH. The novelty of using this ticket is to prevent an attacker from entering into the system. Taking into account, the only authenticated node receives this message through secure mutual excitation/response processes. A node can use this ticket to communicate securely with others in the cluster. Through system simulation, these tickets provide a high level of security.

3. Adopting LEACH framework hierarchy has made the system more reliable for dynamic WSNs and efficient in terms of energy-saving, low complexity overhead and scalability and robustness. The amount of data that must be transmitted to the BS is less compared with others. LWAF focuses on CH selection to distribute energy in an equal manner. Through the study of different WSNs, the selection of CH is a big concern, because a fixed CH drains its battery and hence archive reduction of energy.

Future work in this direction shall focus on applying additional procedures in terms of using asymmetric cryptography and other cryptographic algorithms and focus on the way to resist multiple attacks, robust routing. Besides, the future work shall consider the aspects to reduce the packet transmission time, latency and packet overheads.

8. REFERENCES

- [1] S. G. Fatima, S. K. Fatima, "Home Automation System with WSN and IoT", *International Journal of Advanced Research in Engineering and Technology*, Vol. 10, No. 2, 2019, pp. 78-85.
- [2] M. Peira, J. Fernando, Rocher, Javier, Perra, Lorena, Sendra, Lloret, Jaime, M. Ablanque, P. Vicente, "Autonomous WSN for lawns monitoring in smart cities", *Proceedings of the 14th IEEE/ACS International Conference on Computer Systems and Applications*, 30 October - 3 November 2017, pp. 501-508.
- [3] A. Juels, "RFID security and privacy: A research survey", *IEEE Journal on Selected Areas in Communications*, Vol. 24, No. 2, 2006, pp. 381-394.
- [4] K. Chintalapudi, T. Fu, J. Paek, N. Kothari, S. Rangwala, J. P. Caffrey, R. Govindan, E. Johnson, S. Masri, "Monitoring civil structures with a wireless sensor network", *IEEE Internet Computing*, Vol. 10, No. 2, 2006, pp. 26-34.
- [5] J. Yick, B. Mukherjee, D. Ghosal, "Wireless Sensor Network Survey", *Computer networks*, Vol. 52, No. 12, 2008, pp. 2292-2330.
- [6] W. R. Heinzelman, A. Chandrakasan, H. Balakrishnan, "Energy-efficient Communication Protocol for Wireless Microsensor Networks", *Proceedings of the Hawaii International Conference on System Sciences*, Maui, Hawaii, 4-7 January 2000, Vol. 2, pp. 10.
- [7] M. Elhoseny, A. E. Hassanien, "Secure Data Transmission in WSN: An Overview", *Dynamic Wireless Sensor Networks*, Vol. 165, 2019, pp. 115-143.
- [8] S. E. L. Khediri, N. Nasri, A. Wei, A. Kachouri, "A new Approach for Clustering in Wireless Sensors Networks Based on LEACH", *Procedia Computer Science*, Vol. 32, 2014, pp. 1180-1185.
- [9] J. Sen, "A Survey on Wireless Sensor Network Security", *International Journal of Communication Networks and Information Security*, Vol. 1, No. 2, 2009, pp. 55-78.
- [10] A. Ghosal, S. D. Bit, "A Jamming-Attack-Defending Data Forwarding Scheme Based on Channel Surfing in Wireless Sensor Networks", *Security and Communication Networks*, Vol. 6, No. 11, 2013, pp. 1367-1388.
- [11] K. Haseeb, I. U. Din, A. Almogren, N. Islam, "An Energy Efficient and Secure IoT-Based WSN Framework: An Application to Smart Agriculture", *Sensors*, Vol. 20, No. 7, 2020, pp. 2081.

- [12] A. Ghosal, S. Das, "A Lightweight Security Scheme for Query Processing in Clustered Wireless Sensor Networks" *Computers & Electrical Engineering*, Vol. 41, 2015, pp. 240-255.
- [13] R. R. K. Chaudhary, K. Chatterjee, "An Efficient Lightweight Cryptographic Technique for IoT based E-healthcare System", *Proceedings of the 7th International Conference on Signal Processing and Integrated Networks*, Noida, India, 27-28 February 2020, pp. 991-995.
- [14] C. Buratti, A. Conti, D. Dadari, R. Vedone, "An Overview on Wireless Sensor Networks Technology and Evolution", *Sensors*, Vol. 9, No. 9, 2009, pp. 6869-96.
- [15] N. G. Palan, B. V. Barbadekar, S. Patil, "Low Energy Adaptive Clustering Hierarchy (LEACH) Protocol: A Retrospective Analysis", *Proceedings of the International Conference on Inventive Systems and Control*, Coimbatore, India, 19-20 January 2017, pp 1-12.
- [16] S. Chandra, S. Bhattacharyya, S. Paira, S. K. Alam, "A Study and Analysis on Symmetric Cryptography", *Proceedings of the International Conference on Science Engineering and Management Research*, Chennai, India, 27-29 November 2014, pp 1-8.
- [17] M. Eltoweissy, M. Moharrum, R. Mukkamala, "Dynamic key management in sensor networks", *IEEE Communications Magazine*, Vol. 44, No. 4, 2006, pp. 122-130.
- [18] D. Liu, P. Ning, "Efficient Distribution of Key Chain Commitments for Broadcast Authentication in Distributed Sensor Networks", *North Carolina State University, Department of Computer Science*, 2002.
- [19] A. Perrig, R. Szewczyk, J. D. Tygar, V. Wen, D. E. Culler, "SPINS: Security Protocols for Sensor Networks", *Wireless Networks*, Vol. 8, No. 5, 2002, pp. 521-534.
- [20] J. Deng, R. Han, S. Mishra, "Limiting DoS Attacks During Multihop Data Delivery in Wireless Sensor Networks", *International Journal of Security and Networks*, Vol. 1, No. 3, 2006, pp. 167-178.
- [21] B.-C. C. Lai, D. D. Hwang, S. P. Kim, I. Verbauwhede, "Reducing Radio Energy Consumption of Key Management Protocols for Wireless Sensor Networks", *Proceedings of the International Symposium on Low Power Electronics and Design*, Newport Beach, CA, USA, 11-11 August 2004, pp. 351-356.
- [22] H. Soroush, M. Salajegheh, T. Dimitriou, "Providing Transparent Security Services to Sensor Networks", *Proceedings of the International Conference on Communications*, Glasgow, UK, 24-28 June 2007, pp. 3431-3436.
- [23] D. Qin, S. Jia, S. Yang, E. Wang, Q. Ding, "A Lightweight Authentication and Key Management Scheme for Wireless Sensor Networks", *Journal of Sensors*, Vol. 2016, 2016, pp. 1-9.
- [24] R. Nanda, P. V. Krishna, "Mitigating Denial of Service Attacks in Hierarchical Wireless Sensor Networks", *Network Security*, Vol. 2011, No. 10, 2011, pp. 14-18.
- [25] J. Sen, "A Survey on Wireless Sensor Network Security", *International Journal of Vommunication Networks and Information Security*, Vol. 1, No. 2, 2009, pp. 55-78.
- [26] J. Daemen, S. Hoffert, M. Peeters, G. V. Assche, R. V. Keer, "Xoodyak, a Lightweight Cryptographic Scheme", *IACR Transactions on Symmetric Cryptology*, Vol. 2020, No. S1, 2020, pp. 60-87.
- [27] M. Kocakulak, I. Butun, "An Overview of Wireless Sensor Networks Towards Internet of Things", *Proceedings of the 7th Annual Computing and Communication Workshop and Conference*, Las Vegas, NV, USA, 9-11 January 2017, pp. 1-6.
- [28] J. Dong, K. E. Ackermann, B. Bavar, C. N. Rotaru, "Mitigating Attacks Against Virtual Coordinate-Based Routing in Wireless Sensor Networks", *Proceedings of the 1st ACM Conference on Wireless Network Security*, 31 March 2008, pp. 89-99.
- [29] A. Mitra, A. Banerjee, W. Najjar, D. Zeinalipour-Yazti, V. Kalogeraki, D. Gunopulos, "High Performance, Low Power Sensor Platforms Featuring Gigabyte Scale Storage", *Proceedings of the 3rd International Workshop on Measurement, Modeling, and Performance Analysis of Wireless Sensor Networks*, San Diego, CA, USA, 21 July 2005, pp. 148-157.

Environmental impact estimation of ceramic tile industry using modeling with neural networks

Original Scientific Papers

Verica Hocenski

Keramika Modus d.o.o.
Vladimira Nazora 67, Orahovica, Croatia
verica.hocenski@gmail.com

Ana Lončarić Božić

University of Zagreb
Faculty of Chemical Engineering and Technology
Marulićev trg 19, Zagreb, Croatia
abozic@fkit.hr

Nedjeljko Perić

University of Zagreb
Faculty of Electrical Engineering and Computing
Unska 3, Zagreb, Croatia
nedjeljko.peric@fer.hr

Denis Klapan

J. J. Strossmayer University of Osijek,
Faculty of Dental Medicine and Health
Crkvena 21, Osijek, Croatia
klapandenis@gmail.com

Željko Hocenski

J. J. Strossmayer University of Osijek,
Faculty of Electrical Engineering, Computer Science
and Information Technology Osijek
Cara Hadrijana 10, Osijek, Croatia
zeljko.hocenski@ferit.hr

Abstract – *The ceramic tiles industry has a significant environmental impact due to consumption of raw materials, energy and environmental emissions. There are numerous activities on global level in accordance to the principles of sustainable development. This paper presents the development and application of mathematical models of manufacturing processes based on static neural networks for prediction and control of environmental impact of ceramic tiles production process. The neural network learning is made based on known input and output values from the production process. The control of the environmental impact is made on the basis of the output values from the process amounts of correct and faulty ceramic tiles. The model for prediction of correct amount of tiles and percentage of waste with an average error of 1.7% is presented in this paper. It could be successfully used to estimate and control the environmental influence. A simple model of production process has been applied in the manufacturing process of ceramic tile factory KIO Keramika d.o.o. Orahovica. It produced ceramic tiles using monofiring process according to EN 14 411 B III group Part L. The company has introduced and certified management systems according to ISO-9001. and ISO 14001.*

Keywords: *ceramic tiles, estimation, environmental impact, neural networks*

1. INTRODUCTION

The application of artificial neural networks is based on knowledge of the structure and functioning of the human brain and its great capabilities to solve the complex problems. A great number of neural networks of different structure is used that can basically be divided into static and dynamic [1]. This paper describes the application of static neural network to produce a mathematical model of the production process. This paper uses two-layer neural network shown in Fig.1.

The neural networks have a large application area. They are used to solve problems in various fields of science, technology, medicine, meteorology, economics, sociology, biology, ecology, etc. The paper [2] describes

the results of the evaluation of nonlinear systems by neural networks and comparison of two techniques to select the optimal number of model parameters. Paper [3] presents the study of the structure and role of the learning algorithm in real time applications of neural networks is presented. Another paper published later [4] describes the successful application of neural networks to control the gas of the vehicle. In reference [5] the authors propose a new type of neural network to evaluate the robustness of tires with road friction. The application of neural networks for wind gusts is described paper [6] for predicting the spatial distribution of the wind. The paper published in 2010 describes a successful application of neural networks for automatic sorting of ceramic tiles [7].

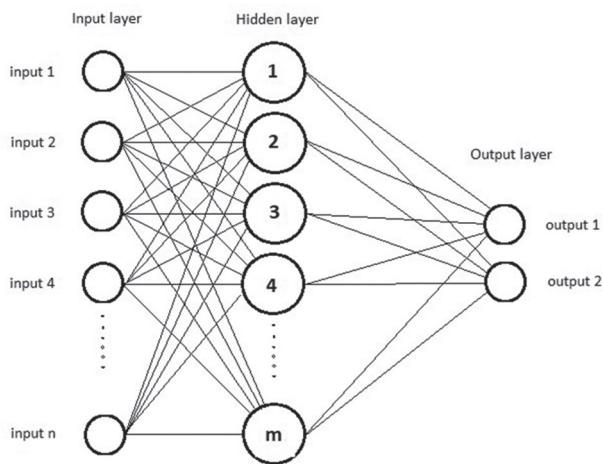


Fig. 1. Schematic view of two-layered neural network

Neural networks in meteorology has been presented in the 2009 for predicting wind flow [8]. The paper published in 2010 describes the application of neural networks to overlook flood [9]. The neural networks could be used to recognize faces and identify persons. The modelling of influence of waste rubber by neural networks is described in 2019 [10]. Another flood-routing modelling with neural networks is described in [11] and electricity consumption forecasting by neural networks is described in 2019 [12].

A simple model of the production process has been applied to the manufacturing process of ceramic tiles factory KIO Keramika d.o.o. in Orahovica that produces ceramic tiles using mono-firing technology according to EN 14 411 Group B III Part L [13]. The company had been certified for management systems according to ISO-9001 [14]. and ISO 14001 [15]. The factory produces ceramic tiles for wall and floor interior lining of various sizes and design by declared norm EN - 14 411 [13]. The diagram of the production process is shown in Fig. 2 [16].

The tiles are manufactured by mono-firing technology for wall and floor tiles. The production process consists of a series of sub-processes: the preparation of raw materials, the preparation of granules for pressing, shaping, drying of raw tiles, glazing, firing, sorting and packaging [17].

Preparation of raw materials. The mixture of raw materials for ceramic tiles production are made from several components: clay, granite and dolomite. The clay is exploited from the mine in factory area. The clay is excavated and arranged in lots. After aging the clay is taken to a warehouse. The materials (frit and pigments for glaze) are delivered by trucks from suppliers mostly from Italy, Spain and other countries.

Preparation of granules for pressing. The mixture of components is grinded by wet process (along with water and electrolyte) with the addition of ceramic wastes in a ball mill. After milling the material is atomized into granules and kept in silos from which it is fed to the press.

The shaping of tiles is made by dry pressing. The hydraulic presses of high power and productivity are used. The granulate needs to be pressed under specific pressure. The tools enable pressing of several plates simultaneously.

Drying of raw tiles. The pressed tiles are introduced into the dryer. The tiles are dried gradually by warming. The drying time depends on the type of tiles (for wall or floor covering), and the necessary moisture content of raw tiles.

Glazing process. After drying tiles come to glazing. A layer of glaze is applied to the tiles and decorating is done. The tiles are stacked in wagons and taken to the oven for firing or baking.

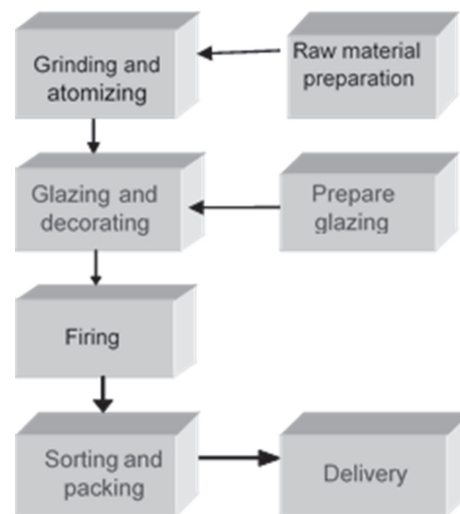


Fig. 2. Schematic view of production process

Firing or baking of tiles takes place in an oven by a mono-firing process at a temperature between 1050 and 1200 °C. After cooling, the tiles are taken for sorting.

Sorting and packing. After baking, the tiles are inspected for surface defects. According to the results of the inspection, they are classified into classes and the waste is separated according to the EN-14411 standard, packed in cardboard boxes and placed on pallets.

2. MODEL OF PRODUCTION PROCESS

The static neural network is a development environment for making mathematical model of the production process that includes a software package with MATLAB tools for neural networks (nntool and nftool) suitable for studies of the structure of neural network and evaluating the results. It is applied the two-layer feedforward (feed-forward) network with sigmoid activation function in the hidden layer and linear activation function in the output layer. Learning was performed by Levenberg-Marquardt algorithm with a retroactive effect. The mathematical model of the production process by static neural network is used to simulate the manufacturing process. The evaluation of the actual results is obtained by measurements [16] [18].

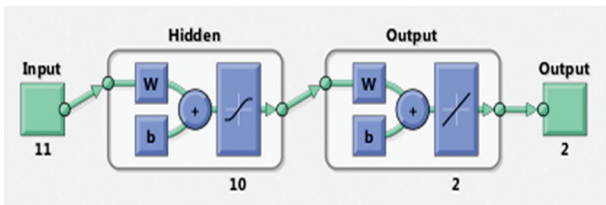


Fig. 3. Simple neural network model with 11 inputs and 2 outputs, which has 10 neurons in the hidden layer and 2 neurons in the output layer.

Research of best neural network structure is a learning process in which the network changes its parameters and coefficients trying to achieve desired target output values based on the known inputs, selected input data sets and the corresponding set of known output data. The input data are obtained by analyzing the mono-firing production process technology in the preliminary assessment phase.

Table 1. Inputs and outputs of process model

A simple model		
Inputs	Process phase	Outputs
clay dolomite electrolyte water gas atomizer	preparation of slip and granules	
gas dryer	pressing tiles and drying	- correct tiles - waste tiles
frit engobe pigment other materials	glazing and decoration	
gas firing	firing	

The inputs are monthly consumption of raw materials used in the preparation of materials, such as clay, dolomite, electrolyte, water, gas in atomizer, gas for drying raw tiles and burning, raw material for the glazing of frit, pigments and other raw materials. A simple model is made according to a set of 11 input variables on the consumption of raw materials and manufacturing process in the year 1998. Two output values were chosen: the correct amount of tiles that meet the requirements of the technical standard EN 14 411: 2004 [13] and the percentage of waste tiles, that are not usable for the primary purpose, because they are not in compliance with the requirements of technical standards [14]. The values of input and output are presented by a simple process stages in Table 1.

3. LEARNING A SIMPLE PRODUCTION MODEL

The learning process of simple model neural network was performed with 10, 15 and 20 neurons in the hidden layer. The evaluation of properties of the obtained neural network structure was completed using the mean squared error (MSE) and regression analysis. Only some of the results of learning network with 20 neurons in the hidden layer are shown in Table 2. The table shows the order of training (Tr), the mean error MSE, regression R, performance P, gradient Gr, Mu (parameter μ) and the number of iterations Ni of that training. The lowest MSE gives the best performance P. The regression shows how close are the model output and target value.

Table 2. Results of learning of network with 20 neurons in hidden layer

Tr	Learning results					
	MSE	R	P	Gr	Mu	Ni
1.	3,293e ⁻³	0,941	1,9e ⁻¹⁴	9,24e ⁻⁸	1,0e ⁻⁷	4
2.	5,257e ⁻³	0,919	1,4e ⁻¹⁹	1,5e ⁻¹⁰	1,0e ⁻⁷	4
3.	2,385e ⁻¹³	0,999	2,3e ⁻¹³	5,5e ⁻⁷	1,0e ⁻⁶	3
4.	1,839e ⁻⁵	0,997	3,9e ⁻¹⁸	1,1e ⁻⁹	1,0e ⁻⁷	4
5.	1,108e ⁻²	0,889	4,0e ⁻¹³	7,2e ⁻⁷	1,0e ⁻⁷	4
6.	3,055e ⁻⁴	0,996	4,3e ⁻¹⁴	5,8e ⁻⁸	1,0e ⁻⁶	3
7.	6,009e ⁻³	0,909	2,5e ⁻¹¹	2,4e ⁻⁶	1,0e ⁻⁶	3
8.	8,325e ⁻³	0,914	3,8e ⁻¹³	6,9e ⁻⁷	1,0e ⁻⁷	4
9.	1,243e ⁻¹⁹	1,000	1,2e ⁻¹⁹	1,9e ⁻¹⁰	1,0e ⁻⁷	4
10.	8,168e ⁻⁴	0,981	1,3e ⁻¹²	8,3e ⁻⁷	1,0e ⁻⁶	3
11.	1,687e ⁻⁶	0,999	8,3e ⁻¹²	2,4e ⁻⁶	1,0e ⁻⁶	3
12.	1,708e ⁻¹⁷	0,999	1,7e ⁻¹⁷	3,8e ⁻⁹	1,0e ⁻⁷	4
13.	5,155e ⁻³	0,935	4,1e ⁻¹⁶	5,9e ⁻⁹	1,0e ⁻⁷	4
15.	6,029e ⁻¹¹	0,999	6,0e ⁻¹¹	6,4e ⁻⁶	1,0e ⁻⁶	3

The network with 20 neurons in the hidden layer and the smallest difference between the real output values and desired target was selected for model verification of the production process. The values for the selected network used for further testing are shown in Table 3.

Table 3. The ninth best resulting learning network with 20 neurons in hidden layer.

Tr	Learning results					
	MSE	R	P	Gr	Mu	Ni
9.	1,243e-19	1,000	1,2e-19	1,9e-10	1,0e-7	4

The results of ninth learning network with 20 neurons in the hidden layer are presented in the following pictures. The ninth learning network has the best result as the MSE and performance are the lowest and regression is one from all training networks. The output from views that have been obtained for the selected network to test the model are presented in pictures below. Fig. 4 shows a histogram of error as the difference between target and output.

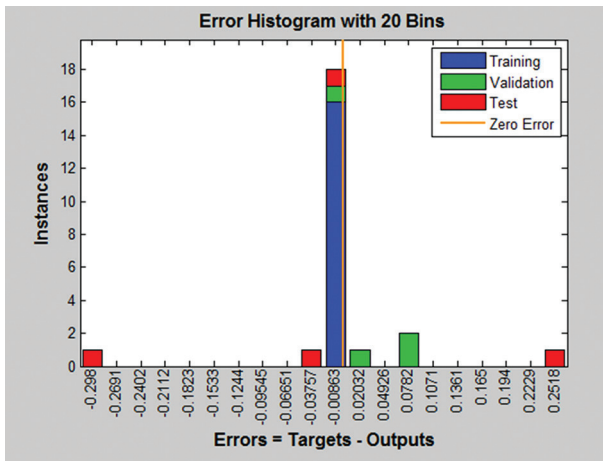


Fig. 4. Histogram and progress of ninth learning with 20 neurons in the hidden layer.

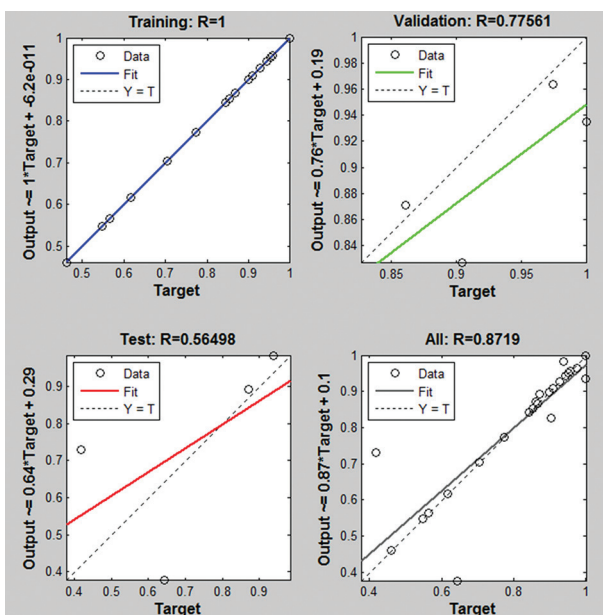


Fig. 5. Regression and progress of ninth learning with 20 neurons in the hidden layer.

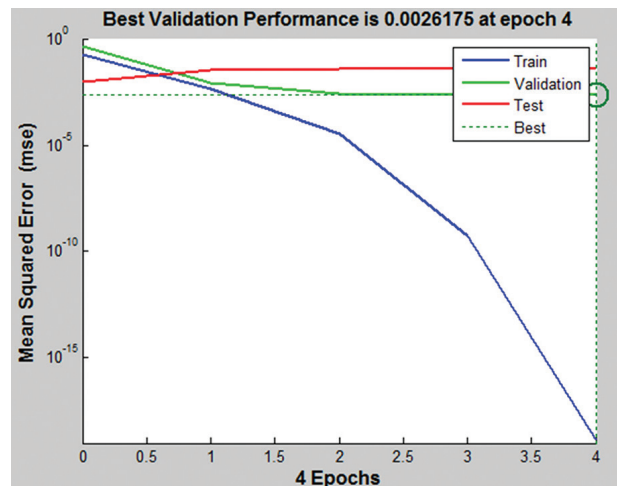


Fig. 6. MSE diagram of ninth learning with 20 neurons in the hidden layer.

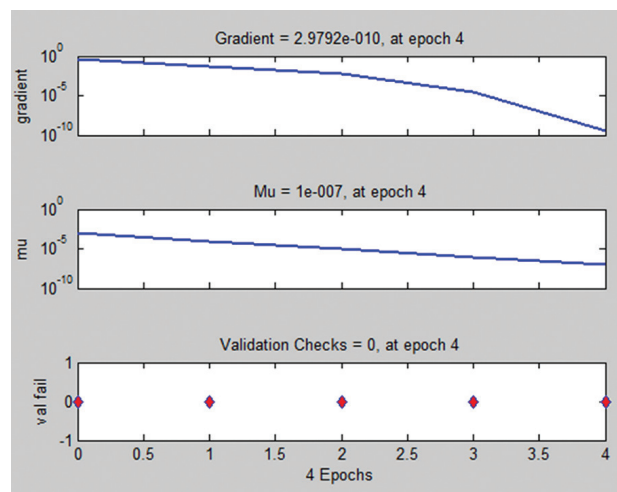


Fig. 7. Gradient diagrams, Mu (parameter μ) and validation of ninth learning with 20 neurons in the hidden layer.

Due to the high MSE of results modeling is continued on network structure and parameters obtained by ninth learning with 20 neurons in the hidden layer.

The Fig. 5 to Fig. 7 are presenting the results of modeling tool and they are used for comparison between trainings to enable the choice of the best network. The number of epochs or iterations depends on getting the best result in some training as presented in Table 2.

4. RESULTS OF SIMPLE MODEL

The network with parameters shown in Table 3 obtained by ninth learning with 20 neurons in the hidden layer was selected to test the models of the production process. The application of a simple model to the data by months of production of ceramic tiles is used for years 1999, 2000, 2001, 2002, 2003, and 2004, 2005 and 2006. The obtained results are for correct amount of tiles and waste tile amount for each year. The model error was calculated by comparing the actual values of output variables obtained by measuring.

4.1. MODEL RESULTS FOR CORRECT TILES

Fig. 8 shows the results of total annual quantity of produced correct tiles and the total quantity the correct tiles in m² per year obtained by model using the neural network from ninth learning with 20 neurons in the hidden layer. A comparison between the values of the production process for the correct amount tiles for the observed period of 1999 - 2006 year and the values obtained by the model and the model error was calculated for each year. Fig. 9 shows the annual output error for the correct tiles compared with the average error that is around 6.5 %.

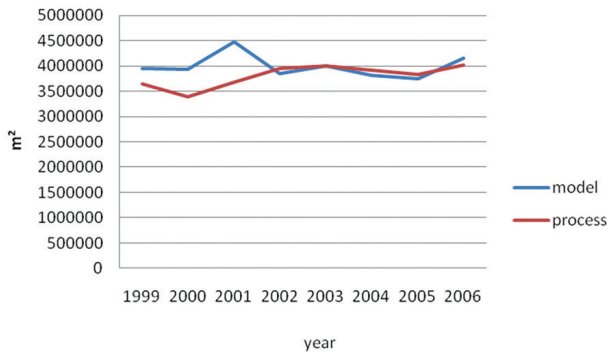


Fig. 8. Comparative review of output from the process and the amount obtained by model and by year.

From Fig. 9 it can be seen that after year 2002 model error decreases and is on average 4.8%

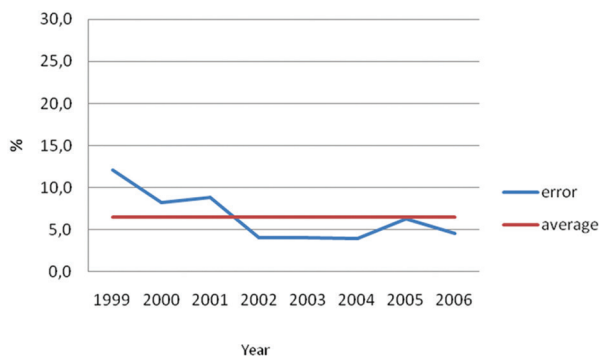


Fig. 9. Model error for the correct amount tiles per year and the average error.

The deviation of the results obtained by the model and real production within one year by month was analyzed. Fig. 10 shows the output of the correct tiles per month in 2006 for quantity and value of the correct tiles obtained using a simple model with a neural network for ninth learning with 20 neurons in the hidden layer.

The Fig. 10 shows the largest variations are observed in January and December 2006.

The largest deviations are in winter months of December and January. Fig. 11 shows the model error percentages for the correct amount of tiles in months of year.

From Fig. 12 it can be seen that the model error is the largest in the winter months and especially at the beginning and end of the year. The average model error for December and January between 1999 and 2006 is around 13.1%. That is twice as much as the average error (6.5%) in the observed period. The larger model error in December and January can be explained by the fact that due to the holidays there are fewer working days in December. The first week of January is the overhaul of equipment, and production stops. It is caused by the lower production in the winter months and the problems of delivery of natural gas. Because of the low temperatures, gas consumption is higher, so it was a big turn off consumers.

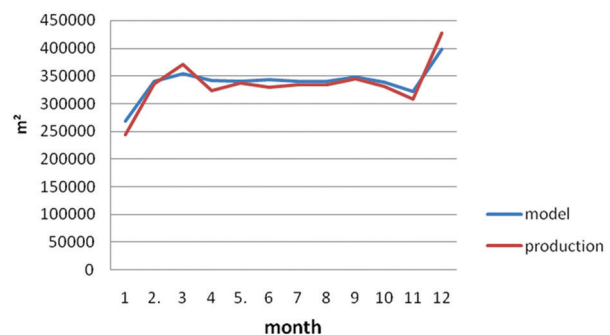


Fig. 10. Amount of the correct tiles and tiles obtained by a simple model of neural network in m² in year 2006 the by month.

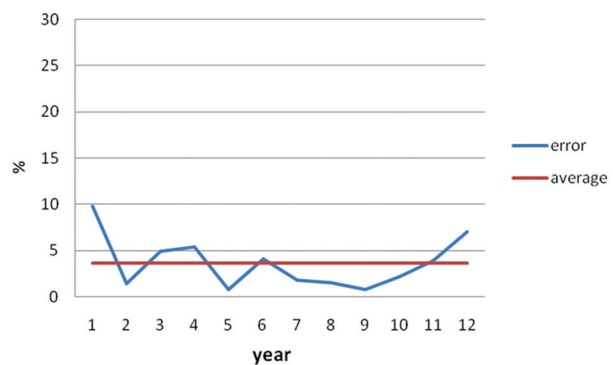


Fig. 11. Model error for the correct amount tiles per months of 2006.

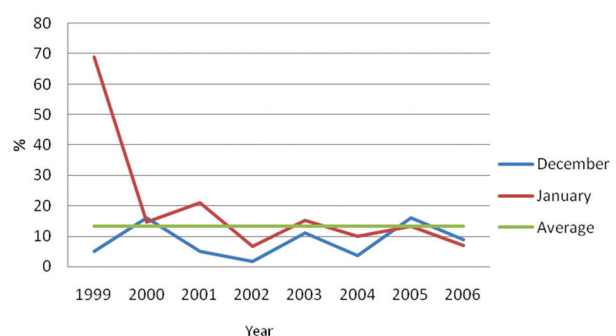


Fig. 12. Model error (%) of the correct amount of tiles in December and January for several years.

4.2. MODEL RESULTS FOR WASTE TILES

The results obtained by model are compared with the values of the production process for the percentage of waste tiles. The results obtained by a simple model based on neural network with 20 neurons in the hidden layer for 11 input variables and the known output values are calculated for waste tiles in 1999, 2000, 2001, 2002, 2003, 2004, 2005 and 2006. The percentage of waste tiles derived from the neural network and the percentage of waste tiles in real production in the period from 1999-2006 are shown in Fig. 13.

The absolute model error of waste tiles was calculated. The percentage of model results in relation to the percentage of produced waste tiles is obtained as the difference of these values. The average model error for the amount of waste tiles in period 1999-2006 of the simple model based on neural network is shown in Fig. 14.

The model error varies by month. The smallest model error was obtained in 1999 when it was 0.1% but in 2005 was around to 4.13%.

If the movement of the percentage of waste tiles generated from the process and percentage of waste tiles from the model is observed from 1999 until 2002, the model gives lower values than those from the process. During the period since 2002 to 2006 the model provides a higher percentage of waste tiles than from production. The average absolute model error of waste tiles per year is around 1.7%.

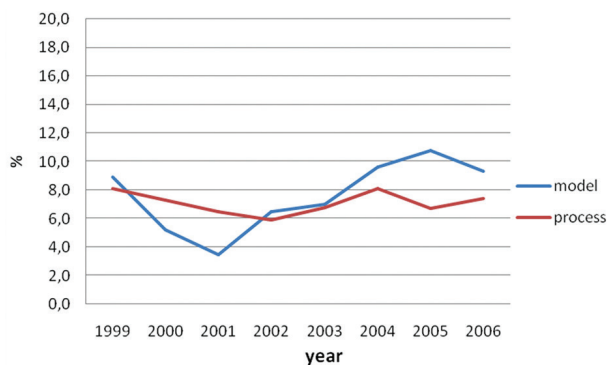


Fig. 13. Percentages of waste tiles obtained by model compared to real values per year.

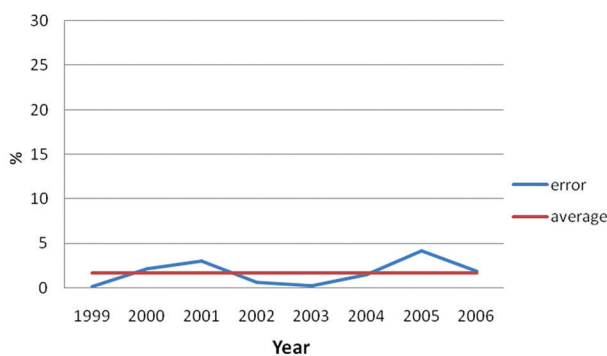


Fig. 14. Model error of waste tiles in period 1999 - 2006.

5. CONCLUSION

This paper presents a simple mathematical model of the production process based on static neural networks in ceramic tiles industry. The research of the best neural network structure is done by learning process or trainings with known standardized inputs and outputs by changing the network parameters to get the best results. The best simple model is obtained by ninth learning with 20 neurons in the hidden layer for neural network with 11 inputs and 2 outputs. The model is applied and calculated for the eight years of production. The resulting model error for the correct tiles is in average around 6.4 % and 1.7 % for waste tiles. The monitoring period from 1999 until 2006 is limited and could not be continued to next years as the real data after are not more available because the factory changed the owner and now does not produces.

The simple model can be used to predict the environmental impact of production on the amount and percentage of correct and waste tiles. The application of this new approach can produce better control effect of ceramic industry to the environment.

The simple model using static neural network enables the prediction of environmental impact of the production process of ceramic tiles. The developed simple model could be used in simulation of the influence of input variables: clay, dolomite mud, electrolytes, water, gas used in atomizer, gas for drying tiles, frit, engobe, pigments, gas for firing and other raw materials on two output variables. It is possible to test the influence of reduction in some of the inputs to percentage and the amount of the correct and waste tiles.

The quantity of correct tiles depends on used technology and equipment. The presented model can predict the quantities of produced correct and waste tiles using new equipment or new technologies. The presented model could be used to similar production processes for prediction and improving management.

6. REFERENCES

- [1] R. Rojas, "Neural Networks: A Systematic Introduction", Springer-Verlang Berlin, 1996.
- [2] I. Petrović, M. Baotić, N. Perić, "Regularization and validation of neural network models of nonlinear systems", *Elektrotechnik und Informationstechnik*, Vol. 117, No. 1, 2000, pp. 24-31.
- [3] M. Baotić, I. Petrović, N. Perić, "Convex Optimization in Training of CMAC Neural Networks", *Automatika*, Vol. 42, No. 3-4, 2001, pp. 151-157.
- [4] M. Barić, I. Petrović, N. Perić, "Neural network based sliding mode control of electronic throttle", *Proceedings of the IFAC Symposium on Advances*

- in Automotive Control, Salerno, Italy, 19-23 April 2004, pp. 176-182.
- [5] J. Matuško, I. Petrović, N. Perić, "Neural network based tire/road friction force estimation", Engineering Applications of Artificial Intelligence, Vol. 21, No. 3, 2008, pp. 442-456.
- [6] V. Spudić, M. Marić, N. Perić, "Neural networks based prediction of wind gusts", Proceeding of the European Wind Energy Conference EWEC, Marseille, France, 16-19 March 2009, pp. 2-9.
- [7] T. Keser, Ž. Hocenski, V. Hocenski, "Intelligent Machine Vision System for Automated Quality Control in Ceramic Tiles Industry", Strojarstvo, Vol. 51, No. 5, 2010, pp. 101-110.
- [8] A. Elshafie, O. Karim, M. R. Taha, "Non-Linear Prediction Model for Scour and Air Entrainment Based Static Neural Network Approach", European Journal of Scientific Research, Vol. 27, No. 3, 2009, pp. 400-416.
- [9] R. P. Deshmukh, A. A. Ghatot, "Short Term Flood Forecasting Using RBF Static Neural Network Modeling a Comparative Study", International Journal of Computer Science and Information Security, Vol. 8, No. 6, 2010, pp. 93-98.
- [10] M. Hadzima-Nyarko, E. K. Nyarko, N. Ademović, I. Miličević, T. Kalman Šipoš, "Modelling the Influence of Waste Rubber on Compressive Strength of Concrete by Artificial Neural Networks", Materials, Vol. 12, No. 4, 2019, pp. 1-18.
- [11] M. Nikoo, F. Ramezani, M. Hadzima - Nyarko, E. K. Nyarko, "Flood-routing modeling with neural network optimized by social-based algorithm", Natural hazards, Vol. 82, No.1, 2016, pp. 1-24.
- [12] I. Barić, R. Grbić, E. K. Nyarko, "Short-Term Forecasting of Electricity Consumption Using Artificial Neural Networks - an Overview", Proceedings of the 42nd International Convention on Information and Communication Technology, Electronics and Microelectronics, Opatija, Croatia, 20-24 May 2019, pp. 1076-1081.
- [13] "HRN EN 14 411: 2004 Keramičke pločice-Definicije, razradba, značajke i označavanje" (EN 14 411:2006, Second edition, December 2008)
- [14] "HRN ISO 9001: Sustavi upravljanja kvalitetom-Zahtjevi" (ISO 9001: 2008; EN ISO 9001: 2008), Fifth Edition, April 2009.
- [15] "HRN EN ISO 14001: Sustavi upravljanja okolišom-Zahtjevi sa uputama za primjenu" (ISO 14001: 2004, EN ISO 14001:2004), Third Edition, April 2009.
- [16] V. Hocenski, "Novi pristup smanjenju utjecaja keramičke industrije na okoliš temeljen na neuronskim mrežama", University of Zagreb, Faculty of chemical engineering and technology, Zagreb, Croatia, PhD Thesis, 2012. (In Croatian)
- [17] "Reference Document on Best Available Techniques in the Ceramic manufacturing industry, EU Commission", August 2007, https://eippcb.jrc.ec.europa.eu/sites/default/files/2019-11/cer_bref_0807.pdf (accessed: 2020)
- [18] V. Hocenski, Ž. Hocenski, S. Vasilić, "Application of Results of Ceramic Tiles Life Cycle Assessment due to Energy Savings and Environment Protection", Proceedings of the IEEE International Conference on Industrial Technology, Mumbai, India, 15-17 December 2006, pp. 2972-2977

The impact of collarette region-based convolutional neural network for iris recognition

Original Scientific Papers

Souheila Tounsi

Higher School of Industrial Technologies (ESTI),
LERICA Laboratory, Badji Mokhtar-Annaba University, Annaba, Algeria
Annaba city, P.O Box 218 23000, Annaba, Algeria.
tounsi@esti-annaba. dz

Karima Boukari

Badji-Mokhtar University,
Faculty of Technology, Department of electronics,
LERICA Laboratory, Badji Mokhtar-Annaba University, Annaba, Algeria
Annaba University, P.O. Box 12, 23000 Annaba, Algeria
boukkarima@yahoo. Fr

Abdourazek Souahi

Badji-Mokhtar University,
Faculty of Sciences, Department of mathematics,
Laboratory of advanced materials, Badji Mokhtar-Annaba University,
Annaba, Algeria
Annaba University, P.O. Box 12, 23000 Annaba, Algeria
arsouahi@yahoo.fr

Abstract – Iris recognition is a biometric technique that reliably and quickly recognizes a person by their iris based on unique biological characteristics. Iris has an exceptional structure and it provides very rich feature spaces as freckles, stripes, coronas, zigzag collarette area, etc. It has many features where its growing interest in biometric recognition lies. This paper proposes an improved iris recognition method for person identification based on Convolutional Neural Networks (CNN) with an improved recognition rate based on a contribution on zigzag collarette area - the area surrounding the pupil - recognition. Our work is in the field of biometrics especially iris recognition; the iris recognition rate using the full circle of the zigzag collarette was compared with the detection rate using the lower semicircle of the zigzag collarette. The classification of the collarette is based on the Alex-Net model to learn this feature, the use of the couple (collarette/CNN) allows for noiseless and more targeted characterization and also an automatic extraction of the lower semicircle of the collarette region, finally, the SVM training model is used for classification using grayscale eye image data taken from (CASIA-iris-V4) database. The experimental results show that our contribution proves to be the best accurate, because the CNN can effectively extract the image features with higher classification accuracy and because our new method, which uses the lower semicircle of the collarette region, achieved the highest recognition accuracy compared with the old methods that use the full circle of collarette region.

Keywords: Iris Recognition, Collarette zigzag, CNN, CASIA-Iris-Lamp V4, biometric, SVM.

1. INTRODUCTION

Making an application more secure and less accessible to unwanted people requires discerning one person from another. There are several ways to identify a person and biometrics is one of the most secure alternatives so far.

An iris is a spherical membrane of the eye, among the sclera and pupil. It starts to shape throughout the embryo phase, completing its formation at about eight

months of age. The originality of the iris lies in the richness of texture details resulting from the radial furrows, crypts, filaments, flecks, pigment frills, stripes, arching ligaments, and collarette. This richness makes the human iris one of the most reliable biometric characteristics [1]. The area of the iris is composed of two regions, the outer ciliary zone, and the central pupillary zone. The area between these two regions is the collarette. The collarette contains sufficient discriminating characteristics. It is less affected by pupil dilation and is

generally unaffected by eyelashes and eyelids [2]. Fig. 1 shows a human iris.

This paper proposes an improved iris recognition method for person identification based on CNN and zigzag collarette. The iris detection rate using the full circle of the collarette region was compared with the lower semicircle of the collarette area. Our approach of using the latter one is evaluated on images from the CASIA-Iris-Lamp V4 database. This version 4 of the CASIA database has been applied for the first time to test the effect of the zigzag collarette region using convolution networks (CNNs) as feature extractors.

The rest of this paper is as follows: Section 2 gives a short review of past works that used iris recognition and collarette area, Section 3 explains our proposed approach including experimental results and analysis and Section 4 provides the conclusion of our work.

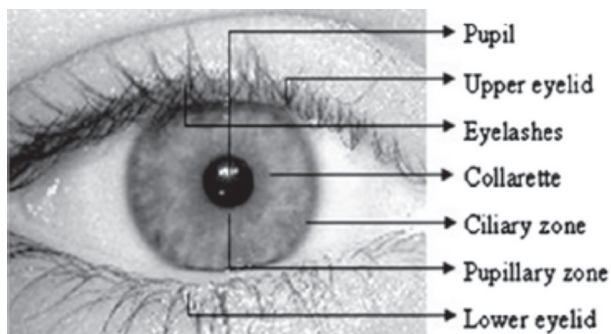


Fig. 1. Human eye

2. RELATED WORK

In recent years, the field of biometric identification has undergone remarkable development. Because of its high reliability and its importance in many fields.

- In the papers [3], the author proposes a high-level security algorithm for the encryption of iris images by combining the permutation method, the QR code, and the chaotic system.
- In the papers [4] an algorithm is proposed to detect a type of intraocular cancer called Uveal Melanoma (UM), the proposed method uses iris segmentation algorithms and proposes a new algorithm for the detection of UM using fuzzy logic and artificial neural networks.
- Iris recognition is used in [5] in combination with fingerprints and palmpoints for multimodal biometric verification at the final decision stage. In [6], the authors segmented the iris as follows: the detection of eye regions was done via an unsupervised neural network, the eye contour was determined using the canny filter, and the pupil and iris using the Hough.
- In [7], the authors used a graphical user interface for the segmentation of the iris image; this interface uses active contours for non-cooperative

biometric recognition to localize the iris structure.

- A new proposal for detecting eyelashes and eyelids with the least noise is discussed in [8], this proposal reduces the detection time of eyelashes and eyelids in the iris image using the Hough transform.
- In [9], the authors presented a new scheme for cancelable iris recognition system based on comb filtering, the author used in his system a coarse to fine the iris localization, then feature extraction using Gabor filtering.
- In the paper [10], the proposed idea adopts the first two phases of Daugman's approach, localization, and standardization. After the normalization stage, the system uses the Base64 coder to convert the normalized image of the iris, into plain text, then extract the language-independent features of the resulting text without modifying its statistical properties, which leads to a numerical model, the resulting model will be later classified using machine learning algorithms such as Random Forest.
- In paper [11], the authors used the circular Hough transform for segmentation to find the region of interest (ROI) of images of the eye, after that Daugman's Rubber sheet model is used for normalization. Then, for feature extraction, the GLCM technique is used. Finally, Discriminant analysis is applied for the classification of the images.
- In [12], the authors proposed a new method of classification and feature extraction based on the hybrid classifier MLPNN-ICA and grey level difference and the hybrid classifier MLPNN-ICA.
- In [13], the authors designed an iris recognition system consisting of segmentation where the author implemented the Canny edge detection algorithm for edge detection, rubber sheet model for normalization, Gabor filter for feature extraction using and hamming distance for classification.
- In [14], a secure vault system based on an iris recognition system is proposed, this system uses a point-to-point feature pattern-matching algorithm and a PIC microcontroller.

In the previous section of the paper, recent work on iris detection has been presented to show what has been done recently in the field of iris detection.

In the previously mentioned works, the authors focused on the iris region. Despite the effectiveness of the above-mentioned methods for less noisy images, they often suffer a serious drop in performance when confronted with very irregular or poorly segmented masks. A solution to this problem is therefore needed

for robust, complete, and more accurate iris segmentation.

Motivated by the previous works, this paper is focused on the area of the collarette zigzag, and more precisely the lower semicircle of the collarette zigzag (see Fig. 5). The choice of the area to be studied - the lower semicircle of collarette zigzag - was not arbitrary as it is an area of the iris with a rich texture, unaffected neither by the eyelids nor by the eyelashes. The main contribution of our idea is to select the most important region of the iris, a more complex pattern, with less noise, to avoid another noise removal treatment that reduces the image quality in most cases.

In fact, the zigzag collarette region is one of the most important parts of the iris pattern because of its rich texture, its insensitivity to pupil dilation, and because it is not affected by the eyelash or eyelid. In [15], the authors found empirically that the zigzag collarette is generally concentric with the pupil and that its radius is restricted within a certain interval.

The use of the collarette area in iris recognition has led to many advances over the last decade:

- In [16], collarette boundary detection is used to improve the recognition rate. Histogram equalization and a high-pass filter are applied, after using a one-dimensional DFT, the authors used statistical information from the image to detect the collarette boundary.
- In [15], the method is based on the zigzag collarette area and crossed chord Theorem.
- In [17], based on the zigzag collarette area localization and an asymmetrical support vector machine, an effective iris recognition technique is presented.
- In [18], the authors presented the experiments by using different normalization algorithms and different iris radii in iris recognition steps. They proposed an iris localization method and a collarette localization method. In feature extraction, they proposed the Gabor wavelet filter to extract characteristics from iris images.
- In [19], the author used the Haar wavelet to localize the zigzag collarette and used a 1D Log Gabor filter for feature extraction.
- In [20], a combination of Support vector machine (SVM), artificial neural networks (ANN), and Zigzag collarette area are used to perform feature extraction for iris recognition system.
- In [2], the author proposes a new feature extraction technique using wavelets [21] combined with DLDA [22] to extract discriminative low-dimensional feature vectors from the collarette region.
- In [23] iris segmentation and normalization, algorithms based on zigzag collarette are presented.

The authors used canny edge detection and Hough transforms to localize pupil near the zigzag area. After that, the use of a Daugman Rubber Sheet Model represents an isolation zigzag collarette.

- In [24], the authors used the chain code method and zigzag collarette area with a Support Vector Machine (SVM) to enhance the iris recognition method for person identification.
- In [25], the author used a two-level segmentation method to segment the image. In the inner boundary segmentation section, They used methods such as Gauss pyramid, anisotropic scattering, thresholding, etc. . In the outer boundary, segmentation section the authors performed a zigzag collarette process using zigzag collarette methodology. Finally, the inner boundary segmentation was subtracted from the outer boundary segmentation to give the segmented iris.

Iris's recognition process consists of several steps. First, segmenting the iris region is done. After that, the normalization is carried out to transform images from Cartesian to polar coordinates. Then, the features extraction step, which is necessary to detect the features in the last stage of the classification, see [26].

Extracting efficient characteristics is the major important stage in many object recognition tasks. That is why many researchers have focused on proposing robust features for a variety of image classification stages, see [27] and references cited therein. Nowadays, a lot of attention is given to Convolutional Neural Networks (CNN) and feature learning algorithms. In this algorithm, the image is transmitted directly to the CNN, and then the algorithm extracts the best features image, see [17,27,28].

In addition to feature extraction, the researchers have attempted, through the use of the CNN, to eliminate the drawbacks of all current segmentation methods and replace much of the pre-processing and post-processing. All these advantages justify our choice to use the CNN method. Learning-based methods are an advanced type of segmentation method, as stated in [29]. Among all learning-based methods, deep learning using deep CNN is among the best known and best learning popular methods in current computer vision applications because of its accuracy and performance. Deep CNN has been implemented to detect damaged road marks [30], recognize human gender from human body images [31], detect people in night environments using a visible light camera [32] and it used for spatial feature extraction to classify lung ultrasound (LUS) videos for diagnosing COVID-19 [33]. As with CNN's brain tumor segmentation, CNN can also provide a solid platform to facilitate intensive work with accuracy and efficiency, see [34,35].

Iris applications are sensitive because they have a very complex texture. Therefore, to the best of our

knowledge, there are not many research papers on CNN related to iris segmentation, the following are the most known ones.

- In [36], CNNs are used for verification purposes and to learn relational characteristics. Also, to calculate the similarity between two iris candidates the authors used Deeplris on heterogeneous iris images.
- In [37], the authors used Deeplris Net for two research studies that focus on iris recognition rather than iris segmentation. These two studies are a visual representation of the iris and iris detection by crossed sensors.
- In [35], using fully convolutional networks (FCNs), the authors detected precise iris boundaries in non-cooperative environments. In his work, hierarchical CNNs (HCNNs) and multi-scale FCNs (MFCNs) have been used to automatically delineate iris boundaries.
- In [38], the authors used CNN entropy-based clustering to effectively segment the iris, sclera, and pupil regions. Here, CNN does the segmentation using entropy measurements.
- In [39], the authors proposed iris segmentation models based on deep learning to highlight very irregular texture areas in post-mortem iris images. The article proposed a very efficient approach to iris segmentation, called IrisParseNet based on deep learning (CNN), which differs from many iris segmentation methods.
- This article makes an interesting study by explaining the limitations of the traditional approach and the advantages of the deep learning approach for iris recognition [40].

Recent works [17,26,27,35-42] are focused on iris recognition with the CNN, but in our case, we have replaced the couple iris/CNN by the couple collarette/CNN in order to take advantage of both: CNN is the best known and most popular deep learning in current computer vision applications because of its accuracy and performance as it can efficiently extract features from the image with higher classification. In addition, deep neural networks learn high level features in hidden layers; this is one of the biggest strengths of CNN. It reduces the need for feature engineering. CNNs also correct the drawbacks of all current segmentation methods as a replacement of a large part of pre-processing and post-processing. All these advantages justify our choice to use the CNN method.

As for the choice of the zigzag collarette, this area is a part of the iris that contains enough discriminating features due to its rich texture and more complex pattern. It is less affected by pupil dilation and is usually not affected by eyelashes and eyelids which makes it less noisy thus avoiding another noise removal processing that reduces the image quality in most cases.

3. PROPOSED METHOD

The proposed method involves the implementation of the steps illustrated in Fig. 2. The first step after the acquisition of the image is the pre-processing which consists in eliminating the white points of the iris as well as other types of noise such as eyelashes and noises of salt and pepper in the image of the eye, etc. Thereafter, we pass to the stage of localization of the iris, our goal in this article is not to detect the iris itself but is to detect a part of the iris that is the collarette zigzag (more precisely the lower semi circle), the latter is the subject of our contribution, The detection of the zigzag collarette is done using the Canny contour detector followed by the circular Hough transform, after that, we perform normalization to have a fixed pattern in polar coordinates using the Daugman rubber sheet model, then we move to the stage of feature extraction using the CNN. Our choice was made on the Alex-Net pre-trained model because it is simple and efficient, at the end, a classification step by SVM is necessary to calculate the recognition rate using the accuracy formula.

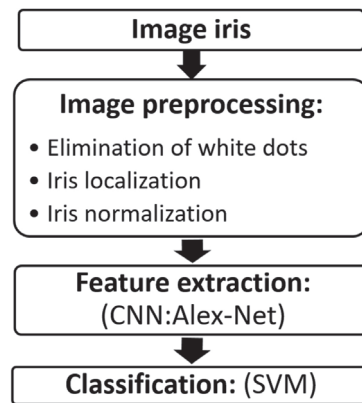


Fig. 2. Stages of iris recognition

3. 1. IMAGE ACQUISITION

The proposed method was tested on the CASIA-Iris-Lamp database. One of six subsets was collected using a hand-held iris sensor produced by OKI. A lamp was turned on/off close to the subject to introduce more intra-class variations when CASIA-Iris-Lamp was collected. Different lighting conditions result in the expansion and contraction of the pupil, which causes elastic deformation of the iris texture. This is one of the most common and difficult problems to solve in iris recognition. Therefore, CASIA-Iris-Lamp is good for studying problems of non-linear iris normalization and robust iris feature representation. The CASIA database images are JPG images with a resolution of 640*480. All iris images are 8-bit grey-level images and the file format is JPEG (584, 2020).

3. 2. IMAGE PRE-PROCESSING

The framework of our recognition system is shown in Fig. 2. In the image pre-processing part, there are three processes which are the elimination of white dots, iris localization, and Iris normalization.

3. 2. 1. Elimination of white dots

In most standard iris databases [43-46], white dots may exist in the input eye image and may remain and disrupt the iris localization process if not properly removed, see [47-51]. However, in [52], this paper proposed an effective system to suppress white dots and other extraneous noise such as eyelash threads or salt-and-pepper noise in the eye image, the result is shown in Fig. 3.

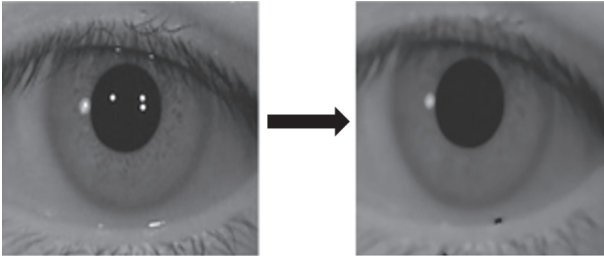


Fig. 3. Elimination of white dots

3. 2. 2. Iris localization (collarette zigzag)

• Pupil detection

During the acquisition process, changes in lighting conditions can influence the quality of the resulting iris region, and then affect the localization of the iris and subsequently the recognition result. To improve the accuracy and reliability of an iris recognition system, one must have an accurate localization of the iris region, because the performance of the subsequent steps of the system is directly dependent on the quality of the detected iris region. An ordinary iris localization system aims at detecting the two iris region boundaries: the inner (pupil-iris) boundary and the outer (iris-sclera) boundary. However, the task becomes more difficult, when eyelids and eyelashes cover parts of the iris. For this reason, a new idea has been proposed based on the detection of the collarette- and more precisely the lower semicircle of collarette-, after detecting the pupil, instead of detecting the entire iris.

The iris segmentation process starts with the detection of the pupil boundaries. for this, the Canny Edge detection is applied [53] to generate an edge map, then the circular Hough transform (CHT) is applied [54]. The standard circular Hough transform is used to detect circular shapes from a given radius in the image. The edge detection of the image is based on the calculation of the first derivatives of the intensity values. Each point in the edge map gives a circle of radius r and center (x_c, y_c) to an output array called accumulators. Then, the largest peak will be searched in the resulting array of accumulators in the parameter space using a voting procedure, the largest peak in the array of accumulators corresponds to the circle best defined by the edge points, as stated in [55,56].

In our experiment, the limit radius of pupils is between 20-60 pixels for the CASIA database. These values were found according to heuristic techniques after

examining all the images in the CASIA V4 database. After that, a voting procedure is applied to select the largest peak in the resulting accumulator array, which represents the best drawn circle by the edge points [41]. Finally, the voting procedure is implemented in the Hough space to detect the correct circle as shown in Fig. 4.

• Collarette zigzag region detection

The next processing is to isolate the zigzag collarette area (see Fig. 5). This area is generally concentric and close to the pupil. Therefore it will be very easy to detect using the formula of tracing a circle using the center coordinates of the pupil and a radius that is equal to 24 according to a study conducted by Rai. It concluded that the zigzag collarette is within 24 pixels of the pupil [19]. In the research of zigzag collarette area detection, many problems are encountered. In most cases, there is noise around the pupil which results in a geometric shape of the pupil that is not completely circular. There are still eyelashes and eyelids covering the area. Hence, researchers in this field tried to make some noise processing, as in paper [42].

In our work, this great problem is overcome by using only the lower semicircle of the collarette zigzag (see Fig. 5) which is neither affected by eyelids nor eyelashes. The principle of our idea is to select the most important region and the most complex pattern with less noise, to avoid another noise treatment that reduces the image quality in most cases.

3. 2. 3. Iris normalization (collarette zigzag)

Once the zigzag collarette is detected, normalization is implemented to produce a standard size feature vector that allows comparison between two different iris images. Stretching of the iris region is caused by dilation of the pupil with several lighting conditions, changes in the image acquisition distance, rotation of the camera or the eye, elastic distortion of the iris texture. All the above, problems affect the result of the iris comparison and may cause dimensional inconsistencies that should be resolved by normalization. As shown in Fig. 6, the iris normalization process is applied using Daugman rubber sheet mapping to transform the image iris from Cartesian to polar coordinates. The result of normalization is shown in Fig. 7 [42].

Contrast limited adaptive histogram equalization (CLAHE) is a method of contrast adjustment to get an image with uniformly distributed intensity levels. In this paper, CLAHE is applied to the normalized images (see Fig. 7). This latter is enhanced to avoid losing features, extract key points accurately, and hence increase the recognition accuracy.

The new idea here is to take only the lower semicircle of the collarette zigzag (as described previously), and divide the normalized iris into two parts, see Fig. 8. According to the image database, it's very noticeable that

the lower part of the iris is the least affected by the eye-lashes and the eyelids compared to the upper part and in most cases, this part represents a region with zero noise. In the rest of the paper, we compare the recognition rate of the iris using the full circle of collarette and the lower semicircle of collarette to further show the great improvement in the recognition rate.

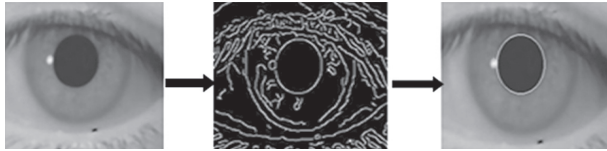


Fig. 4. Pupil detection

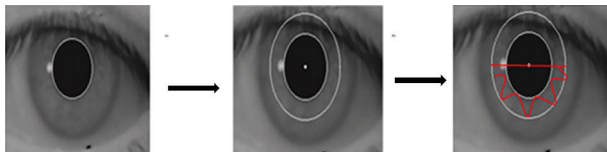


Fig. 5. Isolation of collarette zigzag area (a) and lower semicircle of zigzag collarette area (b).

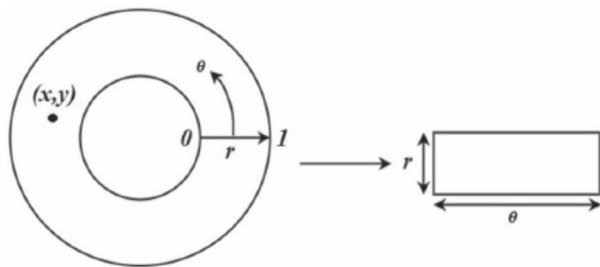


Fig. 6. Transforming the iris region from the Cartesian coordinates to the polar coordinates

3. 3. FEATURE EXTRACTION

• Convolutional Neural Network (CNN)

Alex-Net is the pre-trained network used in this paper for the feature extraction process, the choice of the Alex-Net model over another pre-trained model is not arbitrary, Alex-Net is a simple model and it offers the possibility to test performance without compromising memory and time.

The pre-trained (Alex-Net) is a Convolutional Neural Network model CNN a reduced version of the conventional Le-Net [42]. This model was conceived by the Super Vision group [57]. Fig. 9 shows the architecture of Alex-Net and Table 1 explains it further in detail.

Deep neural networks learn high-level features in the hidden layers. This is one of the greatest strengths of CNN and leads to reduced feature engineering needs. In fact, the image takes several transformations. Firstly, the image goes through many convolutional layers where the network learns new and increasingly complex features. Then, the information from the transformed image passes through the fully connected

layers and is transformed into a classification. the high-level features can be recovered from the last convolutional layers FC7.

To avoid a very long learning time using CNN, and since all layers are responsible for learning certain characteristics from the images, features can be retrieved from the network at any time during the training process. We use these extracted features as input data for a classification model with Support Vector Machines (SVM).

In our work, the characteristic vector is recovered from the fully connected layer (FC7) because we get high-level features from these convolutional layers.

3. 4. The classification

The classifier is applied after feature extraction to find the corresponding label for every test image. A lot of classifiers can be used for classification, with different types. For example, we state the Neural Network, Softmax Regression, and Support Vector Machine, see [56] for more details. In our work, a multiclass Support Vector Machine classifier is used. The SVM is a supervised learning algorithm; it constructs an optimal hyper-plane as a decision surface to maximize the margin of separation between the two classes of data. Support vectors refer to a small subset of the training observations used as support for the optimal location of the decision surface.

After loading the database, it is divided in two parts: 70% for training and 30% for testing. Then, we extract the class labels from the training and the test data. The principle of the SVM classification algorithm is to place each data point in an n-dimensional space, where n is the number of characteristics. The value of each character is the value of a particular coordinate. Later, we perform the classification by searching for the hyper-plane that differentiates the two classes very well. The SVM algorithm will therefore classify the images and finally calculate the "Accuracy" or learning rate, i.e. the efficiency of the method or the accuracy of the classification. This value expresses the fraction of labels that the network correctly predicts, as defined by the formula (1).

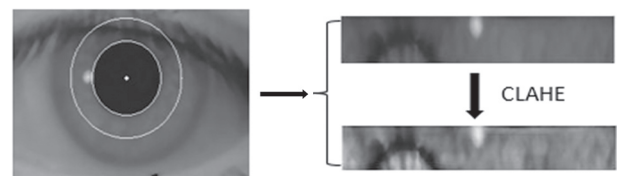


Fig. 7. Iris normalization and enhancement

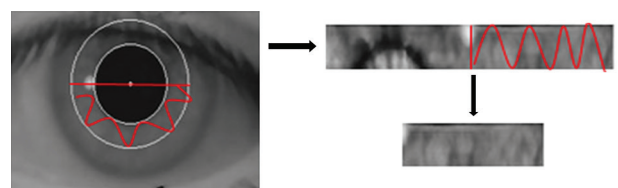


Fig. 8. Iris normalization: lower semicircle of collarette region

Table 1. The Alex-Net Layer [17]

Type of Layer	No. of Filter	Feature Map Size (height x width x channel)	Kernel Size	No. Of Stride	No. of Padding
Image input layer		227x227x3			
(1st convolutional layer) Relu-1	96	55x55x96	11x11	4x4	0x0
Cross-channel normalization Max pooling1	1	27x27x96	3x3	2x2	0x0
(2nd convolutional layer) Relu-2	256	27x27x256	5x5	1x1	2x2
Cross-channel normalization Max pooling2	1	13x13x256	3x3	2x2	0x0
3rd convolutional layer) Relu-3	384	13x13x384	3x3	1x1	1x1
(4th convolutional layer) Relu-4	384	13x13x384	3x3	1x1	1x1
(5th convolutional layer) Relu-5	256	13x13x256	3x3	1x1	1x1
Max pooling5	1	6x6x256	3x3	2x2	0x0
Fully connected layer-6 (fc6)		4096x1			
Relu-6		4096x1			
Fully connected layer-7 (fc7)		4096 x1			
Relu-7		4096 x1			
Fully connected layer-8 (fc8) Softmax layer		1000x1			
Output layer		1000 class			

$$Accuracy = \frac{\text{correctly classified Iris Images}}{\text{Total Number}} \times 100 \quad (1)$$

3. 5. EXPERIMENTAL RESULTS AND ANALYSIS

Our experiments are performed in MATLAB R2018a on a PC Intel core i5, RAM 6 Gb, and a Windows operating system 64 bits. The images used in our experiments come from the CASIA V4-Iris-Lamp image database. This most recent version of CASIA was used with CNN to study the effectiveness of using zigzag collarette region in iris recognition.

For our experiment, 400 images were used from the CASIA database (40 classes and 10 samples per class), several experiments are performed with 100 images (10 classes, 10 samples), 200 images (20 classes, 10 samples), 300 images (10 classes, 10 samples), 400 images (40 classes, 10 samples) as mentioned in Table 2. Alex-Net is used for feature extraction. The data is divided into two phases, 70% for training and 30% for testing. All images in the database are resized to 227 by 227 which is the input size of the Alex-Net. All grayscale images are converted to RGB. At the end, the features learned using the CNN (Alex-Net) and extracted from the layer FC7 will be injected into the multiclass SVM classifier for image classification.

The proposed idea in the previous section has been implemented and the accuracy was calculated using the full circle of the collarette zigzag and compared with accuracy calculated using the lower semicircle of the collarette zigzag. The experimental result is shown in Table 2.

The pre-trained CNN model used was already trained on more than a million images as the feature extractor and the SVM as the classifier. Alex-Net with the SVM classifier achieved good accuracy with a fairly short training time, on the order of seconds to minutes only. The advantage of the pre-trained CNN model is the elimination of the laborious task of feature engineering, making it easier to learn the new assigned task. Table 2 illustrates the accuracy rate with the different cases studied: 100 images, 200 images, 300 images, and 400 images as explained below; for each collared zigzag image, for the full circle of collarette zigzag versus its lower semicircle. The result shows that the best accuracy is found with the samples when using the lower semicircle of the collarette zigzag. Based on the results, our new idea that uses only the lower semicircle of the collarette achieved the highest recognition accuracy compared with the old methods that use the whole collarette region, [2,16,18-23,25,51,58].

In this study case, we have done several training by increasing the number of classes: (10,20,30,40) and keeping the number of samples always fixed, we notice that the accuracy decreases, on the other hand, if we increase the number of samples per class (something impossible with the CASIA database) the learning by CNN will improve greatly and the accuracy too.

Table 2. Accuracy; collarette full circle and collarette lower semicircle.

Samples (images)	Collarette: Full circle	Collarette:lower semi-circle (our proposition)
100	93.33%	100%
200	91.67%	100%
300	88.89%	100%
400	88.33%	94.17%

Table 3. Performance parameters

Collarette: Full circle				
Sensitivity	Specificity	Precision	Recall	Fscore
0.91	0.997	0.88	0.91	0.87
Collarette: lower semi-circle (our proposition)				
Rensitivity	Specificity	Precision	Recall	Fscore
0.94	0.998	0.95	0.94	0.93

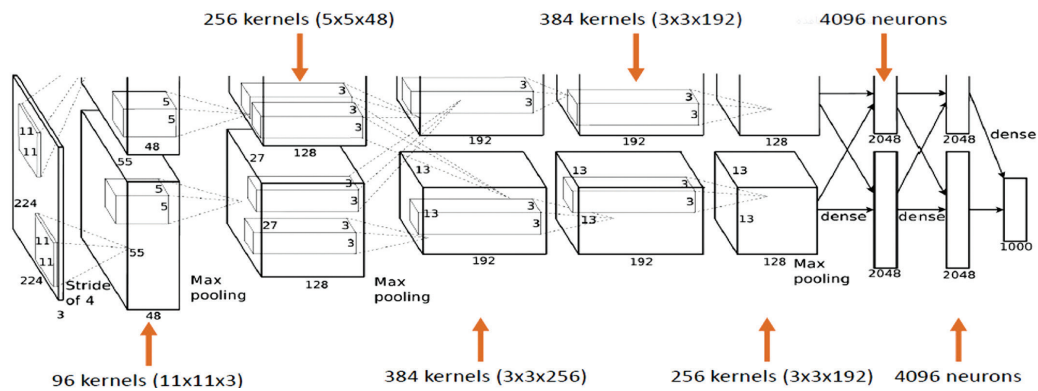


Fig. 9. Detailed architecture of Alex-Net [17]

Output Class	001	002	003	004	005	006	007	008	009	010	Accuracy
001	3 10.0%	0 0.0%	100%								
002	0 0.0%	3 10.0%	0 0.0%	100%							
003	0 0.0%	0 0.0%	3 10.0%	0 0.0%	100%						
004	0 0.0%	0 0.0%	0 0.0%	3 10.0%	0 0.0%	0 0.0%	0 0.0%	0 0.0%	0 0.0%	0 0.0%	100%
005	0 0.0%	0 0.0%	0 0.0%	0 0.0%	3 10.0%	0 0.0%	0 0.0%	0 0.0%	0 0.0%	0 0.0%	100%
006	0 0.0%	0 0.0%	0 0.0%	0 0.0%	0 0.0%	3 10.0%	0 0.0%	0 0.0%	0 0.0%	0 0.0%	100%
007	0 0.0%	0 0.0%	0 0.0%	0 0.0%	0 0.0%	0 0.0%	3 10.0%	0 0.0%	0 0.0%	0 0.0%	100%
008	0 0.0%	3 10.0%	0 0.0%	0 0.0%	100%						
009	0 0.0%	3 10.0%	0 0.0%	100%							
010	0 0.0%	3 10.0%	100%								
Overall	100%	100%	100%	100%	100%	100%	100%	100%	100%	100%	100%

Fig. 10. Confusion matrix for first test (Collarette: lower semi-circle)

Output Class	001	002	003	004	005	006	007	008	009	010	Accuracy
001	3 10.0%	0 0.0%	1 3.3%	0 0.0%	0 0.0%	0 0.0%	0 0.0%	1 3.3%	0 0.0%	0 0.0%	60.0%
002	0 0.0%	3 10.0%	0 0.0%	0 0.0%	0 0.0%	0 0.0%	0 0.0%	0 0.0%	0 0.0%	0 0.0%	100%
003	0 0.0%	0 0.0%	2 6.7%	0 0.0%	0 0.0%	0 0.0%	0 0.0%	0 0.0%	0 0.0%	0 0.0%	100%
004	0 0.0%	0 0.0%	0 0.0%	3 10.0%	0 0.0%	0 0.0%	0 0.0%	0 0.0%	0 0.0%	0 0.0%	100%
005	0 0.0%	0 0.0%	0 0.0%	0 0.0%	3 10.0%	0 0.0%	0 0.0%	0 0.0%	0 0.0%	0 0.0%	100%
006	0 0.0%	0 0.0%	0 0.0%	0 0.0%	0 0.0%	3 10.0%	0 0.0%	0 0.0%	0 0.0%	0 0.0%	100%
007	0 0.0%	0 0.0%	0 0.0%	0 0.0%	0 0.0%	0 0.0%	3 10.0%	0 0.0%	0 0.0%	0 0.0%	100%
008	0 0.0%	0 0.0%	0 0.0%	0 0.0%	0 0.0%	0 0.0%	0 0.0%	2 6.7%	0 0.0%	0 0.0%	100%
009	0 0.0%	0 0.0%	0 0.0%	0 0.0%	0 0.0%	0 0.0%	0 0.0%	0 0.0%	3 10.0%	0 0.0%	100%
010	0 0.0%	0 0.0%	0 0.0%	0 0.0%	0 0.0%	0 0.0%	0 0.0%	0 0.0%	0 0.0%	3 10.0%	100%
Overall	100%	100%	66.7%	100%	100%	100%	100%	66.7%	100%	100%	93.3%

Fig. 11. Confusion matrix for second test (Collarette: Full circle)

In addition to the accuracy, the performance analysis of the two experiments (Collarette: Full circle/ Collarette: lower semi-circle) was based on the most used evalu-

ation measures for statistical tests, such as (sensitivity, specificity, precision, recall, fscore) [59] in order to further verify the performance of our CNN/SVM classifier, for those we performed the first test with 100 images (10 classes) -as an example- and compute the confusion matrix to display the classification results of our tests . By calculating the statistical parameters, the performance of our system is evaluated and presented in Table 3. After the analysis, we can easily see the superiority of all parameters in the case of the lower semi-circle of Collarette and also in the confusion matrix, see Fig. 10 and Fig. 11.

4. CONCLUSION

In this paper, we presented an iris recognition method for person identification based on CNN and the zigzag collarette region. The impact of the choice of the CNN characterization on the lower semicircle of the collarette region allowed us at the same time to target the least noisy area of the collarette with an optimal feature vector. We used an Alex-Net model pre-trained on over a million images as a feature extractor, and a multi-class SVM for classification. Alex-Net with the SVM classifier achieved good accuracy with a fairly short learning time, on the order of seconds to minutes. The iris detection rate using the full semicircle of collarette zigzag was compared with the detection rate using only its lower semicircle. Images from the CASIA-Iris-Lamp V4 database were used to evaluate our approach. Version 4 of the CASIA database has been applied for the first time to study the contribution of the collarette zigzag area with the CNN for iris recognition.

The choice of lower semicircle of collarette had a very effective contribution on the accuracy as mentioned in Table 2, we notice that the accuracy using lower semicircle of collarette is always higher than that of the full of circle collarette. The classification of the test set is represented by a confusion matrix. It shows the performance of a classifier on a test data set. If a class is mislabeled as the other class among several classes, we can easily identify it from a confusion matrix, other statistical parameters have been prospected; the results confirm our choice (low collarette/CNN) We have chosen the SVM algorithm because it can be adapted to classification problems involving more than 2 classes. In contract to a neural net-

work which requires a lot of work to determine the right structure and parameters to use, SVM perform well even without any preparation. CNN facilitates the task of extracting the characteristics and making it easier to learn the new task assigned and extract more features from the image, allowing an SVM classifier to be better informed and achieve good accuracy. The crucial advantage of our combined approach (CNN/SVM) is that we can extract enough features (4096 features from the FC7 layer) from each image by representing the detail of each image from a pre-trained Alex-Net CNN model, and take advantage of the SVM to classify the features, saving time.

For future works, we plan to use data augmentation to increase the data artificially by learning a good amount of data. It is also interesting to train the data on other pre-trained models and finally use other databases.

5. ACKNOWLEDGMENTS

The authors would like to thank the DGRSDT (General Directorate of Scientific Research and Technological Development) - MESRS (Ministry of Higher Education and Scientific Research), ALGERIA, for the financial support of LERICA Laboratory(Laboratory for Study and Research in Instrumentation and Communication Annaba).

6. REFERENCES

- [1] H. K. Rana, S. Azam, R. Akhtar, J. M. W, Quinn, M. A. Moni, "A fast iris recognition system through optimum feature extraction", *PeerJ Computer Science*, 2019
- [2] A. Joshi, A. Gangwar, Z. Saquib, "Collarette Region Recognition based on Wavelets and Direct Linear Discriminant Analysis", *International Journal of Computer Applications*, Vol. 40, No. 9, 2012, pp.0975-8887.
- [3] R. A. Ali, A. A. Maryoosh, D. N. George, W. R. Humood, "Iris images encryption based on QR code and chaotic map", *TELKOMNIKA Telecommunication, Computing, Electronics and Control*, 2020, Vol. 18, No. 1, pp. 289-300.
- [4] D. F. Santos, H. E. Espitia, "Detection of uveal melanoma using fuzzy and neural networks classifiers", *TELKOMNIKA Telecommunication, Computing, Electronics and Control*, 2020, Vol. 18, No. 4, pp. 2213-2223.
- [5] P. S. Sanjekar, J. B. Patil, "Multimodal biometrics with serial, parallel and hierarchical mode at decision level fusion", *Indonesian Journal of Electrical Engineering and Computer Science*, Vol. 16, No. 3, 2019, pp. 1303-1310.
- [6] H. Ohmaid, S. Eddarouich, A. Bourouhou, M. Timouyas, "Iris segmentation using a new unsupervised neural approach", *IAES International Journal of Artificial Intelligence*, Vol. 9, No. 1, 2020, pp. 58-64.
- [7] A. S. Akinfende, A. L. Imoize, O. S. Ajose, "Investigation of iris segmentation techniques using active contours for non-cooperative iris recognition", *Indonesian Journal of Electrical Engineering and Computer Science*, Vol. 19, No. 3, 2020, pp. 1275-1286.
- [8] N. Bounegta, A. Basso, M. Beladgham, "Eyelids, eyelashes detection algorithm and hough transform method for noise removal in iris recognition", *Indonesian Journal of Electrical Engineering and Computer Science*, Vol. 18, No. 2, 2020, pp. 731-735.
- [9] R. F. Soliman, M. Amin, F. E. Abd El-Samie, "Cancelable Iris recognition system based on comb filter", *Multimedia Tools and Applications*, Vol. 79, 2019, pp. 2521-2541.
- [10] S. Adamović, V. Mišković, N. Maček, M. Milosavljević, M. Šarac, M. Saračević, M. Gnjatović, "An efficient novel approach for iris recognition based on stylometric features and machine learning techniques", *Generation Computer Systems*, Vol. 107, 2020, pp. 144-157.
- [11] Y. Jusman, S. C. Ng, K. Hasikin, "Performances of proposed normalization algorithm for iris recognition", *International Journal of Advances in Intelligent Informatics*, Vol. 6, No. 2, 2020, pp. 161-172.
- [12] N. Ahmadi, G. Akbarizadeh, "Iris tissue recognition based on GLDM feature extraction and hybrid MLPNN-ICA classifier", *Neural Computing and Applications*, Vol. 32, 2018, pp. 2267-2281.
- [13] M. S. Chetali, R. V. Babar, "Design of Iris Recognition Biometric System", *International Journal of Research in Engineering, Science and Management*, Vol. 2, No. 6, 2019, pp. 445-448
- [14] A. Kour, B. Gupta, "Secure Vault System using Iris Biometrics and PIC Microcontroller", *International Research Journal of Engineering and Technology*, Vol. 6, No. 3, 2019.
- [15] X. F. He, P. F. Shi, "An Efficient Iris Segmentation Method for Recognition", *International Conference on Pattern Recognition and Image Analysis*, LNCS 3687, 2005, pp. 120-126.

- [16] H. Sung, J. Lim, J. Park, L. Yillbyung, "Iris Recognition Using Collarette Boundary Localization", Proceedings of the 17th International Conference on Pattern Recognition, Cambridge, UK, 26-26 August 2004.
- [17] M. G. Alaslani, L. A. Elrefaei, "Convolutional neural network based feature extraction for iris recognition", International Journal of Computer Science & Information Technology, Vol. 10, No 2, 2018, p. 10206.
- [18] R. H. Jeng, S. W. Chen, L. Hsieh, "Does Collarette of Iris Work for Recognizing Persons?", Proceedings of the 7th International Multi-Conference on Computing in the Global Information Technology, 2012.
- [19] H. Rai, A. Yadav, "Iris recognition using combined support vector machine and Hamming distance approach", Expert Systems with Applications, Vol. 41, 2014, pp.588-593.
- [20] P. Punyani, A. Kumar, R. Gupta, "An optimized Iris Recognition System using MOGA followed by Combined Classifiers", International Journal of Research in Advent Technology, Vol. 4, No. 3, 2016.
- [21] M. W. Frazier, "An Introduction to Wavelets through Linear algebra", Springer, 1999.
- [22] H. Yu, J. Yang, "A Direct LDA Algorithm for High-Dimensional Data with Application to Face Recognition", Pattern Recognition, Vol. 34, 2001, pp. 2067-2070.
- [23] M. R. Faundra, D. R. Sulistyaningrum, "Iris Segmentation and Normalization Algorithm Based on Zigzag Collarette", Journal of Physics Conference Series, Vol. 795, 2017.
- [24] K. Roy, P. Bhattacharya, "An Iris Recognition Method Based On Zigzag Collarette Area and Asymmetrical Support Vector Machines", Proceedings of the IEEE International Conference on Systems, Man, Cybernetics, Taipei, Taiwan, 8-11 October 2006.
- [25] S. S. Jauro, R. Yadav, "An efficient interior and exterior boundary detection- based two level iris segmentation", International Journal of Information and Computer Security, Vol. 13, No.1, 2020.
- [26] S. Minaee, A. Abdolrashidi, Y. Wang, "An experimental study of deep convolutional features for iris recognition", Proceedings of the Signal Processing in Medicine and Biology Symposium, Philadelphia, PA, USA, 3 December 2016, pp. 1-6.
- [27] S. Minaee, A. Abdolrashidi, Y. Wang, "Iris recognition using scattering transform and textural features", Proceedings of the Signal Processing and Signal Processing Education Workshop, Salt Lake City, UT, USA, 9-12 August 2015, pp. 37-42.
- [28] S. Minaee, A. Abdolrashidi, Y. Wang, "Face Recognition Using Scattering Convolutional Network", arXiv preprint, 2016 arXiv:1608. 00059.
- [29] H. Li, Z. Sun and T. Tan, "Robust iris segmentation based on learned boundary detectors", In Proceedings of the International Conference on Biometrics, New Delhi, India, 29 March-1 April 2012, pp. 317-322.
- [30] H. Vokhidov, H. G. Hong, J. K. Kang, T. M. Hoang, K. R. Park, "Recognition of damaged arrow-road markings by visible light camera sensor based on convolutional neural network", Sensors, Vol. 16, 2016, p. 2160.
- [31] D, T. Nguyen, K, W. Kim, H, G. Hong, J, H. Koo, M, C. Kim, K, R. Park, "Gender recognition from human-body images using visible-light and thermal camera videos based on a convolutional neural network for image feature extraction", Sensors, Vol. 17, 2017, p. 637.
- [32] J. H. Kim, H. G. Hong, K.R. Park, "Convolutional neural network-based human detection in nighttime images using visible light camera sensors", Sensors, Vol. 17, 2017, pp. 1-26.
- [33] B. Barros, P. Lacerda, C. Albuquerque, A. Conci, "Pulmonary COVID-19: Learning Spatiotemporal Features Combining CNN and LSTM Networks for Lung Ultrasound Video Classification", Sensors, Vol. 21, No. 16, 2021, p. 5486.
- [34] S. Pereira, A. Pinto, V. Alves, CA. Silva, «Brain tumor segmentation using convolutional neural networks in MRI images», IEEE Transactions on Medical Imaging, Vol. 35, 2016, pp. 1240-1251.
- [35] M. Arsalan, H. G. Hong, R. A. Naqvi, M. B. Lee, M. C. Kim, D. S. Kim, C, S. Kim, K, R. Park, "Deep Learning-Based Iris Segmentation for Iris Recognition in Visible Light Environment", Symmetry, Vol. 9, 2017, p. 263.
- [36] N. Liu, M. Zhang, H. Li, Z. Sun, T. Tan, "Deeplris: Learning pairwise filter bank for heterogeneous iris verification", Pattern Recognition Letters, Vol. 82, 2016, pp. 154-161.

- [37] A. Gangwar, A. Joshi, "DeepIrisNet: Deep iris representation with applications in iris recognition and cross-sensor iris recognition", Proceedings of the IEEE International Conference on Image Processing, Phoenix, AZ, USA, 25-28 September 2016, pp. 2301-2305.
- [38] M. Pathak, N. Srinivasu, V. Bairagi, "Effective segmentation of sclera, iris and pupil in noisy eye images", TELKOMNIKA Telecommunication, Computing, Electronics and Control, Vol. 17, No. 5, 2019, pp. 2346-2354.
- [39] M. Trokielewicz, A. Czajka, P. Maciejewicz, "Post-mortem Iris Recognition with Deep-Learning-based Image Segmentation", Image and Vision Computing, Vol. 94, 2019.
- [40] J. Rahman, M. Noridayu, B. Manshor and Li. S. Afendey, "Iris Recognition Development Techniques: A Comprehensive Review", Complexity, 2021, 6641247.
- [41] A. S. Al-Waisy, R. Qahwaji, S. Ipson, S. Al-Fahdawi, T. A. Nagem, "A multi-biometric iris recognition system based on a deep learning approach", Pattern Analysis and Applications, Vol. 27, 2018, pp. 783-802.
- [42] K. Nguyen, C. Fookes, A. Ross, S. Sridharan, "Iris Recognition with Off-the-Shelf CNN Features: A Deep Learning Perspective", IEEE Access, Vol. 6, 2017, pp. 18848-18855.
- [43] CASIA iris database, <http://www.idealtest.org/find-TotalDbByMode.do?mode=Iris>, (accessed: 2012).
- [44] UBIRIS iris database, <http://iris.di.ubi.pt/>, (accessed: 2012).
- [45] IITD iris database, <http://www.iitd.ac.in/>, (accessed: 2012).
- [46] MMU iris databases, <http://pesona.mmu.edu.my/~ccteol/>, (accessed: 2012).
- [47] J. G. Daugman, "High confidence visual recognition of persons by a test of statistical independence", IEEE Transactions on Pattern Analysis and Machine Intelligence, Vol. 15, 1993, pp. 1148-1161.
- [48] K. Roy, P. Bhattacharya, "Collarette Area Localization and Asymmetrical Support Vector Machines for Efficient Iris Recognition", Proceedings of the 14th International Conference on Image Analysis and Processing, Modena, Italy, 10-14 September 2007.
- [49] W. Sankowski, K. Grabowski, M. Napieralska, M. Zubert, A. Napieralski, "Reliable algorithm for iris segmentation in eye image", Image and Vision Computing, Vol. 28, 2010, pp. 231-237.
- [50] P. D. Almeida, "A knowledge-based approach to the iris segmentation problem", Image and Vision Computing, Vol. 28, 2010, pp. 238-245.
- [51] Z. He, T. Tan, Z. Sun, X. Qiu, "Toward accurate and fast iris segmentation for iris biometrics", IEEE Transactions on Pattern Analysis and Machine Intelligence, Vol. 31, 2009, pp. 1670-1684.
- [52] F. Jan, I. Usman, S. Agha, "Iris localization in frontal eye images for less constrained iris recognition systems", Digital Signal Processing, Vol. 22, 2012, pp. 971-986.
- [53] N. Singh, D. Gandhi, K. P. Singh, "Iris recognition system using a canny edge detection and a circular Hough transform", International Journal of Advances in Engineering & Technology, Vol. 1, No. 2, 2011, pp. 221-228.
- [54] S. Sangwan, R. Rani, "A Review on: Iris Recognition", International Journal of Computer Science and Information Technologies, Vol. 6, 2015, pp. 3871-3873.
- [55] A. S. Al-Waisy, R. Qahwaji, S. Ipson, S. Al-Fahdawi, "A fast and accurate iris localization technique for healthcare security system", Proceedings of the IEEE International Conference on Computer and Information Technology; Ubiquitous Computing and Communications; Dependable, Autonomic and Secure Computing; Pervasive Intelligence and Computing, Liverpool, UK, 26-28 October 2015, pp 1028-1034
- [56] S. Minaee, Y. Wang, "Palmprint Recognition Using Deep Scattering Convolutional Network", arXiv preprint, 2016 arXiv:1603.09027.
- [57] A. Krizhevsky, I. Sutskever, G. E. Hinton, "Imagenet classification with deep convolutional neural networks", Communications of the ACM, Vol. 60, No. 6, 2017, pp. 84-90.
- [58] D. S. Jeong, J. W. Hwang, B. J. Kang, K. R. Park, C. S. Won, D. K. Park, J. Kim, "A new iris segmentation method for non-ideal iris images", Image and Vision Computing, Vol. 28, 2010, pp. 254-260.
- [59] S. Almabdy, L. Elrefaei, "Deep convolutional neural network-based approaches for face recognition", Applied Sciences, 2019, Vol. 9, No. 20, p. 4397.

Performance Assessment of TSO–DSO using Volt-Var Control at Smart-Inverters: Case of Vestfold and Telemark in Norway

Case Study

Victor Astapov

Tallinn University of Technology
Department of Electrical Engineering and
Mechatronics
Ehitajate tee 5, Tallinn, Estonia
victor.astapov@taltech.ee

Sergei Trashchenkov

Pskov State University
Institute of Engineering Sciences
L.Tolstoy St., 4, Pskov, Russia
trashchenkov@gmail.com

Francisco Gonzalez-Longatt

University of South-Eastern Norway
Department of Electrical engineering, Information
Technology and Cybernetics
Office C224b, Kjølnes Ring 56, 3918, Porsgrunn,
Norway
fglongatt@fglongatt.org

Danijel Topic

University of Osijek,
Faculty of Electrical Engineering, Computer Science
and Information Technology
Osijek, Croatia
Kneza Trpimira 2b, 31000 Osijek

Abstract – The massive penetration of distributed energy resources (DERs) in distribution networks provides a strategic opportunity for the distribution system operator (DSO) to coordinate the assets appropriately and offer services to the transmission systems. The IEEE std. 1547-2018 introduced a control mechanism to enable the power electronic converters (PECs) to offer several services, including voltage regulation by controlling the reactive power injection/absorption; this type of PECs is also known as "smart inverter". The participation of the smart-inverters in the voltage regulation with a novel customer-centred piece of legislation and markets provide the DSO with powerful tools to enforce very positive TSO/DSO interactions. This research paper presents a comprehensive assessment of the steady-state performance provided by voltage control at the smart-inverters to the TSO – DSO system. The assessment includes analysing main indicators using time series considering short term (24-hours, 1-minute resolution) and long-term (one-year) horizon. In this paper, the three leading indicators are used as criteria for the assessment: total energy losses voltage profile in the TSO–DSO system and the power flow interaction at the interface between the systems. The assessment is based on numerical results using the DigSILENT PowerFactory simulation tool, where the voltage controllers have been implemented, and regional electrical system in south-eastern Norway, the area of Vestfold and Telemark as been used for illustrative purposes.

Keywords: Ancillary service, control, distribution grid, DG, DSO, PowerFactory, reactive power control, reactive power management, RES, smart inverter, TSO, voltage control.

1. INTRODUCTION

Electrical power systems are facing many challenges nowadays; one of those challenges is the need to adapt the distributions network to increase the growing integration of renewable-based generation (and storage) at the demand side to allow the customer more active participation in the electricity trade. The old concept of passive and one-directional power flows distribution networks must change. *Distribution system operators* (DSOs) must take advantage of the new interest of customers in installing new low-carbon technologies and the market possibilities of compensating the customer for offering services to the grid. Consequently, the

customer-centred active distribution network (ADN) must be flexible and able to adapt, all of the low carbon technologies require power electronic converters (PECs) as interfaces to the grid, such as the case of solar PV (which outputs DC power) or microturbines (high-frequency AC power) [1]. The so-called *power electronic interfaces* (PEI) offer an outstanding instrument to provide controllability features to the DSO; it is particularly true considering the technological advances reached by the development of the smart grids [3], [4].

Modern PEIs are intended to play a crucial role in frequency and voltage control in the ADN, and also, the PEI (when appropriately coordinated) also facili-

tates participation in black start strategies. The IEEE Standard 1547-2018 [5], *IEEE Standard for Interconnection and Interoperability of Distributed Energy Resources with Associated Electric Power Systems Interfaces*, provided a modern way to look at the PEI and allow getting over the limitations of low penetrations of the power converter based *distributed energy resources* (DER) in the electrical networks, and add advanced features on DER, like smart features to *solar PV inverters* [6] and *wind generator inverters* [7]. The IEEE std 1547-2018 [5] created a new tendency in the power electronic converter industry, the so-called "smart inverter" [1]. The IEEE 1547-2018 is a crucial enabler to the low carbon technologies in the distribution network, making room for prosumers to offer services to the DSO and then to the *transmission system operator* (TSO) [8].

The smart inverter is a straightforward concept; it is a PEI that is enabled with novel features and functionalities; it is enhanced capabilities, especially the digital architecture, bidirectional communications capability and robust software infrastructure [9], [10].

The IEEE std 1547-2018 and the concept of a smart inverter allows the drawing of the main features of the so-called: *Smart solar photovoltaic inverters*; the features comprise at a minimum the following [8], [11]:

- Voltage ride through
- Frequency ride-through
- Voltage support
- Frequency support, and
- Ramp rates.

The modern IEEE Std. 2030.7, *IEEE Standard for the Specification of Microgrid Controllers* [12], [13] is a crucial document on defining the operation and control so the microgrid; it introduces the fundamental concept of the *Microgrid Energy Management System* (MEMS). In addition, IEEE Std. 2030.7 contains the specifications of the control functions that distinguish the microgrid as a system that can manage itself. Thus, the microgrid (under the concept of IEEE Std. 2030.7) can operate autonomously or grid-connected, seamlessly connect to the utility grid, and enable the microgrid to be disconnected from the utility grid to exchange power supply of ancillary services [14], [15].

The digitalisation of the electricity networks is a reality; the power systems are taking advantage of digital technologies to transform the electricity sector fundamentally. Moreover, the digitalisation of the power systems has cleared the path to overcome barriers (in the past) and allowed a very active and dynamic interaction between TSOs and DSOs.

The increased interaction between DSOs and TSOs can enable better utilisation of DERs -especially at the demand side, increased system flexibility and optimisation of investments in grid infrastructure. However, also, the interactions between TSO - DSO has the po-

tential to overcome several of the traditional problems in electrical networks [11], [13], [16]: relieving congestion of Transmission-Distribution interface (potential to defer infrastructure investment), relief of congestion of transmission lines and distribution lines, fully managed voltage support (TSO↔DSO), balancing challenge, (anti-) islanding, re-synchronisation & black-start and coordinated protection.

A more adaptive and flexible TSO-DSO operating approach takes advantage of the smart-inverters to provide voltage control of the entire system and take advantage of reactive power/voltage control. The TSO-DSO collaborative approach considered in this scientific paper appropriately employ the smart-inverter installed at the prosumers to provide voltage support to the entire system by adjusting the reactive power injection/absorption at their interface, taking advantage of DGs reactive power capability. The European Grid Code, *Demand and Connection Code* (DCC) [17] established the new distribution systems are requested to have the technical capacity to restrain the reactive power flowing upwards the transmission system at low active power consumption, that is below 25% of their maximal power import capacity [18].

This research paper is dedicated to introducing and assessing the effect of smart inverters voltage control on the quasi-dynamic performance of the TSO – DSO system, considering several time scales [19]. The TSO–DSO system's quasi-dynamic performance assessment is based on two leading indicators; the total energy losses and the voltage profile in the TSO - DSO system. The indicators are calculated from the numerical results obtained in quasi-dynamic simulations using a well-known power system analysis software, DigSILENT PowerFactory. Furthermore, to show the suitability of the proposed approach in a realistic fashion, the assessment in this paper considers the regional electrical system of Vestfold and Telemark, located in the south-eastern part of Norway. This scientific paper is structured in five sections. Section II presents the primary voltage-control operating mode of the smart inverter; Section III is focused on establishing the critical aspects of TSO-DSO modelling. Section IV is dedicated to assessing the impact of voltage control of smart-inverters in multi-time scale quasi-dynamic performance of the TSO – DSO regional system of Vestfold and Telemark, Norway. Finally, this scientific paper closes with Section V presenting the main conclusions and findings. One main contribution of this paper is making evident that reaching the minimum total energy losses implies a compromise between the TSO/DSO losses; as a consequence, enabling the interaction TSO/DSO that reaches a global benefit for all parties requires sub-optimum losses at each individual system.

2. VOLT-VAR CONTROL IN SMART CONVERTERS

Voltage control in a traditional transmission system is reached by several mechanisms where the provision/consumption of reactive power is the central con-

trol element. Some of the mechanism used in voltage control in traditional transmission includes the use of power transformers equipped with an *on-load tap changer* (OLTC). The scientific literature is rich in many other classical Volt-var control when dealing with voltage control at transmission-level [20-22]: shunt capacitors/reactors, transformer tap changers, synchronous generators, synchronous condensers, FACTS, e.g., STATCOM, SVC and HVDC. The voltage control at the distribution network uses several reactive power sources/control [23], [24] such as voltage regulators, transformer tap changers, shunt capacitors. The power utilities included in the grid code specific connection requirements generation units, and those requirements vary from country to country, installed capacity and the voltage level of connection, and some other factors.

The smart-inverter concept allows the power-converter based distributed energy resources (DER) units to produce/absorb reactive power depending on a control rule that can be defined in many ways. For instance, the smart inverter working in control mode can adjust the operating power factor to absorb reactive power at the controlled point to bring the high voltage down within standard limits and inject reactive power to increase voltage level, which consequently changes reactive power flow in the grid. A vital element of the modern voltage control aforementioned is that nowadays, the controlled node is not necessarily the connection point of the DER unit. It can also be a common coupling point (PCC), a boundary between TSO and DSO, or a specific node in the grid. The inclusion of digital communication technologies basically reaches the flexibility in the location of the control node. Today the additional regulation types such as constant voltage (const U), constant power factor (const $\cos \varphi$), $Q(P)$, or $P(U)$ is not a rarity, especially for high capacity (multi-MW) DG. For example, a DER in the low voltage network in Germany must implement at least one of those voltage control functions [25], [26].

The explanation of such control methods is widely presented in many scientific publications [27-29], but the authors would like to highlight a few key points relevant to the control strategies used in this paper and how they are implemented in the power systems simulation environment. The technological advances on PEC and the new IEEE std 1547-2018 makes the smart-inverter a desirable solution to provide Volt-var control and positively impact the distribution systems. Smart-inverter supports the following control modes, which are considered in the paper: (i) Constant reactive power, (ii) Constant voltage, (iii) Voltage Q-droop, (iv) Q(U)-Characteristic (see Fig. 1), and the control can be implemented locally and remotely. Technically ii-iv modes are pretty similar, despite that constant voltage controller implementation does not have a deadband and is accordingly stricter. In such mode, reactive power fluctuations are more often compared to (iii) and (iv).

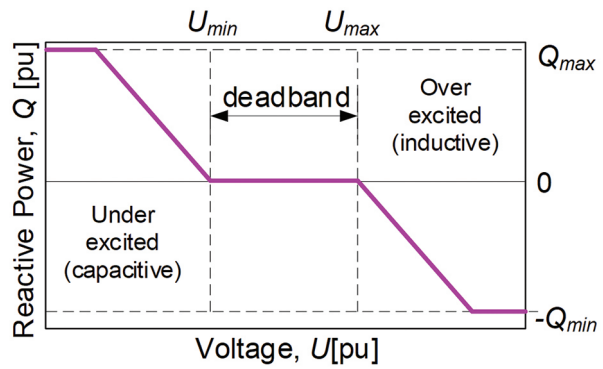


Fig. 1 Illustrative representation of the $Q(U)$ -characteristic

As mentioned before, the model includes the possibility of controlling parameters locally and at some specific point in the network. In this paper, the point of control is the boundary between TSO and DSO networks. The so-called wide-area control is basically a centralised controller that takes measurements and then, using a predefined control rule, defines the operational setpoints of the smart-inverters. Depending on the control model defined, the following parameters should be set up: reactive power setpoint (operation considering constant power factor); voltage setpoint U_{setp} and reactive droop Q_{droop} in Mvar/pu (operation considering constant voltage). The wide-area control use measurement devices located at the branch or boundary where the controller is intended to fulfil the control rule. The voltage setpoint is modified depending on the reactive power flow at the Q-measurement point as follows:

$$U'_{setp} = U_{setp} + \frac{Q_{meas}}{Q_{droop}} \quad (1)$$

where: U_{setp} is the voltage set point in pu. of the busbar, U'_{setp} represents the voltage set point in pu., including the droop characteristic, and Q_{meas} and Q_{droop} are the measured reactive power in Mvar and droop in Mvar/pu, respectively.

Moreover, for station control contribution of the different reactive power sources to the control of the voltage is specified. Every source is assigned a contribution factor (K_p) that indicates the percentage to feed an actual value, in addition to its set point. This factor is calculated according to five different options, including dispatched active power, individual reactive power, or the rated power as in our case.

During the operation, especially in remote control, demands for reactive power could be outside the inverter capability limits. Another boundary is derived by the attributes of most inverters, which are not able to provide reactive power outside of the feed-in periods. Inverters with called "Q at night" option are not considered in this paper. On the other hand, the smart-inverters in this paper are enabled with a reactive power characteristic that includes the voltage dependence; the implemented curve is depicted in Fig. 2.

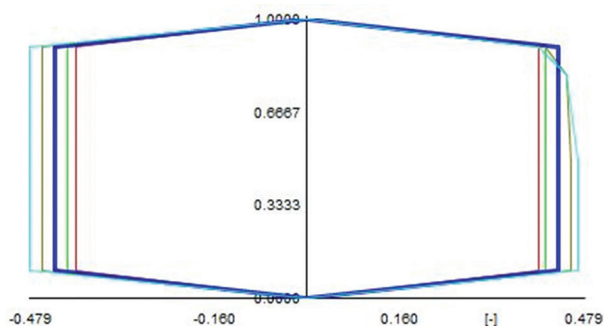


Fig. 2 Example of a reactive curve of a smart inverter used in a PV system, considering voltage dependence.

3. MODELLING AND SIMULATION DESCRIPTION

The performance of voltage control mechanisms in smart-inverters and releasing the synergy between TSO/DSO systems considering the paradigm of tied-micro grids is presented in this paper considering an illustrative case of a TSO-DSO. The main interest is the performance of the voltage control mechanism in the quasi-dynamic voltage profile of the regional TSO-DO power networks in the South-Eastern part of Norway. The equivalent TSO consists of a detailed high-level representation of the regional 132-kV system, Telemark and Vestfold area [11], [30]. The DSO network is created [11] in order to represent the main feature of the 11 kV distribution system. This section is dedicated to modelling aspects of the TSO-DSO. More details on the TSO-DSO system can be found at [11], [31].

Transmission System Operator (TSO)

A detailed high-level model of the regional TSO network of the south-eastern area of Norway, specifically Vestfold and Telemark, is used in this paper. Using information publicly available, the network model has been created. The single line diagram of the TSO model of the Vestfold and Telemark area in Norway is depicted in Fig. 3 [10]; the network model includes seven synchronous generators (SGs) representative of the regional hydropower plants locally available in the Vestfold and Telemark area. The authors have included the connections to the National transmission system in Norway as a simplified equivalent model at 300 and 420 kV levels.

Distribution System Operator (DSO)

The authors have created a representative substation of the local DSO at the region of Telemark and Vestfold; it is used for performance analysis in this paper and can be extended and generalised. The distribution substation is modelled considering a classical step-down transformer (110/11 kV) and a typical 11 kV distribution feeder (representative of the south-eastern part of Norway), as this voltage level is the most widely used voltage level in the Telemark area, Norway.

Underground cables mostly dominate the Norwegian distribution networks in urban areas, and it is usually built like a meshed network. The distribution net-

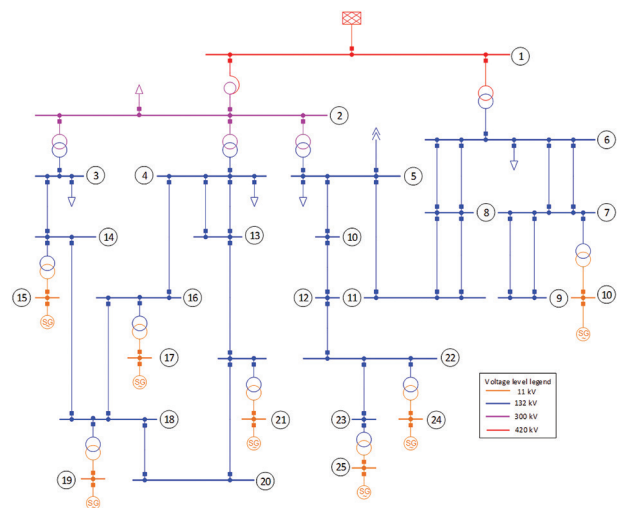


Fig. 3. Single line diagram of the TSO system implemented in this paper: It is a representative of the regional transmission system of Vestfold and Telemark at 132, 300 and 420 kV [11].

works in Norway are built in a meshed configuration, but it is operated as a radial configuration to make it easier to control and predict the different currents and voltages in the grid. Consequently, the authors decided to consider the representative Norwegian distribution feeder as a radial topology, as shown in Fig. 4; however, the feeders are equipped and designed so that it will be possible to work in a ring topology (no considered in this paper). For simplicity, the distribution grid consists of fourteen feeders, three feeders have been modelled in full detail, and the remaining eleven feeders are presented as an equivalent lumped system.

The proposed DSO network has been enhanced with the integration of smart inverters, making the DSO network an active distribution network. Consequently, the DSO system has been intentionally selected to resemble a specific part of the city of Skien in the Telemark area, Norway. The local company Skagerak Nett provides the electricity service as the city of Skien, and the company owns and operates a solar-powered microgrid (solar rooftop panels 800 kW), including a battery energy storage system (BESS, 800kW/1000 kWh). The micro-grid is called Skagerak Energilab, it is supposed to be dedicated to research and development activities, and it is located at the Skagerak Arena, with a potential peak-load of 1,000 kW during football matches. The model used to emulate the performance of the Skagerak Energilab has been created by the authors using information publicly available; the Energilab is equipped with smart-inverters where the voltage control and reactive power production are enabled, and the model is integrated at bus 4 of the feeder 3 to at Fig. 4.

Load and generation profiles

The distribution substation used to emulate the DSO system at node 5 has a 30 MVA capacity; the load has equally divided between 14 feeders. A nominal load

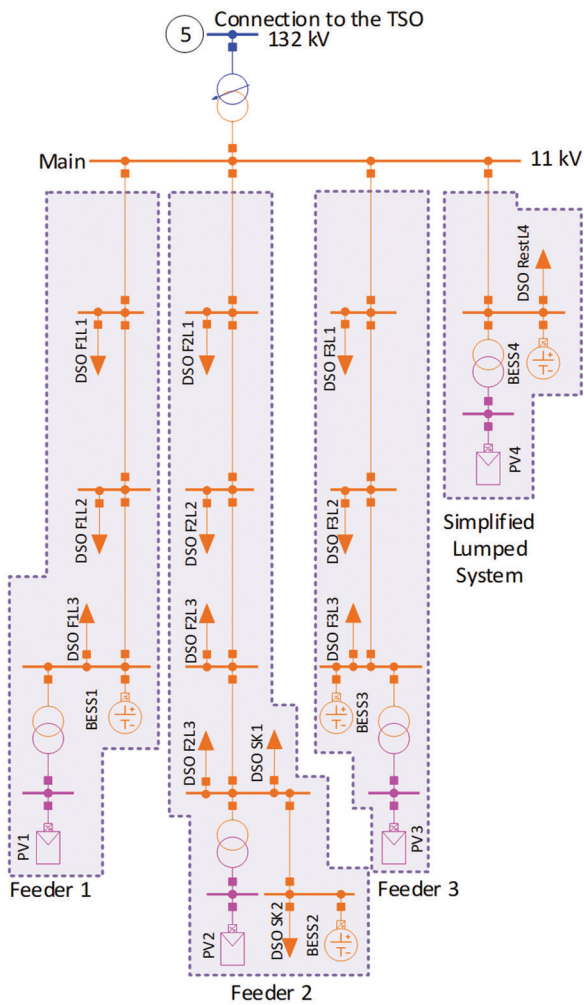


Fig. 4. Single line diagram of the DSO system implemented in this paper: Representative substation at Vestfold Telemark, considering four radial feeders and PV and BESS are depicted for future simulation scenarios [11].

demand of 2 MW is used at each one of the feeders. This way, Feeder 4, which represents simplified 11 feeders, has a peak load of 22 MW.

The total load of the DSO system is considered a residential load except for the case of the Skagerak Energilab, which is considered a special load. Load profiles representative of the 24-hour operation of the loads is synthetically created [32], [33] by using the tool developed by the Centre for Renewable Energy Systems Technology (CREST) at Loughborough University in the United Kingdom.

The CREST model was modified [11] to represent the Norwegian consumer's weather and load. The CREST model was originally created based on stochastic models of British or Indian power consumers. The CREST model was improved and enhanced to consider realistic location in Norway by using the temperatures in Skien, Norway. Also, the original CREST model considers gas as the primary source of heating inside the dwelling, as that is the primary energy source for heating in Great Britain. Therefore, the CREST model is modified to represent

the reality of primary resource use for heating in Norway, mainly done by electricity. Fig. 5 shows the 24-hour load profile (1 sample per minute) of loads 1, 2 and 3 connected at the feeders 1 to 3.

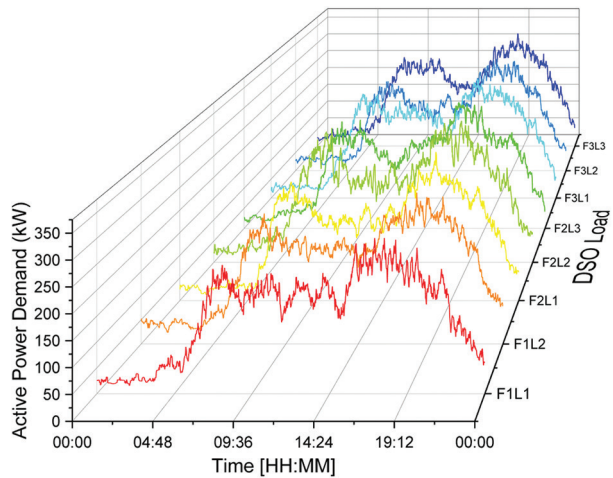


Fig. 5. Hourly power demand (in kW) several loads of the DSO.

Identical electrical consumption patterns in two dwellings have an extremely low probability; consequently, it is required to calculate several consumption profiles for several dwellings to the extent that it is possible to reach the wanted peak load for the different loads in the DigSILENT PowerFactory quasi-dynamic model. Therefore, the load simulations will be performed individually for all the various loads in the model so that none of the loads will have an identical pattern or peak load.

The DSO Feeder 4 is a typical distribution feeder considering a total combined demand of 22 MW, considering residential loads, and using the modified CREST model, the synthetic data of a local residential area with least 6.300 dwellings was created for a load profile of 24-hour (1-minute resolution), and the profile is shown in Fig. 6.

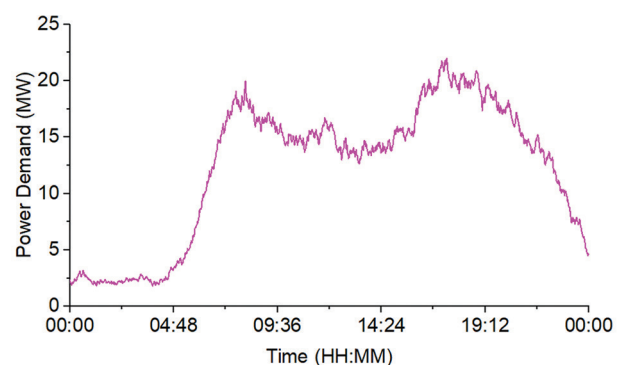


Fig. 6. Hourly load profile for the 22 MW load (1 sample per minute).

To extend the time scale, the diversity of the loads was accordingly modified considering the power demand in the whole system during the year; the authors added additional profiles parameters considering standardised

load profiles. The adjusted profiles include characteristics patterns considering different seasons, working days, and weekends. It allowed producing synthetic data for a whole year loads based on the 24-h profile created by the modified CREST model. By assigning three different profiles to 12 different loads produced a more realistic total load profile avoiding unrealistic simultaneous load peaks. Based on that, the load profile presented in Fig. 5 can be observed as DSO_F1L1 load in summer days (Friday-Sunday) on Fig. 7, which has different peaks and is slightly reduced compared to winter where loads are maximum.

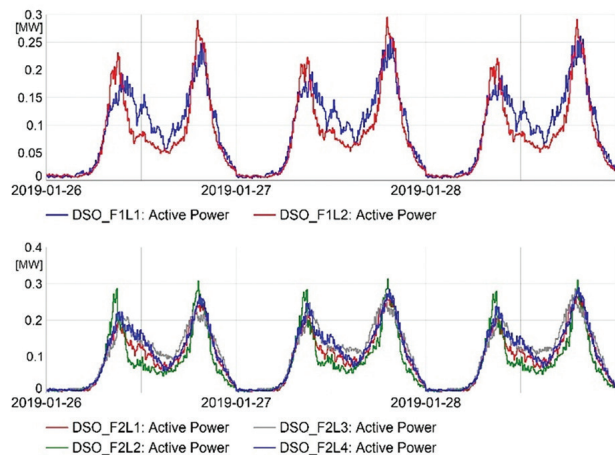


Fig. 7. The implementation of time characteristics for DSO loads.

For TSO loads, time characteristics were implemented the same way as for DSO but based on peak power instead of the day-hourly profile, as it was shown in Fig. 8.

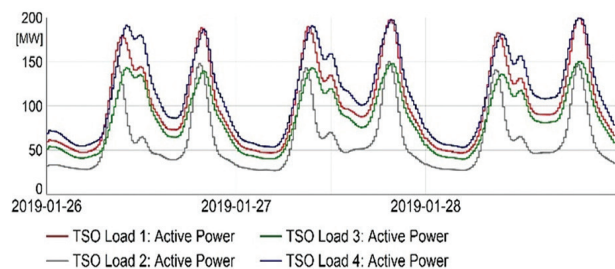


Fig. 8. The implementation of time characteristics for DSO loads

Special Load: Skagerak Arena

The Feeder 2 includes the correction of the Skagerak Arena, which is a stadium dedicated to the local football team [34], [35]. It is collected from publicly available data that the Skagerak Arena have a potential peak-load of 1,000 kW during football matches. The total power demand is divided between two distribution transformers; one transformer supplies around 300 kW (for daily consumption), and the second one is 700 kW (Mainly for the floodlights during football matches). Therefore, the remaining load of this feeder will be around 1.000 kW, which will be divided between three loads of a little over 300 kW.

The implementation of time characteristics applied for general DSO loads is not applicable for Skagerak Arena since matches and events obviously do not occur here every day. Therefore, the authors created and implemented characteristics based only on weekdays. The weekly pattern for Arena is as follows: on Sundays, the Arena is fully loaded with a peak-load of 700 kW; on Saturdays, it is partly loaded for pre-match events with 10% scaling, and on other days it consumes only 1% of load demands. The implementation of discrete-time characteristics for Arena (DSO_SK1 and DSO_SK2) is presented in Fig. 9.

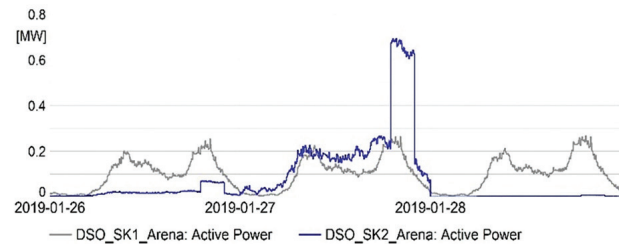


Fig. 9. The implementation of time characteristics for Skagerak Arena loads.

Modelling of BESS

The appropriate control of a BESS provides the possibility of injecting/absorbing active/reactive power, thus providing support to the TSO-DSO interactions. In this scientific paper, the authors have taken advantage of the quasi-dynamic simulation language (QDSL) to create a simplified model of a BESS inside the power system simulation environment. The BESS model aims to simulate the operation of the set, battery, voltage control, and charge control based on the feedback of signals taken from the network operation. The BESS model has been enabled with a simple state of charge (SOC) controller; it controls the active power injection/consumption to keep the battery between the operational limits (SOC_{min} , SOC_{max}). The battery has been modelled considering a simple equivalent circuit model considering the number of individual cells (series and parallel) in the pack and where the SOC is calculated based on the changes of the energy absorbed/produced based on the rate of charging/discharging current.

Performance Indicators

The following data for analysis were obtained during simulations, such as power flow, maximum generation and loads, line loading, and voltage fluctuations. However, for the evaluation of each control mode, we decided to select criteria as follows:

- Total energy loss (MWh) in the DSO and TSO networks.
- Voltage improvement (Voltage difference, min and max values).
- Reactive power flow via DSO/TSO (considered for year scenarios).

- The total active and reactive power production of the distributed energy resources.

Such indicators are general measurements or values that have a relevant impact on a specific study case. In the case of efficiency and Volt-var control, the indicators used to assess the performance of the TSO-DSO system are shown in the following subsections.

Energy loss (E_{loss})

Energy loss has a financial impact on the total operating cost. As a consequence, in this paper, the total energy loss (MWh) in one day is used as an index to assess the quasi-dynamic performance of electricity TSO-DSO interactions. The total energy loss (E_{loss}) is calculated by using the following formula [36]:

$$E_{loss} \left[\frac{MWh}{day} \right] = \int_{t=00:00}^{t=24:00} P_{loss}(t) dt \quad (2)$$

Therefore, the afore presented equation is discretised over a 24-hour:

$$E_{loss} \left[\frac{MWh}{day} \right] = \frac{1}{60} \left[\frac{h}{min} \right] \sum_{t=0}^{\min} P_{loss,t} \quad (3)$$

Voltage Difference (VD)

The index maximum *voltage difference* (VD_{max}) is used in this paper to relate the lowest voltage level (U_{low}) and the highest voltage level (U_{high}) during a period of 24-hours. The voltage difference (VD) of these is compared to the no-load voltage ($V_{no-load}$); therefore, the VD is expressed in percentage (%) is defined as:

$$VD [\%] = \frac{VD_{max} [V]}{U_{no-load} [V]} \times 100\% \quad (4)$$

$$VD_{max} [V] = U_{high} [V] - U_{low} [V] \quad (5)$$

Reactive power flow via TSO/DSO boundary

Reactive power flow has been disregarded for many years in electrical power systems because electricity networks are designed to transmit active power, as that is the energy source billed by the utilities. On the other hand, voltage variability and control has been perceived as a local problem that typically is solved by a local source of reactive power or voltage control. However, the proliferation of smart-inverters in the distribution network has changed the old paradigm, and local reactive power control has to help improve the whole system's performance. Up to now, no reactive power market is enforced commercially around the world, but time-based marked defined prices would be a game-changer for the customers regarding the location of reactive power production. In this paper, the reactive power flows between the DSO and TSO are quantified

by measurements devices at the interface between the systems (Q_{ij}).

Annual Energy production (E_{PDG})

A customer centred market might motivate the owner of the distributed resources located at the demand side to participate in the energy trade on that market; as a consequence, the annual energy production arises an important indicator at the distributed resource assets installed at the DSO. The annual energy production of distributed resources installed in the DSO, e.g., BESS and PV, are calculated (E_{DER}) are calculated. It helps to make evident the performance of the controller assesses at the time to show the operation patterns of the distributed energy resources. The annual energy production is calculated in the separated fashion of the active (E_{PDER}) and reactive power and calculated as:

$$E_{PDER} \left[\frac{MWh}{year} \right] = \int_{t=0}^{t=8760} P_{DER}(t) dt \quad (6)$$

$$E_{QDER} \left[\frac{Mvar h}{year} \right] = \int_{t=0}^{t=8760} Q_{DER}(t) dt \quad (7)$$

where $P_{DER}(t)$ and $Q_{DER}(t)$ are the instantaneous active and reactive power production, respectively.

Simulation Scenarios

The performance assessment of TSO-DSO interactions in Vestfold and Telemark considering the Volt-Var control at smart-inverters in the case of is assessed in two main general scenarios:

- **Short-term variations (ST):** the main performance indicators are assessed over a short-term period, 24-h profile. This assessment is specifically designed to observe and identify intra-hour patterns of variations.
- **Long-term variations (LT):** A long term horizon of simulation is used to analyse extra-day patterns. Mainly, a 365-day period is used in this scenario.

The following subsections are specifically designed to present simulation results and discuss in detail the main findings.

4. SHORT-TERM (S.T) PERFORMANCE ASSESSMENT

Scenario ST.I: Base

The base scenario is used to assess the performance of the TSO/DSO system, considering a typical traditional system where there is no integration of low carbon technologies at the distribution network. This scenario is called the base and used as a reference for comparison with other scenarios. Table 1 shows a summary of the energy losses share between TSO and DSO during the 24-hour and the voltage difference indicator. A plot of 24-hour active power losses at the TSO/DSO is pre-

sented in Fig. 6; it is essential to notice that the maximum losses at the DSO system are related to times of the peak demand (08:00 and 17:30, see Fig. 10).

Table 1. Energy losses and voltage differences: Scenario ST.I

System	Energy losses E_{loss} [MWh/day]	Voltage difference UD [%]
TSO-grid	194.81	2.17
DSO-grid	1.820	1.88



Fig. 10. Plot of the active power losses (MW) at the TSO/DSO systems during a period of 24-hours.

Scenario ST.II: Integration of Top Roof PV

This scenario, the TSO/DSO network is as described in Scenario I, but now it considers the integration of PV systems at the residential level, the so-called top roof PV system populated at the demand side. The top roof PV system consists of several PV panels located at the property's roof and a smart inverter installed inside the property. This scenario does not consider the use of energy storage; consequently, the PV locally produce electricity during sunlight hours, and then the customer must buy electricity during off-daylight hours.

In this paper, the top roof PV model was set up to duplicate the conditions at the location named Falkum, in the city of Skien, south-eastern part of Norway (precisely, 59.2° latitude, 9.6° longitude). The PV system considers 160W/35V solar panels, considering single crystalline silicon. This scenario is designed to consider a complete integration of the PV system in the DSO network. Ideally, the total installed capacity of the top roof PV system is adjusted to be above the peak of the local demand; Table 2 depicts a summary of the DSO performance integrating top roof PV at each one of the feeders and the total DSO grid.

The smart-inverters allows the top roof PV system to fed reactive power (when operates as over-excited), and absorbing reactive power (when operates as under-excited) allows the smart-inverter to control the voltage by changes of reactive power. This scenario considers a full DSO operating the distribution network; as a consequence, the DSO authorises the active participation of the smart-inverter in voltage regulation. This paper considers six different voltage control methods, and their specific details are presented in Table 3.

Table 2. Summary of the Integration of PV systems in the DSO System.

Feeder	Total installed Power [kWp]	Number of panels	Penetration level [%]
1	2,000	12,500	100.6
2	840	5,250	45.4
3	2,000	12,500	105.5
4	22,000	137,500	110.5
Total DSO-grid	26,840	167,750	104.6

Table 3. Details of voltage control implemented at the smart-inverters: Scenario ST.II.

Case	Description
1	Constant power factor, $pf = 1.0$ (no reactive power support)
2	Constant power factor, $pf = 0.95$
3	Constant power factor, $pf = 0.90$
4	Slow voltage droop: $Q(U) - 30\%$ Droop set to $K_U = 30\%$, $U_{set} = 1.0$ pu
5	Fast voltage droop: $Q(U) = 10\%$ Droop set to $K_U = 10\%$, $U_{set} = 1.0$ pu
6	Constant voltage set-point at $U_{set} = 1.0$ pu

Two important considerations are taken into account when operating the smart-inverters: (i) the inverters deliver all the active power produced by the PV systems at the time, (ii) the inverters are equipped with voltage control that enables the reactive power injection/absorption. Fig. 11 depicts an outline of the numerical results of total energy losses [MWh/day]. It is clear from the figures that the smart-inverter operating in voltage support control mode provides a reduction in the total power losses and produces a positive change in the voltage profile of the whole TSO-DSO system.

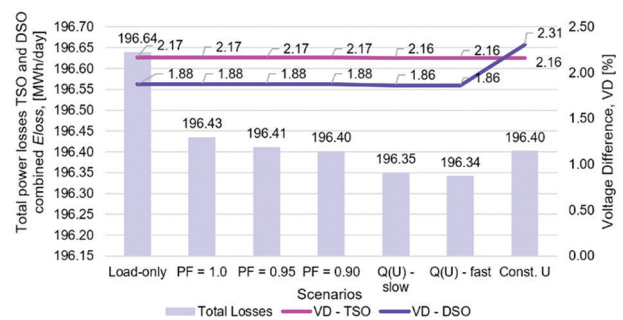


Fig. 11. Summary results of different voltage control implemented at the smart-inverters: Scenario ST.II.

The numerical results of the quasi-dynamic simulation over a 24-hour period show that the most significant and most minor total energy loss (E_{loss}) are found when the voltage controller is adjusted to the fast droop settings (Case 5, see Table 3) and power factor equal to 1.0 (Case 1, see Table 3), respectively.

The energy-saving of TSO and DSO is calculated referred to the Scenario ST.I (load-only) results are shown in Table 4. One essential element here is the most considerable energy reduction of TSO using Case 6. Meanwhile, the most significant energy reduction of DSO occurs using Case 4. The maximum TSO/DSO saving occurs at Case 5 ($Q(U)$ fast), but the savings at this situation the energy saving is not maximum at each system.

Table 4. Energy savings of cases comparison based to Scenario ST.I (load-only): Scenario ST.II.

Scenario ST.II Case	Energy-saving TSO [MWh/day]	Energy-saving DSO [MWh/day]	Energy-saving Total [MWh/day]
1	57.1	147.1	204.2
2	73.4	154.7	228.0
3	80.8	157.0	237.9
4	131.4	157.8	289.1
5	171.0	126.0	297.0
6	220.0	17.0	237.0

Scenario ST.III: Integration of PV and BESS

In this paper, the previous analysis is taken as a reference to define simulation scenarios considering the integration of BESSs into the DSO. In this specific case, the two extreme cases of the Scenario ST.II (PV-voltage controllers) are selected as the baseline of the cases considering the integration of BESS in the DSO network; Table 5 is used to summarise the set of simulation cases considered in this paper.

Table 5. Details of voltage control implemented at the smart-inverters: Scenario ST.III.

PV-system controller scenario	Case	BESS controller scenario
Scenario ST.III.A Lowest losses: $Q(U)$, $K_U = 10\%$ Scenario II, Case 5	1	Power factor, $pf = 1.0$
	2	Power factor, $pf = 0.9$
	3	Slow voltage droop: $Q(U) = 30\%$ Droop set to $K_U = 30\%$, $U_{set} = 1.0$ pu
	4	Fast voltage droop: $Q(U) = 10\%$ Droop set to $K_U = 10\%$, $U_{set} = 1.0$ pu
	5	Constant voltage setpoint
Scenario ST.III.B Highest losses $pf = 1.0$ Scenario II, Case 1	1	Constant power factor, $pf = 1.0$
	2	Constant power factor, $pf = 0.9$
	3	Slow voltage droop: $Q(U) = 30\%$ Droop set to $K_U = 30\%$, $U_{set} = 1.0$ pu
	4	Fast voltage droop: $Q(U) = 10\%$ Droop set to $K_U = 10\%$, $U_{set} = 1.0$ pu
	5	Constant voltage setpoint

Scenario ST.III.A: Lowest PV-losses scenarios

This scenario is created to assess the performance of the PV smart-inverters enabled with controllers set to $Q(V)$ operating mode and $K_U = 10\%$; consequently, the lowest losses caused by the PV integration are considered. Five different cases are considered in the assessment regarding the voltage control at the smart-inverter in-

stalled at the BESSs. Fig. 12 depicts the performance of the energy losses (E_{loss}) and voltage differences (VD in percentage) during a 24-hour period. It is observed from the numerical results that the combined minimum energy losses are found when the $Q(U)$ -fast control is enabled in the smart inverters (Case 6).

Scenario ST.III.B: Highest PV-losses scenarios

This scenario is designed to assess the performance of the highest losses caused by the PV system when the smart inverters are enabled with a voltage controller that follows a constant power factor of 1.0; the BESS is alternatively assessed considering five cases of voltage control at the smart-inverter. Fig. 13 shows the numerical results of the energy losses (E_{loss}) and voltage differences (VD) during a period of 24-hours. The lowest combined minimum energy losses are found when the controller of the smart-inverters is operating at constant voltage but tends to produce higher voltage levels at the DSO network.

Summary of Scenario ST.III

Table 6 shows a complete summary of the numerical results of the simulations considering the different scenarios where the controllers are enabled to the smart-inverters. The table has been formatted using a colour-based scale, where the green colour represents the most beneficial result for an indicator and the red colours the least beneficial.

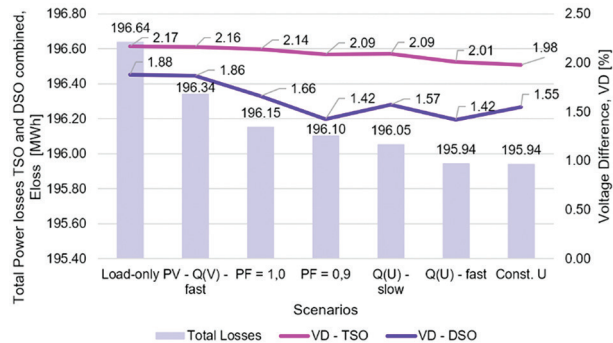


Fig. 12. Summary results of different voltage control implemented at the smart-inverters: Scenario ST. III.A.

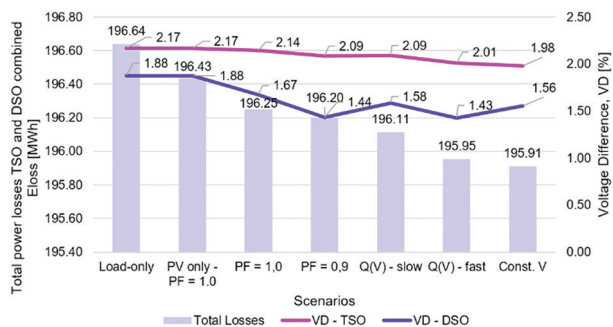


Fig. 13. Summary results of different voltage control implemented at the smart-inverters: Scenario ST.III.B.

The summary presented in Table 6 allows concluding that for the DSO-TSO case shown in this paper, an excellent performance with respect to both energy losses and voltage difference in the DSO-grid is reached when the smart-inverter at the PV system operating at unity power factor and the voltage controller of the BESS inverter set to $Q(U)$, $K_u = 10\%$.

Furthermore, those scenarios show a lower-than-average voltage difference and energy losses in the TSO-grid, as a consequence, it making it one of the most efficient scenarios concerning total energy loss.

5. LONG-TERM (L.T) PERFORMANCE ASSESSMENT

A comparison of the initial 24-hour performance of the TSO-DSO model considering the implementation of BESS and installation of top roof PV modules was described in [11]. The examination period was based on the whole 24-hour period. In this paper, the performance assessment extends the simulation period up to an entire year (365-day). The following subsections are dedicated to assessing the performance of the TSO-DSO interactions, including several operational scenarios for the investigated grid. Few of them are enhanced from [11] to include long-term variation over a period of a year.

Table 6. Summary of the simulation results with BESS scenarios.

	PV - Setting	BESS - Setting	VD - DSO	VD - TSO	DSO E _{loss} [MWh/day]	TSO E _{loss} [MWh/day]	Total E _{loss} [MWh/day]
Scenario ST.III.A	1		1.67	2.14	1.52	194.73	196.08
	2		1.44	2.09	1.50	194.70	196.20
	3		1.58	2.09	1.47	194.64	196.11
	4		1.43	2.01	1.47	194.48	195.95
	5		1.56	1.98	1.54	194.37	195.75
Scenario ST.III.B	1		1.66	2.14	1.52	194.63	195.99
	2		1.42	2.09	1.50	194.60	196.10
	2		1.57	2.09	1.51	194.54	196.05
	4		1.42	2.01	1.54	194.40	195.94
	5		1.55	1.98	1.65	194.29	195.84

Scenario LT.I: Base

The first simulation scenario represents TSO-DSO network, considering there is not the integration of smart-inverters at the distributed energy resources, PV and BESS; this scenario replicated the short-term scenario ST-I but considers a long term simulation horizon (1-year).

Scenario LT.II: Unity power factor

The smart-inverters installed at the DSO are controlled using constant reactive power operating mode where the reactive power is controlled to maintain a unity power factor at the time that reduces peaks, load flow and cable loading; as a consequence, the top roof PV system and the and BESS are operating in such way. Fig. 14 illustrated the case of node 3, Feeder 3.

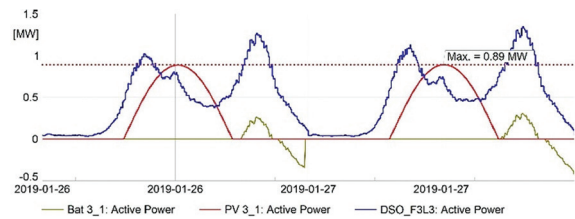


Fig. 14. Illustrative example of active power flow at the distribution line and the BESS active power production showing the peak shaving operation (highlighted in red colour).

It is easy to see the peak shaving capability of the enabled controller at the BESS. The black line at the figure depicts the actual power, and the blue line is dedicated to the performance without BESS. In other words, instead of loading the distribution line and transferring more than 1 MW, the controller enabled BESS to generate around 200 kW to supply load DSO_F3L3. Fig. 15 represents the operation of PV BESS system at feeder 3, and the profile of load DSO_F3L3, which is connected to the same node.

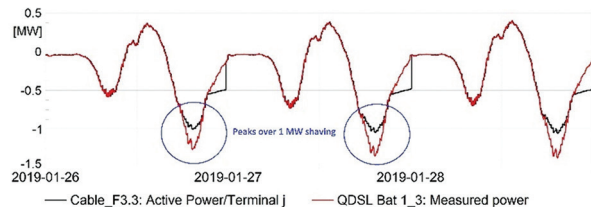


Fig. 15. Illustrative example of operation of distributed energy assets (BESS-PV) connected at the feeder F3 in Scenario LT.II

Scenario LT.III: mixed control strategies

Results of the 24-hour simulation showed that the smart-inverter at the PV system operating $pf = 1.0$ and the voltage controller of the BESS inverter set to $Q(U)$, $K_u = 10\%$ has excellent performance with respect to both energy losses and voltage difference in the DSO-grid. Fig 16 shows the simulation results of the operation of PV-BESS pair considering the unity power factor ($Q = 0$) and $Q(U)$ control, $K_u = 10\%$. In this case, the top roof PV system keeps reactive power as zero (as expected by the operation mode, $const Q = 0$), BESS injects reactive power according to the voltage measurements and $Q(U)$ settings.

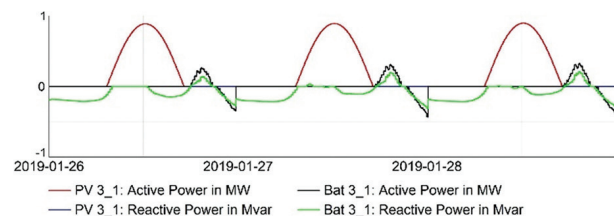


Fig. 16. Illustrative example of the operation of BESS-PV system at the DSO feeder F3 in Scenario LT.III

Scenario LT.IV: Wide area voltage control

This operation scenario is characterised by the implementation of a wide area voltage control with the main

objective of monitoring and controlling the interactions at the TSO/DSO boundary. In this case, the voltage controller is designed to keep the steady-state voltage at PCC at a predefined setpoint ($|U_{set}| = 1.00$ pu), the action control is taken in the relative power injection/consumption of the BESS as follow: if the voltage is below the setpoint, PV and BESS system inject reactive power and opposite: when is overvoltage. Fig 17 shows the performance of the wide-area voltage controller over a period of three days, and there is a clear correlation between the voltage and reactive power as defined by the controllers. It is possible to see that during periods where the voltage drops below the setpoint ($|U_{set}| = 1.00$ pu in this case), either PV or BESS are injecting reactive power. Usually, during daylight, reactive power is provided by PV; during the night by BESS. Results were obtained with the setting of 100 MVar per pu (1 MVar for 1.0% droop).

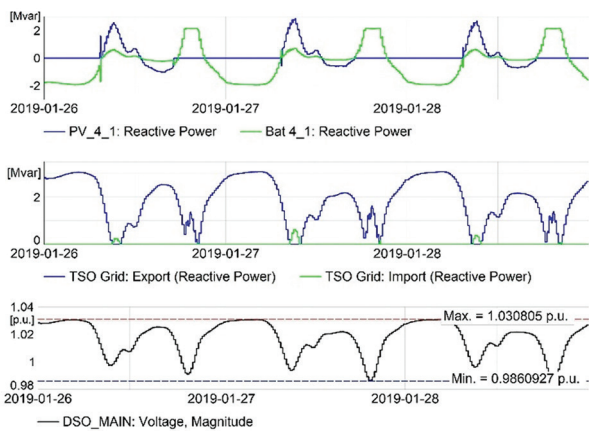


Fig. 17. The operation of BESS-PV system at the feeder F4 in Scenario LT.IV

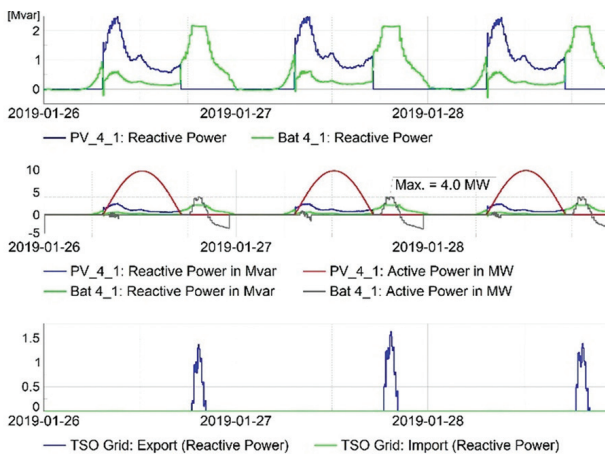


Fig. 18. Illustrative example of the operation of BESS-PV system at the feeder F4 in Scenario LT.V

Scenario LT.V: Wide area reactive power control

In this scenario, smart-inverters of PV and BESS aimed to keep reactive power flow via TSO/DSO boundary as zero ($Q = 0$ pu). From Fig. 18, it can see that most of the time, it is possible to achieve. However, the observed peaks of reactive power interchange can be explained that PV inverters cannot inject reactive power when there is no active

power output. The BESS inverters cannot inject reactive power when SOC is low and requirements (settings) for reactive power injection are not fulfilled.

Results of Scenario LT.III

For each one of the long term (LT) operational scenario one-year simulations were made with the recording results for PV, BESS systems, DSO and TSO separately with the aim to obtain values of annual energy production and losses, active and reactive power flow via TSO/DSO boundaries maximum and minimum values for voltage. The most significant results are illustrated in Fig. 19 – Fig. 21.

Fig. 19 shows the reactive power production/consumption of the distributed energy resources, e.g., PV and BESS, during a period of one year, and the same figure shows the instantaneous active power losses (P_{loss} MW) and energy loss in the DSO network (E_{loss}).

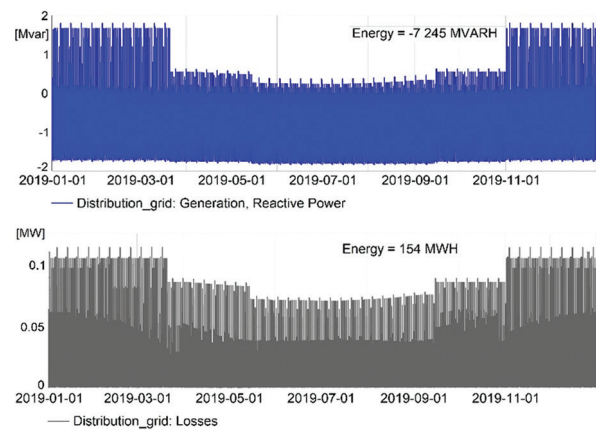


Fig.19. Illustrative example of the operation of DSO in the case of Scenario LT.III.

Fig. 20 shows the performance of voltage profile as measured at the boundary between the TSO-DSO networks (also known as PCC) and the minimum and maximum values during one year. The bottom part of Fig 21 shows the performance of the reactive power flow at TSO/DSO boundary discriminating the import/exports conditions created by the reactive power management control system (station controller).

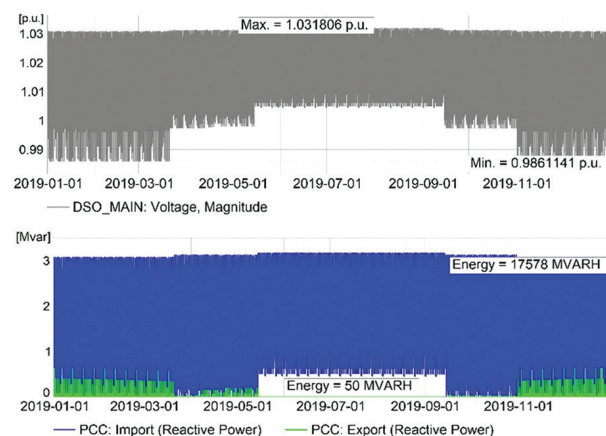


Fig. 20. Results for DSO in Scenario LT.IV (remote const U).

Fig 21 shows the performance of the reactive power flow via TSO/DSO boundary where the power flow is reduced by the control actions taken by the controller at the time the figure depicts the performance of the PCC steady-state voltage, indicating how voltage profile is changed in such operational scenario.

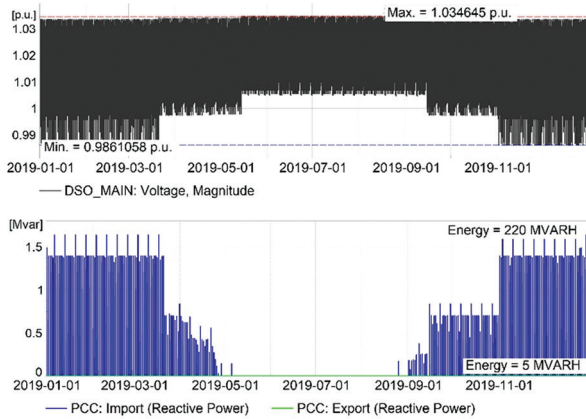


Fig. 21. Results at TSO/DSO boundary in case of Scenario LT.V

A summary of the main indicator used to assess the long term performance of the operating scenarios is shown in Table 7. The summary provided a clear comparison between operational scenarios taking into account indicators mentioned in section 4.

Using the scenario LT.I, as a reference, the integration of the distributed energy resources (PV and BESS) -LT.II- provided a smooth voltage profile and reduction in extreme voltages when the TSO-DSO losses are reduced. The ST.III with the implementation of settings taken from LT.III, system performance increased: voltage fluctuations and losses reduced when compared to ST.II.

The scenario LT.IV aims to control voltage at the controlled node. As a consequence, there is an apparent reduction in voltage fluctuations. However, since the voltage control is performed via reactive power injection/consumption, there is an increased reactive power flow via PCC, which might lead to additional costs for DSO (if a reactive power compensation market is enabled, however, that discussion is beyond this paper. Finally, the scenario LT.V shows a significantly reduced reactive power flow via PCC, which is a very positive consequence, as there is a capacity released at the distribution network providing a positive impact for the DSO, but in turn, this operation mode raises voltage fluctuations when compared to LT.IV. However, the voltage fluctuations are comparable to LT.II and less than in the case of LT.I.

Table 7. Summary of the simulation results with BESS of the long term operational scenarios.

OS	Short description	PCC Umax [p.u.]	PCC Umin [p.u.]	VD [%]	P DSO Import [MWh]	P DSO Export [MWh]	Q DSO Import [MVARh]	Q DSO Export [MVARh]	TSO Losses [MWh]	DSO Losses [MWh]
I	Initial	1.035042	0.9818979	5.31	64 395	-	10 252	740	87 230	209
II	PV+BESS const Q=0	1.035042	0.983184	5.19	38 683	13 366	10 242	717	87 219	149
III	Paper [AV8]	1.033343	0.9843438	4.90	38 686	13 364	17 131	-	87 231	154
IV	Station const U	1.031806	0.9861141	4.57	38 688	13 365	17 578	50	87 217	156
V	Station const Q	1.034645	0.9861058	4.85	38 729	13 344	220	5	87 184	143

6. CONCLUSIONS

Power electronic converters (PECs) have the potential to provide a wide variety of services when well-designed controllers and appropriate settings are used. The IEEE std.

1457-2018 provide the basis to enable the PECs with more active voltage control. Furthermore, several places worldwide are developing customer-centred legislation and markets; consequently, the smart inverters empower the DSO by creating positive TSO/DSO interactions. This research paper presents a comprehensive assessment of the steady-state performance of the DSO-TSO interaction caused by several voltage control strategies in smart-inverters

installed at the DSO network. The assessment considers two different time scales: short term (24-hours, 1-minute resolution) and long-term (one-year) horizon. The three leading indicators are used in the assessment: total energy losses voltage profile in the TSO-DSO system and the power flow interaction at the interface between the systems. The assessment is based on numerical results using the DIgSILENT PowerFactory simulation tool, where the voltage controllers have been implemented, and regional electrical system in south-eastern Norway, the area of Vestfold and Telemark as been used for illustrative purposes. Overall results indicate that voltage profiles are improved when the smart converters work at constant voltage, and operation to constant reactive power provides a better reduction in total energy losses.

7. REFERENCES

- [1] Thomas Krechel; F. Sanchez; F. Gonzalez-Longatt; H. Chamorro; Jose Luis Rueda, "Transmission System Friendly Micro-grids: An option to provide Ancillary Services", *Distributed Energy Resources in Microgrids*, Elsevier, 2018.
- [2] P. Meraz et al., "Renewable Energy and Economic Dispatch Integration Within the Honduras Electricity Market", Springer, Singapore, 2021, pp. 1–34.
- [3] F. S. Gorostiza, F. Gonzalez-Longatt, "Deep Reinforcement Learning-Based Controller for SOC Management of Multi-Electrical Energy Storage System", *IEEE Transactions on Smart Grid*, Vol. 3053, No. C, 2020, pp. 1–1.
- [4] W. Cui, B. Zhang, "Lyapunov-Regularized Reinforcement Learning for Power System Transient Stability", *IEEE Control Systems Letters*, Vol. 6, 2022, pp. 974-979.
- [5] IEEE PES Industry Technical Support Task Force, "Impact of IEEE 1547 Standard on Smart Inverters", 2018.
- [6] D. Chathurangi, U. Jayatunga, S. Perera, A.P. Agalgaonkar; T. Siyambalapatiya, "Comparative evaluation of solar PV hosting capacity enhancement using Volt-VAr and Volt-Watt control strategies", *Renewable Energy*, Vol. 177, 2021, pp. 1063-1075.
- [7] A. Perilla, J. L. Rueda Torres, S. Papadakis, E. Rakhshani, M. van der Meijden, F. Gonzalez-Longatt, "Power-Angle Modulation Controller to Support Transient Stability of Power Systems Dominated by Power Electronic Interfaced Wind Generation", *Energies*, Vol. 13, No. 12, 2020, p. 3178.
- [8] P. Betancourt-Paulino, H. R. Chamorro, M. Soleimani, F. Gonzalez-Longatt, V. K. Sood, W. Martinez, "On the perspective of grid architecture model with high TSO-DSO interaction", *IET Energy Systems Integration*, Vol. 2021, 2020, pp. 1–12.
- [9] T. Krechel, F. Sanchez, F. Gonzalez-Longatt, H. Chamorro, J. L. Rueda, "Transmission system-friendly microgrids: an option to provide ancillary services", *Distributed Energy Resources in Microgrids*, 2019, pp. 291–321.
- [10] E. Rakhshani, A. Perilla, J. R. Torres, F. G. Longatt, T. B. Soeiro, M. Van Der Meijden, "FAPI Controller for Frequency Support in Low-Inertia Power Systems", *IEEE Open Access Journal of Power and Energy*, Vol. 7, 2020, pp. 276-286.
- [11] D. Pettersen, E. Melfald, A. Chowdhury, M. N. Acosta, F. Gonzalez-Longatt, D. Topic, "TSO – DSO Performance Considering Volt-Var Control at Smart-Inverters: Case of Vestfold and Telemark in Norway", 2020.
- [12] A. Hirsch, Y. Parag, J. Guerrero, "Microgrids: A review of technologies, key drivers, and outstanding issues", *Renewable and Sustainable Energy Reviews*, Vol. 90, 2018, pp. 402–411.
- [13] A. Peña Asensio, F. Gonzalez-Longatt, S. Arnaltes, J. L. Rodríguez-Amenedo, "Analysis of the Converter Synchronizing Method for the Contribution of Battery Energy Storage Systems to Inertia Emulation", *Energies*, Vol. 13, No. 6, 2020, p. 1478.
- [14] F. Gonzalez-Longatt, J. L. Rueda, "Advanced Smart Grid Functionalities Based on PowerFactory", Springer, United Kingdom, 2018.
- [15] Y. A. I. Mohamed, A. A. Radwan, "Hierarchical Control System for Robust Microgrid Operation and Seamless Mode Transfer in Active Distribution Systems", *IEEE Transactions on Smart Grid*, Vol. 2, No. 2, 2011, pp. 352-362.
- [16] "TSO-DSO interaction: An Overview of current interaction between transmission and distribution system operators and an assessment of their cooperation in Smart Grids", 2014, <https://smart-grids.no/wp-content/uploads/sites/4/2016/01/ISGAN-TSO-DSO-interaction.pdf> (accessed: 2020)
- [17] "Demand Connection Code." https://electricity.network-codes.eu/network_codes/dcc/ (accessed Oct. 13, 2018).
- [18] J. Morin, F. Colas, X. Guillard, J.-Y. Dieulot, S. Grenard, "Joint DSO–TSO reactive power management for an HV system considering MV systems support", *CIGRE - Open Access Proceedings Journal*, Vol. 2017, No. 1, 2017, pp. 1269–1273.
- [19] H. R. Chamorro, I. Riaño, R. Gerndt, I. Zelinka, F. Gonzalez-Longatt, V. K. Sood, "Synthetic inertia control based on fuzzy adaptive differential evolution", *International Journal of Electrical Power & Energy Systems*, Vol. 105, 2019, pp. 803–813.

- [20] P. Regulski, F. Gonzalez-Longatt, V. Terzija, "Estimation of load model parameters from instantaneous voltage and current", Proceedings of the IEEE International Conference on Fuzzy Systems, Taipei, Taiwan, 27-30 June 2011.
- [21] R. Torkzadeh, H. R. Chamorro, R. Rye, M. Eliassi, L. Toma, F. Gonzalez-Longatt, "Reactive Power Control of Grid-Interactive Battery Energy Storage System for WADC", Proceedings of the IEEE PES Innovative Smart Grid Technologies Europe, Bucharest, Romania, 29 September - 2 October 2019.
- [22] D. T. Rizy, Y. Xu, H. Li, F. Li, P. Irminger, "Volt/Var control using inverter-based distributed energy resources", Proceedings of the IEEE Power and Energy Society General Meeting, Detroit, MI, USA, 24-28 July 2011, pp. 1-8.
- [23] F. Gonzalez-Longatt, B. S. Rajpurohit, S. N. Singh, "Optimal structure of a Smart DC micro-grid for a cluster of zero net energy buildings", Proceedings of the IEEE International Energy Conference, Leuven, Belgium, 4-8 April 2016, pp. 1-7.
- [24] S. Mugemanyi, Z. Qu, F. X. Rugema, Y. Dong, C. Bananeza, L. Wang, "Optimal Reactive Power Dispatch Using Chaotic Bat Algorithm", IEEE Access, Vol. 8, 2020, pp. 65830-65867.
- [25] "Power Generating Plants in the Low Voltage Network (VDE-AR-N 4105)." <https://www.vde.com/en/fnn/topics/technical-connection-rules/power-generating-plants> (accessed: 2021).
- [26] Y. Bae, T. Vu, R. Kim, "Implemental Control Strategy for Grid Stabilization of Grid-Connected PV System Based on German Grid Code in Symmetrical Low-to-Medium Voltage Network", in IEEE Transactions on Energy Conversion, Vol. 28, No. 3, pp. 619-631, Sept. 2013.
- [27] V. Astapov, P. H. Divshali, L. Söder, "The potential of distribution grid as an alternative source for reactive power control in transmission grid", Proceedings of the 19th International Scientific Conference on Electric Power Engineering, Brno, Czech Republic, 16-18 May 2018, pp. 1-6.
- [28] M. Tomaszewski, S. Stanković, I. Leisse, L. Söder, "Minimisation of Reactive Power Exchange at the DSO/TSO interface: Öland case", Proceedings of the IEEE PES Innovative Smart Grid Technologies Europe, Bucharest, Romania, 29 September - 2 October 2019, pp. 1-5.
- [29] H. Laaksonen, C. Parthasarathy, H. Khajeh, M. Shafie-Khah, N. Hatziargyriou, "Flexibility Services Provision by Frequency-Dependent Control of On-Load Tap-Changer and Distributed Energy Resources", IEEE Access, Vol. 9, 2021, pp. 45587-45599.
- [30] M. N. Acosta, F. Gonzalez-Longatt, S. Denysiuk, H. Strelkova, "Optimal Settings of Fast Active Power Controller: Nordic Case", Proceedings of the IEEE 7th International Conference on Energy Smart Systems, Kyiv, Ukraine, 12-14 May 2020.
- [31] M. N. Acosta, F. Gonzalez-Longatt, D. Topić, M. A. Andrade, "Optimal Microgrid-Interactive Reactive Power Management for Day-Ahead Operation", Energies, Vol. 14, No. 5, 2021, p. 1275.
- [32] F. Gonzalez-Longatt; F. Sanchez; B. S. Rajpurohit; S. N. Singh, R. K. Chuahan, "On Topology for a Smart DC micro-grid for a Cluster of Zero Net Energy Buildings", Distributed Energy Resources in Microgrids, Elsevier, 2019.
- [33] I. Richardson, M. Thomson, D. Infield, "A high-resolution domestic building occupancy model for energy demand simulations", Energy and Buildings, Vol. 40, No. 8, 2008, pp. 1560-1566.
- [34] A. Sharma, M. Kolhe, S. O. Kristiansen, S. Simonsen, H. Landsverk, S. M. Oland, "Techno-Economic Case Study of Micro-Grid System at Soccer Club of Skagerak Arena Norway", Proceedings of the 2020 5th International Conference on Smart and Sustainable Technologies, Split, Croatia, 23-26 September 2020, pp. 1-5.
- [35] K. Berg, M. Resch, T. Weniger, S. Simonsen, "Economic evaluation of operation strategies for battery systems in football stadiums: A Norwegian case study", Journal of Energy Storage, Volume 34, 2021.
- [36] A. Eid, A. Y. Abdelaziz, M. Dardeer, "Energy Loss Reduction of Distribution Systems Equipped with Multiple Distributed Generations Considering Uncertainty using Manta-Ray Foraging Optimization", International Journal of Renewable Energy Development, Vol. 10, No. 4, 2021, pp. 779-787.

Electric Energy Management for Plug-in Electric Vehicles Charging in the Distribution System by a dual cascade scheduling algorithm

Case Study

Supipat Panichtanakom

Prince of Songkla University,
Faculty of Engineering, Department of Electrical
Engineering
Hatyai, Songkla, Thailand
Kanapacame@hotmail.com

Kusumal Chalermyanont

Prince of Songkla University,
Faculty of Engineering, Department of Electrical
Engineering
Hatyai, Songkla, Thailand
Kusumal.c@psu.ac.th

Abstract – This paper presents an algorithm for plug-in electric vehicles (PEVs) charging in the three-phase distribution system for residential houses. It aims to prevent violent voltage level deviation and increasing losses on the three-phase distribution system due to uncontrolled charging and allocate power to each plug-in electric vehicle. The algorithm is comprised of two processes. The first process is power limitation and limited power of load imbalance by if-else rules, while the second process is power allocation to each PEV by the dual cascade scheduling algorithm which is the integration of tasking scheduling algorithms. A 100 kVA distribution transformer and 30 houses are defined in the simulation situation. Also, the available PEVs in single-phase, two-phase, and three-phase systems are assigned for verification of the proposed algorithm. Root-mean-square deviation (RMSD) referred to the satisfaction of PEV owners, total PEVs charged energy, and the average percentage of achieved charging time, as the result indicators. The results show the proposed algorithm can provide good results without rejected PEVs charging. Furthermore, this paper also displays the analysis of voltage level, percentage of voltage unbalance factor, and loss in the distribution system. In the future, coordination with home appliances to gain a high load margin or electric energy cost control will be improved in the proposed algorithm.

Keywords: Electric energy management, Plug-in electric vehicles charging, Dual cascade scheduling algorithm

1. INTRODUCTION

Nowadays, Plug-in Electric Vehicles (PEVs) are of interest to many countries because they offer a reduction in the volatility of fuel costs due to the operation of global markets and also because of environmental concerns. Moreover, a variety of research studies have proposed novel technologies for PEVs such as energy management for PEVs charging, battery technology, and charging or discharging technology.

The uncontrolled PEVs charging may cause problems in the distribution system, such as voltage level deviation, increased losses in the distribution system [1], and a decrease in transformer lifetime. When many PEVs are plugged into the distribution system at the same time, high electricity consumption occurs, which causes the voltage to drop, especially at the farthest locations on

the transmission line [2], [3]. Moreover, excessive domestic consumption can increase the temperature of transformers, causing deterioration of their insulation and decreasing transformer lifetime [4]–[6].

The electric energy required for PEV charging consists of two variables: power and time. Power management methods are based on controlling the electric energy required by a PEV in a limited time. Fuzzy logic power control algorithms [7] are capable of increasing the charging power when consumption is low and decreasing it when consumption is high. However, rapidly increasing the power level may reduce battery lifetime. Time control methods are used when the power is limited and are suitable for fully charging batteries with no impact on the distribution system. The principle of time control methods is to search for periods of low

consumption and persuade PEV owners to charge during those periods by reducing the price of electricity during those periods [8]. Examples of this method are the *ant colony* algorithm [9], *game theory* [10], [11], *valley filling* [12], [13], *genetic algorithm (GA)* [14], *genetic-intelligent scatter search algorithm (GA-ISS)* [15], home energy management [16]–[21], and priority scheduling [22]–[28]. However, these algorithms mostly aim to get more energy and low cost but do not take into account the impacts of voltage levels and unbalanced voltage levels in the three-phase system according to the standard, which would affect the efficiency of the power distribution system and does not represent the maximum and minimum achieved PEVs charging and PEV owner satisfaction level. Moreover, they are also complex, hard to implement, and have the possibility of causing new peak power. Therefore, this paper presents the algorithm that is a simple method, easy to implement, and operates real-time scheduling.

The scheduling algorithms are based on the requested time and available time to generate a weight for sorting PEVs charging. The scored priority scheduling [23] adopts the fuzzy logic to generate a weight while the real-time scheduling [29] uses a ratio of the requested time and available time and the improved queuing-theory-based scheduling [30] applies available time to sort PEVs. All scheduling algorithms have a single weight for sorting PEVs and intend to provide PEVs charging success which may cause some PEVs to be rejected. Also, algorithms can get confused when sorting PEVs with the same weight.

In this paper, the case study in Thailand was chosen because electric vehicles are gaining interest from the central government, and urgent policy for implementation-defined. However, research on the topic continues to progress slowly because of the lack of statistical information concerning vehicle usage, information on people's needs, and other measures used with PEVs charging. Paper [31] published in the proceeding shows PEVs charging by the load shaving method based on TOU (Time of Use) rates, which is a study of PEVs charging on two rates of electric energy price in two periods. It is unsuitable for PEVs charging to gain high electric energy while keeping electric energy costs low.

In this paper, simple electric energy management for PEVs charging in the three-phase distribution system for the residential houses is proposed. The management process can be divided into two processes. First, the power available is calculated based on the identification of the power margin and the limitation of load unbalance in a three-phase distribution system to control voltage level according to the standard and improve losses in the distribution system. The second process is power allocation using the dual cascade scheduling algorithm. The power and load unbalance are limited by if-else rules, and the charging power of PEVs is allocated by the dual cascade scheduling algorithm based on simple task-scheduling algorithms [32]

in the computer CPU processing-time-allocation system. The dual cascade scheduling algorithm consists of the RR-SJF-EDF-LJF-FCFS scheduling algorithm and the SJF-RR-EDF-LJF-FCFS scheduling algorithm. The RR-SJF-EDF-LJF-FCFS scheduling algorithm is applied if there are available PEVs in the single-phase and two-phase systems. On the other hand, the SJF-RR-EDF-LJF-FCFS scheduling algorithm is employed when the available PEVs are in the three-phase system. The contribution of the proposed algorithm is increased performance of electric energy management of the three-phase system for the postponing investment to extend the capacity of the distribution system with preventing violent voltage level deviation and increasing losses on the three-phase distribution system. The algorithm has the advantage of being an online procedure with no need for a forecasting algorithm. It just uses the existing system structure and devices. Therefore, it will be possible to implement such a system immediately. The results of this study show that the algorithm can limit power and load unbalance in a three-phase system. Moreover, the dual cascade scheduling algorithm can provide good results without the rejection of PEVs charging. In the future, the proposed algorithm should be improved with coordination with home appliances to achieve a high load margin.

This paper is organized as follows: in section 2, the dual cascade scheduling algorithms are introduced, then section 3 deals with the statement of the problem, and the system profiles and system parameters are defined. Section 4 presents the methods, and section 5 illustrates and discusses the results of the simulation model and section 6 offers conclusions.

2. DUAL CASCADE SCHEDULING ALGORITHM

The dual cascade scheduling algorithm based on task management in a computer is proposed in this paper for scheduling PEVs charging. The five principles of CPU scheduling algorithms are applied to allocate electric power to PEVs, including First-Come-First-Serve (FCFS), Shortest-Job-First scheduling (SJF), Longest-Job-First scheduling (LJF), Round-Robin scheduling (RR), and Earliest-Deadline-First scheduling (EDF). The PEVs charging scheduling is based on the charging time for each PEV to schedule and every criterion is applied to decide the order of charging PEVs. The arrival time and departure time are employed by FCFS and EDF to sort the PEVs charging. The charging time is used by LJF, and the time difference between available time and requested time is employed by SJF. The RR scheduling averages the achieved charging time.

The dual cascade scheduling algorithm comprises two cascade scheduling algorithms that involve the overlapping of five scheduling algorithms, as shown in Fig. 7 and Fig. 8. The first cascade scheduling algorithm is the SJF-RR-EDF-LJF-FCFS scheduling algorithm, and the second is the RR-SJF-EDF-LJF-FCFS scheduling algorithm. The objective is problem-solving when the

system has the same data. For instance, if some PEVs have the same time differences, which the SJF scheduling algorithm is unable to sort charging, the next scheduling algorithm is applied to sort PEVs charging, such as RR scheduling, EDF scheduling, LJF scheduling, or FCFS. Table 1 presents the characteristics of the five scheduling algorithms from a preliminary experiment of a single scheduling algorithm. This paper sets the priority of the result indications to be Root-Mean-Square Deviation (RMSD), which refers to the satisfaction of PEV owners, the total PEVs charged energy, the average percentage of achieved charging time, and the minimum percentage of achieved charging time of each PEV. The table shows that the SJF scheduling algorithm can provide low RMSD or high satisfaction of PEV owners, but there are some opportunities where the lowest priority may not be implemented. Next, the RR scheduling algorithm offers a high average percentage of achieved charging time with a few opportunities where some PEVs are rejected. The EDF scheduling algorithm gives high total PEVs charged energy, but there are some opportunities where the lowest priority may not be implemented and there is no guarantee of satisfaction for PEV owners. Likewise, the LJF scheduling algorithm gives high actual power but still has disadvantages like the EDF scheduling algorithm. Last, the FCFS scheduling algorithm enables smooth PEVs charging. However, it has disadvantages similar to the EDF and LJF scheduling algorithms.

Table 1. The characteristics of five scheduling algorithms

Algorithms	Advantages	Disadvantages
FCFS	1. Getting good continuity of PEVs charging.	1. Getting low results. 2. There is no guarantee of satisfaction for PEV owners. 3. There are some opportunities where the lowest priority may not be implemented.
SJF	1. Getting satisfaction for PEV owners.	1. More complexity to sort charging. 2. There are some opportunities where the lowest priority may not be implemented.
LJF	1. Getting high actual power.	1. There are some opportunities where the lowest priority may not be implemented. 2. There is no guarantee of satisfaction for PEV owners.
RR	1. Getting high average value.	1. Getting high interruption. 2. There is no guarantee of satisfaction for PEV owners.
EDF	1. Getting good results.	1. There is no guarantee of satisfaction for PEV owners. 2. There are some opportunities where the lowest priority may not be implemented.

3. PROBLEM STATEMENT

3.1 MODEL OF THE DISTRIBUTION SYSTEM

The distribution system used in this paper consists of a single distributed transformer and 30 houses. The power rating of the transformer is 100 kVA, 3 phases, 400/230 V, 50 Hz. The distribution transformer supplies electricity to the 30 houses, consisting of 2 feeders with 15 houses in each feeder. It is assumed that each house has one PEV plugged in through a control box, which enables two-way communication between the control box and the control centre. When each PEV sends data through the control box to the control centre, the control centre will evaluate and send commands to the control box for PEV charging as communicated to the control centre, as shown in Fig. 1.

3.2 TRANSFORMER LOAD PROFILE

The actual load profile of the 100 kVA distribution transformer is shown in Fig. 2. This graph shows the electric energy consumption for each phase in 24 hours. It can be seen that the high power consumption period generally occurs between 16:00 and 23:00 hours. The power level arranged in descending order from 17:00 to 23:00 hours is phase A, phase C, and phase B, respectively. The maximum power is around 17 kW and unbalance is observed. The minimum power is around 100 watts, occurring from 9:00 to 14:00 hours.

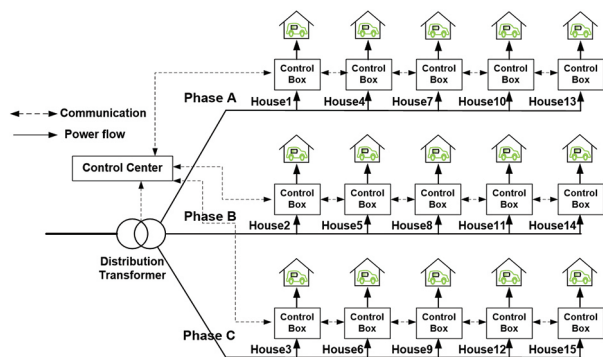


Fig. 1. Representation of one feeder

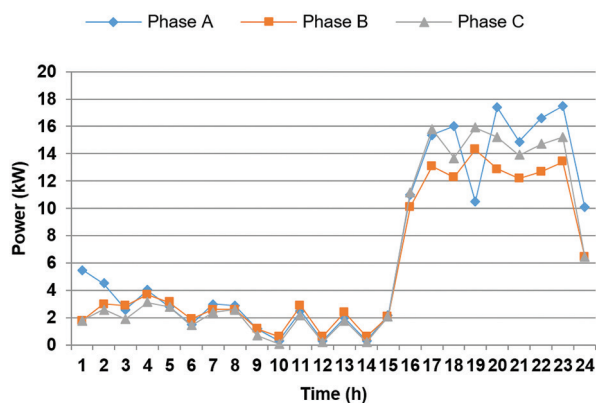


Fig. 2. The actual load profile of the 100 kVA distribution transformer

3.3 TYPE OF PEVS

To render the simulation close to a realistic system, three types of PEVs with different battery energy have been chosen, as follows [33]: 16 kWh Mitsubishi i-MiEV, 24 kWh Nissan Leaf, and 53 kWh Tesla Roadster. They are randomly used by the 30 houses.

3.4 DEFINITIONS OF SYSTEM PARAMETERS

The parameters for electric power and related time used in this paper are defined in Table 2 and Table 3, respectively. Table 2 displays the definition of electric power used in the simulation, which consists of battery charging power defined as 2 kW, limited power as 27 kW per phase calculated at the rating power of the distribution transformer and safety factor, a limited power of unbalanced load assigned 4 kW, load margin is between a limited power and load profile, and phase unbalanced power is between the maximum power and actual power.

Table 3 illustrates the definitions of related charging times used in the simulation. The available time is calculated by the arrival time and departure time. The requested time is calculated by the capacity of the battery (E_{BC}), the end percentage of the state of charge (E_{soc_e}) and the start percentage of the state of charge (E_{soc_s}), the efficiency of the charger (η), and the battery charging power (P_{ch}). The charging time is the relationship between the available time and the requested time. That is, when the requested time is more than the available time, the charging time is the available time. On the other hand, if the requested time is less than the available time, the charging time is the requested time. The time difference is between available time and requested time. Moreover, it can refer to the urgent necessity of the PEV owner.

Table 6 in the appendix presents a summary of all the parameters assumed for each PEV, such as the energy of the battery (E_{BC}), the battery charging power (P_{ch}), the efficiency of the charger (η), the start percentage of the state of charge (E_{soc_s}), the end percentage of the state of charge (E_{soc_e}), the arrival time ($T_{arrival}$), the departure time ($T_{departure}$), the available time ($T_{available}$), the requested time ($T_{requested}$), the charging time ($T_{charging}$), and the time difference (T_{diff}). Since the accumulation of PEVs from their arrival times to departure times in phases A, B and C are different, the system has an unbalanced load.

Table 2. The definition of electric power used in the simulation

Electric power	Specification values
Battery charging power (P_{ch})	2 kW
Limited power (P_{limit})	27 kW
Limited power of unbalanced load ($P_{limit,un}$)	4 kW
Load margin (P_{mar})	$P_{mar}(t) = P_{Limit} - P_{load_pro}(t)$ (1)
Phase unbalanced power ($P_{A,un}, P_{B,un}, P_{C,un}$)	$P_{A, un}(t) = P_{max}(t) - P_{A,ch}$ (2)
	$P_{B, un}(t) = P_{max}(t) - P_{B,ch}$ (3)
	$P_{C, un}(t) = P_{max}(t) - P_{C,ch}$ (4)

Table 3. The definition of related of charging times used in the simulation

Time	Equations
Available time ($T_{available}$)	$T_{available} = T_{departure} - T_{arrival}$ (5)
Requested time ($T_{requested}$)	$T_{requested} = \frac{(E_{soc_e} - E_{soc_s}) * E_{BC}}{P_{ch} * \eta}$ (6)
Charging time ($T_{charging}$)	$T_{charging} = T_{requested}; T_{requested} \leq T_{available}$ (7) $T_{charging} = T_{available}; T_{requested} > T_{available}$
Time difference (T_{diff})	$T_{diff} = T_{available} - T_{requested}$ (8)

$$f(x, \mu, \sigma) = \frac{1}{\sqrt{2\pi\sigma^2}} * e^{-\frac{1}{2} \left(\frac{x-\mu}{\sigma}\right)^2} \quad (9)$$

Where is

- σ Standard deviation value
- μ Mean value

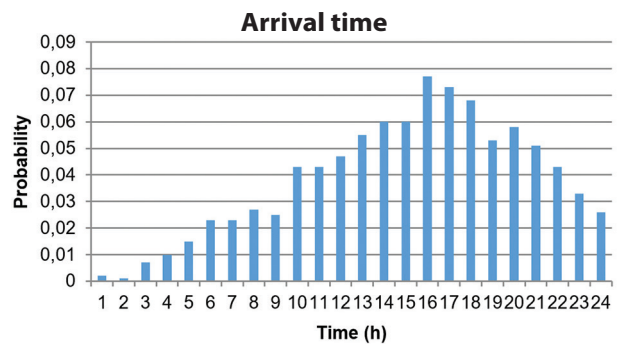


Fig. 3. The probability of arrival time of PEVs in phase A

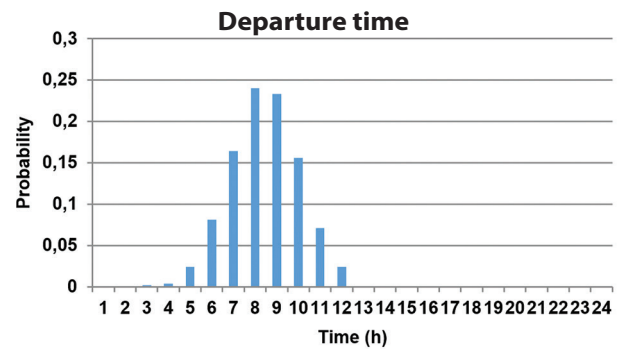


Fig. 4. The probability of departure time of PEVs in phase A

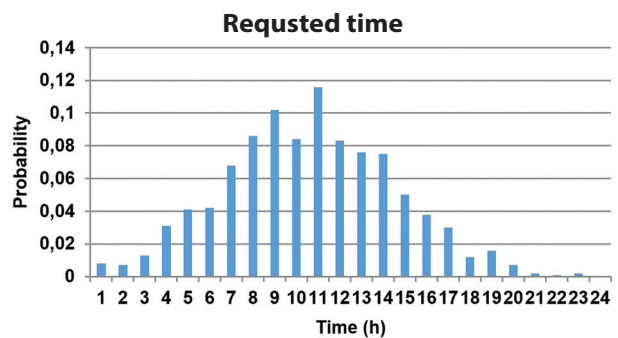


Fig. 5. The probability of requested time of PEVs in phase A

4. METHOD

4.1 SYSTEM CONSTRAINTS

In this paper, the algorithm proposed has been performed to control PEV charging under the following two constraints:

- The actual power (P_{actual}) is power profile (P_{pro}) added to the actual battery charging power of all PEVs ($P_{A,ch}$, $P_{B,ch}$, $P_{C,ch}$) comprising of phases A, B, and C. It must not be higher than the limited power of the transformer (P_{limit}).

$$\begin{aligned} P_{A,actual}(t) &= P_{A,pro}(t) + P_{A,ch}(t) \\ P_{B,actual}(t) &= P_{B,pro}(t) + P_{B,ch}(t) \\ P_{C,actual}(t) &= P_{C,pro}(t) + P_{C,ch}(t) \end{aligned} \quad (10)$$

$$P_{actual} \leq P_{Limit} \quad (11)$$

- The maximum power of unbalanced load in each phase ($P_{max,un}$) is the maximum difference in power between maximum power and the actual battery charging power of all PEVs (P_{ch}) in each phase shown in (2)-(4). It must be less than or equal to the limited power of the unbalanced load ($P_{limit,un}$).

$$P_{max,un} \leq P_{Limit,un} \quad (12)$$

4.2 RESULT INDICATORS

- Root-mean-square deviation (RMSD): the average deviation of value difference between the requested time and achieved charging time. RMSD refers to the satisfaction of PEV owners.

$$RMSD = \left(\frac{1}{N} \sum_{i=1}^N (T_{request,i} - T_{achieved,i})^2 \right)^{\frac{1}{2}} \quad (13)$$

- Total PEVs charged energy: the algorithm aims to maximize the total electric energy to all PEVs and the electric energy consumption from the distribution transformer.

$$Total \ PEVs \ Charged \ Energy = \sum_{i=1}^N E_i \quad (14)$$

where E_i is the electric energy of i^{th} PEV, N is the number of PEVs

- The average percentage of achieved charging time: The charging time is arranged to achieve the maximum average charging of all PEVs.

$$Average \ \%T_{achieved} = \frac{\sum_{i=1}^N T_i}{N}$$

Where T_i is the percentage of achieved charging time of i^{th} PEV, and N is the number of PEVs.

A flow chart of the energy management of PEVs charging is illustrated in Fig. 6. It consists of two main processes. The first process is to calculate limited power in the system including load margin, unbalanced power, etc., while the second process is applying the dual cascade scheduling algorithms to allocate charging power to the PEVs by using the functions set out in the previous section. In the first step of the first process, the variables for the algorithm are defined, consisting of the battery charging power (P_{ch}), the limited power (P_{limit}), and the limited power of unbalanced load ($P_{limit,un}$). Subsequently, the data for each PEV is collected from the commencement of charging, comprising their arrival time ($T_{i,arrival}$), departure time ($T_{i,departure}$), the total battery charging power of all PEVs required in each phase ($P_{A,PEV}(t)$, $P_{B,PEV}(t)$, $P_{C,PEV}(t)$) and the transformer's load profile ($P_{load,pro}(t)$). The third step involves calculating the phase loading margins ($P_{A,mar}(t)$, $P_{B,mar}(t)$, $P_{C,mar}(t)$), the power of unbalanced load of each phase ($P_{A,un}(t)$, $P_{B,un}(t)$, $P_{C,un}(t)$), the requested time ($T_{i,request}$), the available time ($T_{i,available}$) and time difference ($T_{i,diff}$), as well as the charging time ($T_{i,charging}$) by using (1)-(8). Then the maximum and minimum values of the loading margin ($P_{max,mar}(t)$, $P_{min,mar}(t)$) and power of unbalanced load ($P_{max,un}(t)$, $P_{min,un}(t)$) are selected. In the next step, the total available charging power of all the PEVs in each phase ($P_{A,ch}(t)$, $P_{B,ch}(t)$, $P_{C,ch}(t)$) are selected between the minimum values of the total battery charging power of all the PEVs ($P_{A,PEV}(t)$, $P_{B,PEV}(t)$, $P_{C,PEV}(t)$) and the loading margin of each phase ($P_{A,mar}(t)$, $P_{B,mar}(t)$, $P_{C,mar}(t)$). Then the maximum power of unbalanced load ($P_{max,un}(t)$) can be computed and checked within the system constraints shown in (12). If the maximum power of unbalanced load ($P_{max,un}(t)$) exceeds the limited power of unbalanced load ($P_{limit,un}$), PEVs with 2 kW charging capacity are eliminated one at a time until the system is restored to the constraints. In this step, the system will get the maximum actual power. The final step of the first process is to calculate the total number of PEVs that can be charged in each phase of the distribution system based on the actual battery charging power of all PEVs ($P_{A,ch}(t)$, $P_{B,ch}(t)$, $P_{C,ch}(t)$).

In the second process, the situation is evaluated every hour. The number of PEVs from the first process is scheduled by the dual cascade scheduling algorithms shown in Fig. 7. It shows the specific PEVs charging schedule of phase A. There are three conditions for PEVs scheduling. In the first condition, if the power margin (P_{mar}) is more than the battery charging power of all PEVs ($P_{A,PEV}$), the controller commands the charging of all PEVs. In the second condition, when the power margin is less than the battery charging power of all PEVs and there are available PEVs in the single-phase and dual-phase, the controller uses the RR-SJF-EDF-LJF-FCFS for PEVs charging schedule. In the last condition, both the power margin is less than the charging power and there are available PEVs in the three-phase system, so the controller applies the SJF-RR-EDF-LJF-FCFS for PEVs charging

schedule. This algorithm is an online system. Therefore, it is repeated every hour to evaluate the situation of the system and adjusts the newly calculated value. It will be repeated until a stop command is achieved.

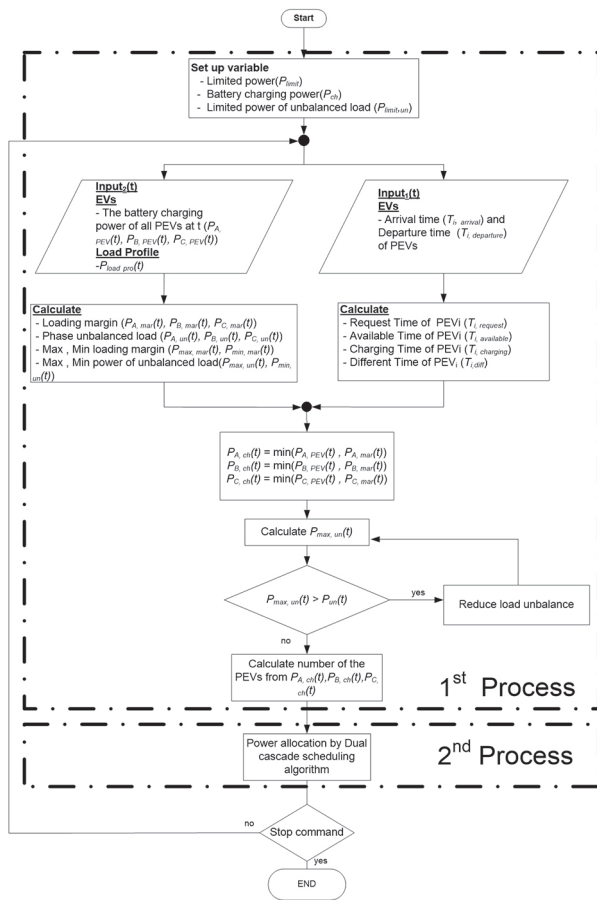


Fig. 6. Flow chart of electric energy management for PEV charging

5. SIMULATION RESULTS AND DISCUSSION

5.1 SIMULATION RESULTS

Table 5 reveals the simulation results of coordinating PEVs charging in the electricity distribution system for residential houses. The simulation scenarios consist of three PEVs penetration levels and occurring PEVs load balance and imbalance in the three-phase distribution system. The uncontrolled charging and four scheduling algorithms, which consist of the dual cascade scheduling algorithm, the scored priority scheduling, the real-time scheduling algorithm, and the improved queuing-theory-based scheduling, are applied for power allocation to each PEV.

First, the simulation results of 25% PEVs penetration level are illustrated in Table 5. Occurring PEVs load in the single-phase system is the first scenario. The uncontrolled charging, even though provides the best RMSD, total PEVs charged energy, and the average percentage of achieved charging time but violates the constraints of power limitation and power of unbal-

anced. In contrast, all four algorithms can control power under constraints. However, the dual cascade scheduling algorithm provides the best percentage average of achieved charging time, 23.8%.

Next, appearing PEVs load in the two-phase system is 50% of the PEVs penetration level. Likewise, the uncontrolled charging still provides the best results and violates the constraints, and the dual cascade scheduling algorithm providing RMSD, total PEVs charged energy, and the average percentage of achieved charging time is 6.4, 120 kWh, and 41.3%, respectively is a good method for allocating power to each PEV, while other methods reject some PEVs charging, 0%. For the 100% PEVs penetration level, the PEVs load presents in the three-phase system. The dual cascade scheduling algorithm that delivers 0.69, 554 kWh, and 99%, is a good result for this scenario.

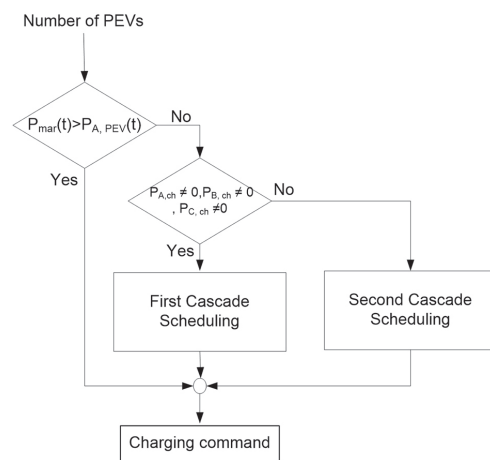


Fig. 7. Power allocation by the dual cascade scheduling algorithm in phase A

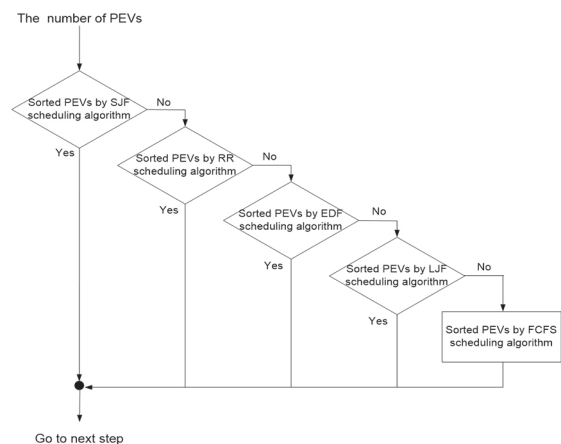


Fig. 8. The first cascade scheduling algorithm

Table 4. Comparison of loss in the power line

Uncontrolled charging			
Phase A	Phase B	Phase C	Total
7,917.615	8,343.459	9,933.399	26,194.473
Controlled charging			
7,100.325	8,278.902	8,304.190	23,683.417

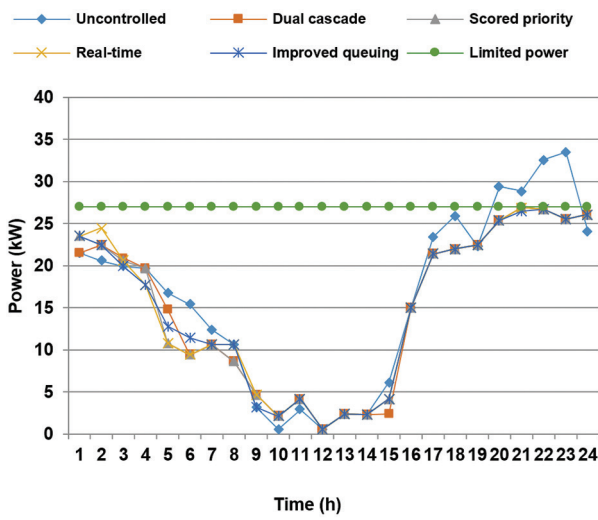


Fig. 9. The actual power of each scheduling algorithm

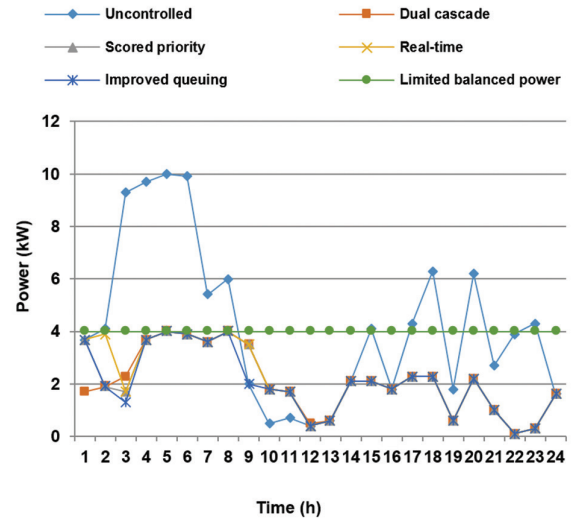


Fig. 10. Power of unbalanced load of all scheduling algorithms

Table 5. Simulation results of each method

Algorithms	% Achieved charging time (%)						Average (%)	RMSD	Total PEVs charged energy (kWh)	Max. Actual power (kW)	Max. power of unbalanced load (kW)
	Phase A		Phase B		Phase C						
	Max.	Min.	Max.	Min.	Max.	Min.					
25% PEVs penetration or 8 PEVs (Only 8 PEVs in phase A)											
Uncontrolled	100	-	-	-	-	-	100	0	152	31.4	18.5
Dual cascade scheduling	33.3	18.1	-	-	-	-	23.8	7.3	36	17.5	4.5
Scored priority	44.4	11.1	-	-	-	-	23.1	7.3	36	17.5	4.5
Real-time scheduling	45.4	10	-	-	-	-	23.1	7.3	36	17.5	4.5
Improved queuing-theory-based-scheduling	45.4	10	-	-	-	-	23.1	7.3	36	17.5	4.5
50% PEVs penetration or 15 PEVs(10 PEVs in phase A, and 5 PEVs in phase B)											
Uncontrolled	100		100		-	-	100	1.2	288	31.7	16.2
Dual cascade scheduling	37.5	22.2	100	46.6	-	-	41.3	6.4	120	19.4	4.0
Scored priority	60	0	90.9	28.5	-	-	39.2	6.3	122	19.4	4.0
Real-time scheduling	66.6	0	83.3	14.2	-	-	39.2	6.2	122	19.4	4.0
Improved queuing-theory-based-scheduling	66.6	0	75	28.5	-	-	38.5	6.1	122	19.4	4.0
100 % PEVs penetration of 30 PEVs (10 PEVs in phase A, 10 PEVs in phase B, and 10 PEVs in phase C)											
Uncontrolled	100		100		100		100	0.54	560	30.9	6.3
Dual cascade scheduling	100		100	87.5	100		99.0	0.69	554	26.9	4.0
Scored priority	100		100	75	100		97.9	0.98	546	26.9	4.0
Real-time scheduling	100		100	87.5	100		98.7	0.66	552	26.9	4.0
Improved queuing-theory-based-scheduling	100		100	91.6	100		99.1	0.69	554	26.9	4.0

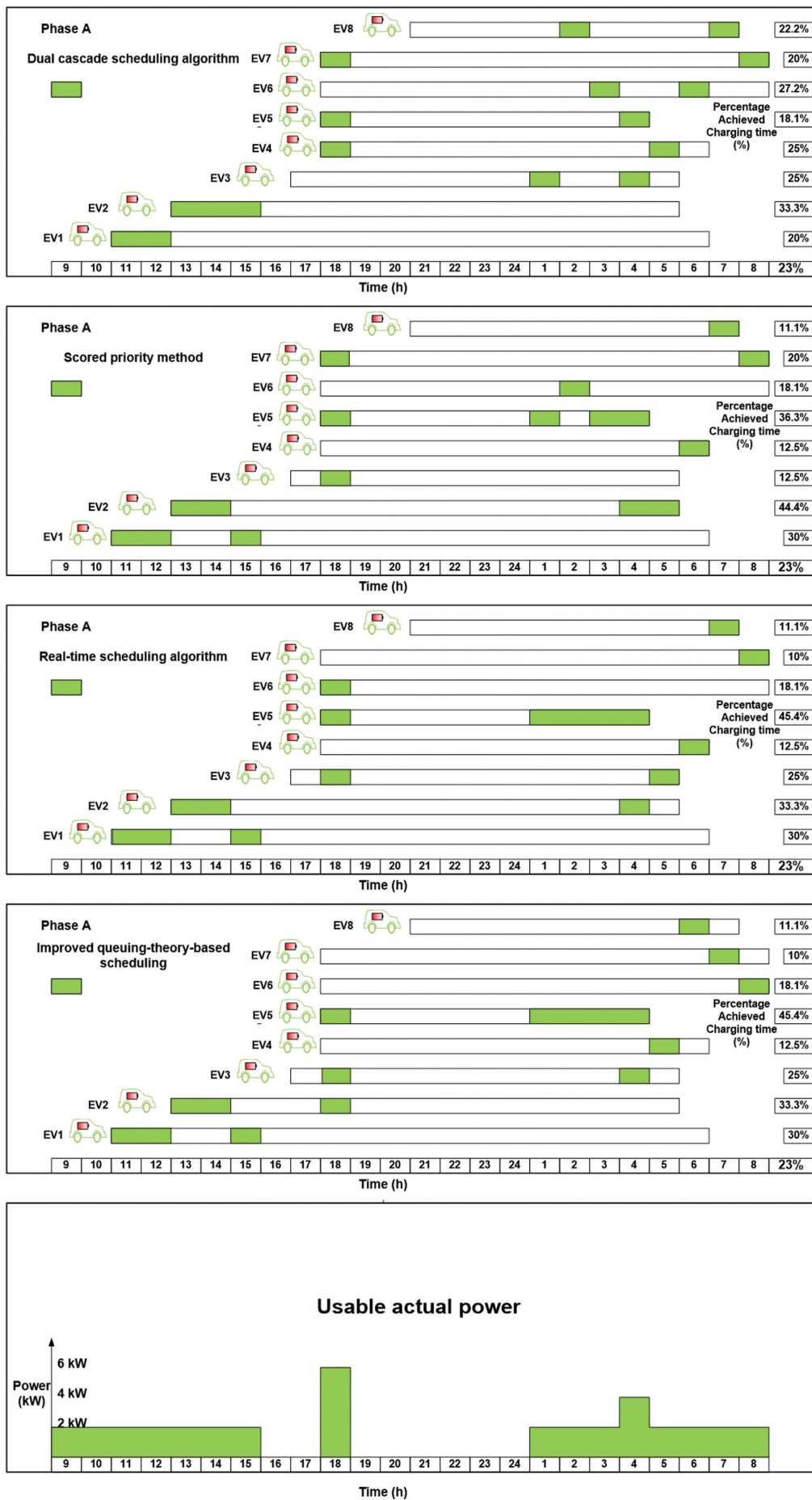


Fig. 11. PEVs charging behavior of each algorithm

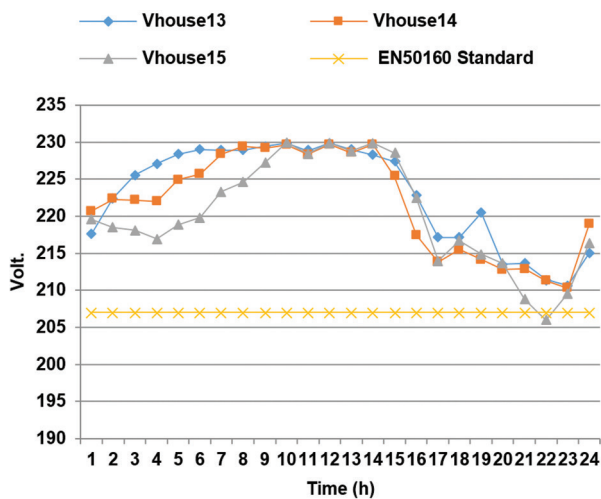


Fig. 12. Voltage level profiles the farthest houses under uncontrolled charging situation

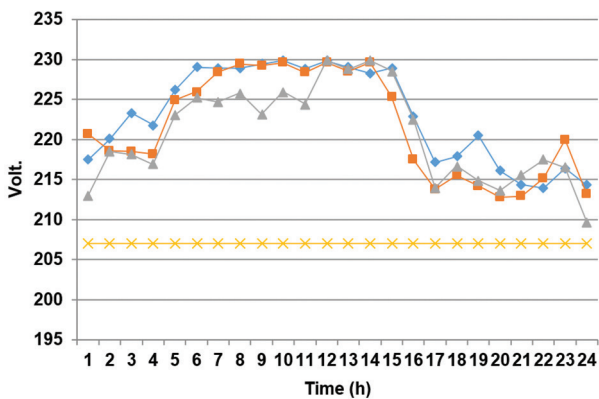


Fig. 13. Voltage level profiles the farthest houses under controlled charging situation

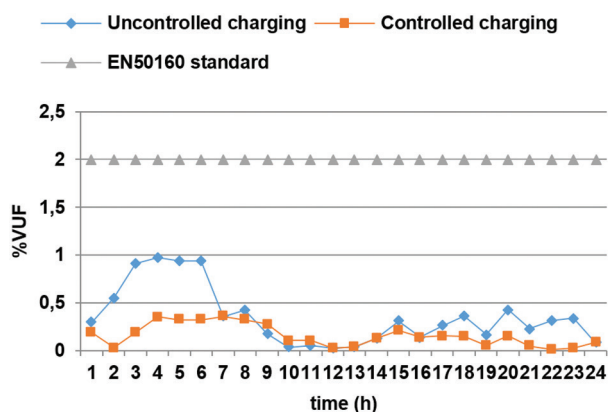


Fig. 14. Percentage of voltage unbalance factor profiles

5.2 DISCUSSION

For the results described above, all four scheduling algorithms can provide similar results because the input variables for processing are requested time and available time. However, the different processes will provide the different results as follows.

First, the dual cascade scheduling algorithm based on task management in a computer operation schedules PEVs charging by charging time gained from requested time and available time. Few opportunities exist that some PEVs are rejected from charging by this algorithm.

Second, the scored priority method based on fuzzy logic to generate the scores for PEVs scheduling [23] employing requested time and available time to be input variables of fuzzy mechanism can provide good RMSD in occurring PEVs load imbalance.

Next, the real-time scheduling algorithm based on the proportion between the requested time and the available time to schedule PEVs charging [29] provides quite a low average electric energy cost.

Finally, the improved queuing-theory-based scheduling algorithm based on the least slack time rate first scheduling for sorting PEVs charging [30] can result in good RMSD in appearing PEVs load imbalance and gives low average electric energy cost in some scenarios.

All scheduling algorithms based on requested time and available time to generate the weight for sorting PEVs are the simple method and provide good results, however, all three scheduling methods comprised scored priority method, real-time scheduling, and improved queuing-theory-based scheduling are inflexible methods. There is a high possibility to have rejected PEVs charging when there are PEVs in a single-phase or two-phase, moreover if the method gets data that have the same value, it can't sort the PEVs. The dual cascade scheduling algorithm can handle these problems. When there are PEVs in a single-phase or two-phase, it applies RR-SJF-EDF-LJF-FCFS to sort PEVs, and SJF-RR-EDF-LJF-FCFS is applied when there are PEVs in three phases, while it gets the same data the next scheduling algorithm is applied to sort PEVs such as shortest-job-first scheduling (SJF) for RR-SJF-EDF-LJF-FCFS and Round-Robin scheduling (RR) for SJF-RR-EDF-LJF-FCFS.

Fig. 9 reveals the actual power from using each scheduling algorithm. All lines have a similar shape and all scheduling algorithms can control power under power limitation, except uncontrolled charging, which takes the maximum power over limited power. The electrical devices in the distribution system may be damaged. Likewise, Fig. 10 illustrates the power of an unbalanced load from each scheduling algorithm. The uncontrolled charging provides high power, which violates the power of unbalanced load limitation. This result makes the voltage level drop and the electrical device may be damaged. From using each scheduling algorithm, the line graph displays that they can control the power of an unbalanced load under the constraint. The period of low power means there are many PEVs in the three-phase distribution system. In contrast, high power refers to having few PEVs and existing PEVs in the system unbalance.

Fig.11 presents the PEVs charging behavior of each algorithm. The 8 PEVs in a single-phase system is this

situation. The solid color is PEV charging, and the transparent color is no PEV charging. The lowest chart shows the usable power resulting from the first process. The maximum power occurring from 18:00 to 19:00 hours is 6 kW which can charge 3 PEVs, and the minimum power is zero from 16:00 to 18:00 hours and 19:00 to 1:00 hours. In this situation, the dual cascade scheduling algorithm provides the average charging time, 2 hours, to each PEV while other algorithms offer the charging time under the urgent factor making some PEVs have short charging time, just an hour, or rejects charging.

Fig. 12 and Fig. 13 show voltage level profiles in the distribution system. Fig. 14 indicates the percentage of voltage unbalance factors (%VUF) compared with standard EN50160 [34]. The distribution system consists of two feeders with 15 houses in each feeder. The backward/forward sweep method is applied to analyse the voltage level in the three-phase distribution system. $V_{house_{13}}$, $V_{house_{14}}$, and $V_{house_{15}}$ are voltage levels of the farthest houses (13th, 14th, and 15th houses) in phase A, phase B, and phase C, respectively.

The standard EN50160 defines the variation of voltage level to be $\pm 10\%$ and the percentage of voltage unbalance factor (%VUF) is lower than 2%. Fig. 12 illustrates the voltage level based on the uncontrolled charging situation. The results show that the voltage level is lower than the standard at 22 hours. Fig. 13 indicates that the voltage levels of the farthest houses under controlled charging are above the standard, even in the worst case of phase C. Moreover, it can provide a better percentage of voltage unbalance factor, as shown in Fig. 14.

Table 4 indicates the comparison of losses in the power line. The losses in the power line decrease from 26,194.473 watts to 23,683.417 watts with the controlled charging.

In the future, the proposed algorithm should be improved to be able to coordinate control with home appliances for higher electric energy in PEVs charging.

6. CONCLUSION

A simple electric power management system for PEV charging of the electricity distribution system proposed consists of two processes. The first process calculates the usable power in the distribution system to control the charging power under the limited power and the limited power of the unbalanced load of the three-phase distribution transformer. The second process uses the dual cascade scheduling algorithms to optimally allocate power to PEVs under the power constraints. The achievement of management is measured by the value of root-mean-square deviation (RMSD), the total PEVs charged energy, and the average percentage of achieved charging time under the power and load unbalance limitation. The dual cascade scheduling algorithm consists of RR-SJF-EDF-LJF-FCFS and SJF-RR-EDF-LJF-FCFS for use with available PEVs in single, dual-phase and, three-phase systems. The results show that the dual cascade scheduling algorithm can provide good results and improve the possibility of PEVs charging rejection. This study demonstrates that the ability of the power distribution system to charge PEVs can be improved without the need to invest in increases in its capacity. Moreover, the proposed system has the advantage of being able to be implemented by simply installing a control box with a suitable plug-in at each house, after which the system can be controlled centrally at the distribution transformer without the need for any modification to the structure of the distribution system. In the future, the proposed algorithm will be improved to enable higher total PEVs charged energy by electric energy management to co-operate home appliances, especially the improvement of the cascade scheduling algorithm or studying other related methods.

7. ACKNOWLEDGMENT

This work was supported financially and through facility provision by the Faculty of Engineering and the Graduate School at Prince of Songkla University (PSU) and the Office of the Higher Education Commission (OHEC), Thailand.

8. APPENDIX

Table 6. The summary of all variables of PEVs

No.	Start percentage state of charge (%)	End percentage state of charge (%)	Energy of battery (Wh)	Battery Charging power (w)	Efficiency of charger (%)	Arrival time (h)	Departure time (h)	Available time (h)	Requested time (h)	Charging time (h)	Time difference (h)	
Phase A												
1	60	90	53,000	2,000	80	16:00	7:00	15.00	10.00	10.00	5.00	
2	50	90	53,000	2,000	80	20:00	8:00	12.00	14.00	12.00	-2.00	
3	40	90	53,000	2,000	80	0:00	9:00	9.00	7.00	9.00	-8.00	
4	50	90	24,000	2,000	80	17:00	10:00	17.00	6.00	6.00	9.00	
5	10	90	24,000	2,000	80	13:00	9:00	20.00	12.00	12.00	8.00	
6	20	90	24,000	2,000	80	16:00	7:00	15.00	11.00	11.00	4.00	
7	30	90	16,000	2,000	80	19:00	5:00	10.00	6.00	6.00	4.00	
8	50	90	16,000	2,000	80	14:00	6:00	16.00	4.00	4.00	12.00	
9	20	90	16,000	2,000	80	21:00	6:00	9.00	7.00	7.00	2.00	
10	10	90	16,000	2,000	80	18:00	7:00	13.00	8.00	8.00	5.00	
Total			295,000									
Phase B												
1	60	90	53,000	2,000	80	22:00	6:00	8.00	10.00	8.00	-2.00	
2	50	90	53,000	2,000	80	19:00	7:00	12.00	14.00	12.00	-2.00	
3	40	90	53,000	2,000	80	17:00	8:00	15.00	17.00	15.00	-2.00	
4	50	90	53,000	2,000	80	20:00	7:00	11.00	14.00	11.00	-3.00	
5	20	90	53,000	2,000	80	19:00	6:00	11.00	24.00	11.00	-13.00	
6	20	90	24,000	2,000	80	14:00	8:00	18.00	11.00	11.00	7.00	
7	40	90	24,000	2,000	80	15:00	6:00	15.00	8.00	8.00	7.00	
8	10	90	24,000	2,000	80	16:00	9:00	17.00	12.00	12.00	5.00	
9	20	90	16,000	2,000	80	21:00	10:00	13.00	7.00	7.00	6.00	
10	30	90	16,000	2,000	80	0:00	6:00	6.00	6.00	6.00	0.00	
Total			369,000									
Phase C												
1	60	90	53,000	2,000	80	15:00	7:00	14.00	10.00	10.00	2.00	
2	40	90	53,000	2,000	80	15:00	8:00	17.00	17.00	17.00	0.00	
3	50	90	53,000	2,000	80	20:00	8:00	12.00	14.00	12.00	-2.00	
4	50	90	53,000	2,000	80	1:00	9:00	8.00	14.00	8.00	-6.00	
5	40	90	53,000	2,000	80	19:00	8:00	13.00	17.00	13.00	-4.00	
6	60	90	53,000	2,000	80	20:00	11:00	15.00	10.00	10.00	5.00	
7	50	90	53,000	2,000	80	21:00	7:00	10.00	14.00	10.00	-4.00	
8	20	90	24,000	2,000	80	20:00	6:00	10.00	11.00	10.00	-1.00	
9	10	90	24,000	2,000	80	23:00	4:00	5.00	12.00	5.00	-7.00	
10	30	90	16,000	2,000	80	16:00	6:00	14.00	6.00	6.00	8.00	
Total			435,000									

9. REFERENCES

- [1] C. H. Dharmakeerthi, N. Mithulananthan, T. K. Saha, "Impact of electric vehicle fast charging on power system voltage stability", *International Journal of Electrical Power & Energy Systems*, Vol. 57, 2014, pp. 241–249.
- [2] N. Leemput, F. Geth, J. Van Roy, A. Delnooz, J. Buscher, J. Driesen, "Impact of Electric Vehicle On-Board Single-Phase Charging Strategies on a Flemish Residential Grid", *IEEE Transactions on Smart Grid*, Vol. 5, No. 4, 2014, pp. 1815–1822.
- [3] K. Clement-Nyns, E. Haesen, J. Driesen, "The impact of vehicle-to-grid on the distribution grid", *Electric Power Systems Research*, Vol. 81, No. 1, 2011, pp. 185–192.
- [4] G. Razeghi, L. Zhang, T. Brown, S. Samuelsen, "Impacts of plug-in hybrid electric vehicles on a residential transformer using stochastic and empirical analysis", *Journal of Power Sources*, Vol. 252, 2014, pp. 277–285.
- [5] A. D. Hilshey, P. D. H. Hines, P. Rezaei, J. R. Dowds, "Estimating the Impact of Electric Vehicle Smart Charging on Distribution Transformer Aging", *IEEE Transactions on Smart Grid*, Vol. 4, No. 2, 2013, pp. 905–913.
- [6] M. A. S. Masoum, P. S. Moses, K. M. Smedley, "Distribution transformer losses and performance in smart grids with residential Plug-In Electric Vehicles", *Proceedings of ISGT 2011, Anaheim, CA, USA, 17-19 January 2011*, pp. 1–7.
- [7] A. A. Eajal, M. F. Shaaban, E. F. El-Saadany, K. Ponambalam, "Fuzzy Logic-Based Charging Strategy for Electric Vehicles Plugged into a Smart Grid", *Proceedings of the IEEE International Conference on Smart Energy Grid Engineering, Oshawa, ON, Canada, 17-19 August 2015*, pp. 1–6.
- [8] S. Shao, T. Zhang, M. Pipattanasomporn, S. Rahman, "Impact of TOU rates on distribution load shapes in a smart grid with PHEV penetration", *Proceedings of PES T&D 2010, New Orleans, LA, USA, 19-22 April 2010*, pp. 1–6.
- [9] S. Xu et al., "Ant-Based Swarm Algorithm for Charging Coordination of Electric Vehicles", *International Journal of Distributed Sensor Networks*, Vol. 9, No. 5, 2013, pp. 1–13.
- [10] L. Xia, J. de Hoog, T. Alpcan, M. Brazil, I. Mareels, D. Thomas, "Electric Vehicle Charging: A Non-cooperative Game Using Local Measurements", *IFAC Proceedings Volume*, Vol. 47, No. 3, 2014, pp. 5426–5431.
- [11] Z. Zhu, S. Lambotharan, W. H. Chin, Z. Fan, "A Mean Field Game Theoretic Approach to Electric Vehicles Charging", *IEEE Access*, Vol. 4, 2016, pp. 3501–3510.
- [12] K. Zhang et al., "Optimal decentralized valley-filling charging strategy for electric vehicles", *Energy Conversion and Management*, Vol. 78, 2014, pp. 537–550.
- [13] L. Zhang, F. Jabbari, T. Brown, S. Samuelsen, "Coordinating plug-in electric vehicle charging with electric grid: Valley filling and target load following", *Journal of Power Sources*, Vol. 267, 2014, pp. 584–597.
- [14] R. Mehta, D. Srinivasan, A. M. Khambadkone, J. Yang, A. Trivedi, "Smart Charging Strategies for Optimal Integration of Plug-In Electric Vehicles Within Existing Distribution System Infrastructure", *IEEE Transactions on Smart Grid*, Vol. 9, No. 1, 2018, pp. 299–312.
- [15] T. Mao, X. Zhang, B. Zhou, "Intelligent Energy Management Algorithms for EV-charging Scheduling with Consideration of Multiple EV Charging Modes", *Energies*, Vol. 12, No. 2, 2019, pp. 1–17.
- [16] M. Pipattanasomporn, M. Kuzlu, S. Rahman, "An Algorithm for Intelligent Home Energy Management and Demand Response Analysis", *IEEE Transactions on Smart Grid*, Vol. 3, No. 4, 2012, pp. 2166–2173.
- [17] A. S. Masoum, S. Deilami, P. S. Moses, M. A. S. Masoum, A. Abu-Siada, "Smart load management of plug-in electric vehicles in distribution and residential networks with charging stations for peak shaving and loss minimisation considering voltage regulation", *IET Generation, Transmission & Distribution*, Vol. 5, No. 8, 2011, pp. 877–888.
- [18] S. Deilami, A. S. Masoum, P. S. Moses, M. A. S. Masoum, "Real-Time Coordination of Plug-In Electric Vehicle Charging in Smart Grids to Minimize Power Losses and Improve Voltage Profile", *IEEE Transactions on Smart Grid*, Vol. 2, No. 3, 2011, pp. 456–467.

- [19] Y. Azzougui and A. Recioui, "Hardware and software load power control in smart home applications based on Taguchi optimisation technique", *International Journal of Intelligent Systems Design and Computing*, Vol. 2, No. 3-4, 2018, pp. 203–223.
- [20] A. Recioui, "Home Load-Side Management in Smart Grids Using Global Optimization"; *Research Anthology on Multi-Industry Uses of Genetic Programming and Algorithms*, IGI Global, 2021.
- [21] A. Recioui, F. Z. Dekhandji, "Implementation of Load Control for Smart Metering in Smart Grids", *Book chapter in: Optimizing and Measuring Smart Grid Operation and Control*, IGI Global, 2021.
- [22] B. Sun, Z. Huang, X. Tan, D. H. K. Tsang, "Optimal Scheduling for Electric Vehicle Charging With Discrete Charging Levels in Distribution Grid", *IEEE Transactions on Smart Grid*, Vol. 9, No. 2, 2018, pp. 624–634.
- [23] E. Akhavan-Rezai, M. F. Shaaban, E. F. El-Saadany, F. Karray, "Online Intelligent Demand Management of Plug-In Electric Vehicles in Future Smart Parking Lots", *IEEE Systems Journal*, Vol. 10, No. 2, 2016, pp. 483–494.
- [24] K. N. Kumar, B. Sivaneasan, P. L. So, "Impact of Priority Criteria on Electric Vehicle Charge Scheduling", *IEEE Transactions on Transportation Electrification*, Vol. 1, No. 3, 2015, pp. 200–210.
- [25] K. W. Chan and X. Luo, "Real-time scheduling of electric vehicles charging in low-voltage residential distribution systems to minimise power losses and improve voltage profile", *IET Generation, Transmission & Distribution*, Vol. 8, No. 3, 2014, pp. 516–529.
- [26] B. Geng, J. K. Mills, D. Sun, "Two-Stage Charging Strategy for Plug-In Electric Vehicles at the Residential Transformer Level", *IEEE Transactions on Smart Grid*, Vol. 4, No. 3, 2013, pp. 1442–1452.
- [27] Z. Wang and R. Paranjape, "Optimal scheduling algorithm for charging electric vehicle in a residential sector under demand response", *Proceedings of the IEEE Electrical Power and Energy Conference*, London, ON, Canada, 26-28 October 2015, pp. 45–49.
- [28] E. Akhavan-Rezai, "Priority-based Charging Coordination of Plug-in Electric Vehicles in Smart Parking Lots", *Proceedings of the IEEE PES General Meeting*, National Harbor, MD, USA, 27-31 July 2014, pp. 1–5.
- [29] J. Kang, S. J. Duncan, D. N. Mavris, "Real-time Scheduling Techniques for Electric Vehicle Charging in Support of Frequency Regulation", *Procedia Computer Science*, Vol. 16, 2013, pp. 767–775.
- [30] P. Han, J. Wang, Y. Han, Y. Li, "Resident Plug-In Electric Vehicle Charging Modeling and Scheduling Mechanism in the Smart Grid", *Mathematical Problems in Engineering*, Vol. 2014, 2014, pp. 1–8.
- [31] S. Panichtanakom, K. Chalermyanont, S. Thienmontri, "Study of Plug-in Electric Vehicles Charging by Using Load Shaving Method Based on TOU in Distribution System: A Case Study in Thailand", *Proceedings of the International Electrical Engineering Congress*, Krabi, Thailand, 7-9 March 2018, pp. 1–4.
- [32] A. Silberschatz, P. B. Galvin, G. Gagne, "Operating System Concepts", 9th Edition, John Wiley & Sons, Inc, 2012.
- [33] M. Yilmaz and P. T. Krein, "Review of Battery Charger Topologies, Charging Power Levels, Infrastructure for Plug-In Electric and Hybrid Vehicles", *IEEE Transactions on Power Electronics*, Vol. 28, No. 5, 2013, pp. 2151–2169.
- [34] H. Markiewicz, A. Klajn, "Voltage Disturbances Standard EN 50160 Voltage Characteristics in Public Distribution Systems", *Wroclaw University of Technology*, 2004.

Comparative study of power smoothing techniques produced by a wind energy conversion system

Case Study

Hind Elaimani

Mohammed V University in Rabat, Ecole Nationale Supérieure d'Arts et Métiers (ENSAM), Research Center of Engineering and Health Sciences and Technologies (STIS) Avenue de l'Armée Royale, Rabat, Morocco.
h.elaimani@gmail.com
ID: <https://orcid.org/0000-0002-6075-2883>

Noureddine Elmouhi

Mohammed V University in Rabat, Ecole Nationale Supérieure d'Arts et Métiers (ENSAM), Research Center of Engineering and Health Sciences and Technologies (STIS) Avenue de l'Armée Royale, Rabat, Morocco.
n.elmouhi@gmail.com
ID : <https://orcid.org/0000-0002-3379-7568>

Ahmed Essadki

Mohammed V University in Rabat, Ecole Nationale Supérieure d'Arts et Métiers (ENSAM), Research Center of Engineering and Health Sciences and Technologies (STIS) Avenue de l'Armée Royale, Rabat, Morocco.
ahmed.essadki1@gmail.com

Rachid Chakib

Laboratory of Innovation in Management and Engineering for Enterprise (LIMIE), ISGA Rabat Institut supérieur d'ingénierie et des affaires, 27 Avenue Oqba, Agdal, Rabat, Morocco.
rachid.chakib@isga.ma

Abstract – *This paper aims to present and compare two techniques used to smooth the injected power in the grid from a doubly-fed induction generator (DFIG) based conversion system. The first technique based on an inertial storage system while the second is founded on limiting the power captured by the wind turbine. The overall system composed of a wind energy conversion system (WECS) allowing to convert a wind power into electric power. It is controlled by two converters, grid side converter and a rotor side converter, both are controlled by sliding mode. The storage system is used to consume power which exceeds the setpoint due to storing it or producing more in the event of a lack, the system is controlled through the flywheel side converter by the sliding mode. Numerical simulations were carried out using Matlab/Simulink software.*

Keywords: DFIG modelling, Power smoothing, Sliding mode, Wind Energy

1. INTRODUCTION

In recent years, the need for electricity has continued to increase. Research projects have focused on clean and inexhaustible sources of energy, of which renewable energy is part. More precisely and thanks to its advantages, researchers have turned to wind energy.

Different structure of wind energy conversion system exists, the most used one is based on DFIG. It has emerged as one of the most economical and efficient solutions for the electrical energy generation. It is composed of a doubly-fed induction generator DFIG, with a direct connection of the stator to the grid, connection of its wound rotor through two power converters [1]. The first converter is the RSC (Rotor Side Converter) it controls the DFIG's active and reactive power, the second GSC (Grid Side Converter) it controls the DC link's voltage. Several researches have been carried out on the control of these power converters in order to properly control the generated power.

Different techniques exist to control the converters such as the PI regulators, the Backstepping technique, the direct power control, the Active Disturbance Rejection Control (ADRC), the direct torque control and the control by sliding mode, which will be used in this work. These techniques are not efficient against the wind fluctuation, it remains an inevitable and direct threat. In fact, the wind fluctuations appear at the level of the produced power, therefore we see that the power produced does not follow its reference, when the wind speed decreases, we produce less than what is required, when it is the reverse, we produce more than we need.

To remedy this problem, it is necessary to act either before the conversion on the mechanical part by reducing the blades' rotational speed acting on their orientation, or after the conversion by using the storage of energy technique [2]. In the mechanical part, we act on the blades' orientation angle to reduce the speed of the wind turbine and subsequently reduce or even limit the electrical produced power, by using the blades

orientation system. An ESS (energy storage system) contributes to the energy balance between production and need. It provides energy when needed and stores it at high wind speeds where energy demand is reduced, this balance generates a smooth power which respects its reference.

Indeed, there are several techniques of energy storage, such as storage by hydraulic pumping of energy, storage in the form of potential energy from compressed air, storage in the form of chemical energy and storage of kinetic energy in a spinning mass also called a flywheel. All these methods are widely studied in [3], the flywheel technique is further developed in [3,4,5,6].

Energy capacity, self-discharge, environmental reliability and potential are the main factors in the choice of an energy storage system, according to the comparative study carried out in [7] therefore and according to its comparison's results, the ESS using flywheel are favorably proposed.

Many works have focused on the regulation of the produced power which depends on the converted power (at the DFIG's output) and the power of the ESS. Different control laws have been developed to ensure the balance between the supplied power and the stored power from or in the ESS.

In [6] the flywheel energy storage system consists of an electronic power converter supplying a squirrel-cage induction machine coupled to a flywheel. The squirrel cage machine is controlled through its flux, the latter is calculated using the flux weakening algorithm. The control is provided by a traditional linear proportional-integral (PI) controller. The same regulators are used in [2], [8] in addition to a fuzzy logic-based supervisor to compute the regulated power value. However, taking into account the system parameters' variation (due, especially to modelling uncertainties and some physical phenomena), other control laws have been proposed as in [4] the author used the same structure in [2],[8] but with a control based on the backstepping technique.

Most of the works cited above are concerned with the power smoothing using an ESS by controlling either the flux or the torque, subsequently a supervision block based on fuzzy logic to control the power. In this paper we tried to directly control the ESS by using the sliding mode technique to try to achieve higher performances. we compared this new approach with the technique using the blades orientation system limiting the pitch angle of the blades known as pitch control, to see the advantages and disadvantages of both of techniques.

This paper is structured as follows: After the introduction, the second part presents the topology of the system studied including the modelling of the turbine, the doubly fed induction generator, the power converters, the filter, the control part using the sliding mode tech-

niques. Then the smoothing power techniques are shown in the third section. The last section is dedicated to the simulation results, carried out using the Matlab/Simulink software, followed by a conclusion.

2. THE TOPOLOGY OF THE SYSTEM

The most suitable topology of the wind energy conversion system is the one based on the DFIG, which is directly connected to the grid from the stator, connected to the grid through two power converters from the wound rotor, a DC link placed among the converters as shown in figure 1.

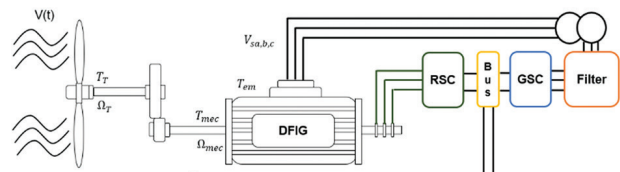


Fig.1. Block diagram of the wind energy converter system

2.1 THE MODELLING PARTS

2.1.1 The turbine modelling

The source of the wind energy conversion system is the kinetic energy of the wind. The latter is equivalent to an air mass displacement field characterized by a variable speed and a random trajectory applied to the turbine. It creates forces on the surfaces of its blades, which generates a rotational movement of the latter. It is an aerodynamic conversion.

The aerodynamic power expression is given by:

$$P_{a\acute{e}r} = \frac{1}{2} \rho S V^3 \quad (1)$$

According to betz's theory the turbine power P_t is given by:

$$P_T = P_{a\acute{e}r} C_p(\beta, \lambda) \quad (2)$$

C_p is a specific coefficient to each wind turbine.

The turbine torque is defined by:

$$T_T = \frac{P_T}{\Omega_T} \quad (3)$$

the gearbox is a speed adapter from that of the turbine to that of the generator. Its gain is given by:

$$G = \frac{T_T}{T_{mec}} = \frac{\Omega_{mec}}{\Omega_T} \quad (4)$$

Applying the fundamental relation of the dynamics, the generator tree is modeled by the following equation:

$$J \frac{d\Omega_{mec}}{dt} = \sum T = T_{mec} - T_{em} - T_{vis} \quad (5)$$

From the equations given above, we conclude the block diagram of the turbine given by figure 2.

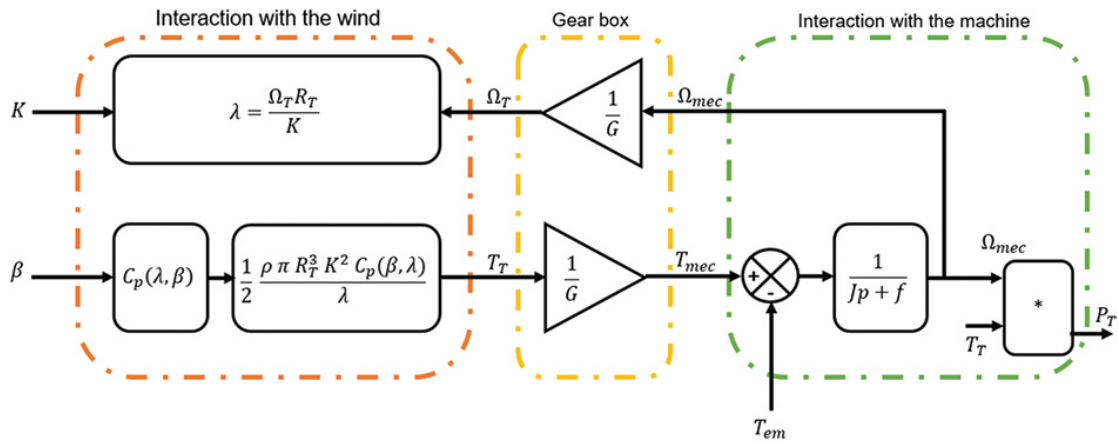


Fig. 2. Block diagram of the turbine

2.1.2 THE DFIG modelling

The electrical part modelling is needed after the modelling of the mechanical part, the first element to model is the DFIG.

Starting from the schematic representation of a DFIG in the three-phase reference widely presented in [9,10,11] and by adopting the hypothesis of a stator resistance R_s as negligible (given the power of the DFIG), the stator flux φ_s is constant (while V_s is constant) and oriented along the axis d [12,13,14] the machine's new equations are given by:

$$\begin{cases} V_{sd} = 0 \\ V_{sq} = V_s = \omega_s \varphi_s \\ V_{rd} = R_r I_{rd} + \frac{d\varphi_{rd}}{dt} - \omega_r \varphi_{rq} \\ V_{rq} = R_r I_{rq} + \frac{d\varphi_{rq}}{dt} + \omega_r \varphi_{rd} \end{cases} \quad (6)$$

And

$$\begin{cases} \varphi_{sd} = \varphi_s = L_s I_{sd} + M I_{rd} \\ 0 = L_s I_{sq} + M I_{rq} \\ \varphi_{rd} = L_r I_{rd} + M I_{sd} \\ \varphi_{rq} = L_r I_{rq} + M I_{sq} \end{cases} \quad (7)$$

The stator currents are given by the following system:

$$\begin{cases} I_{sd} = \frac{\varphi_s}{L_s} - \frac{M}{L_s} I_{rd} \\ I_{sq} = -\frac{M}{L_s} I_{rq} \end{cases} \quad (8)$$

The active and reactive powers become:

$$\begin{cases} P_s = V_{sq} I_{sq} = -\frac{M}{L_s} V_s I_{rq} \\ Q_s = V_{sd} I_{sd} = \frac{V_s \varphi_s}{L_s} - \frac{M V_s}{L_s} I_{rd} \end{cases} \quad (9)$$

by injecting the expression of the stator currents given by equation 9, into the equations of the rotor fluxes, we obtain:

$$\begin{cases} \varphi_{rd} = \left(L_r - \frac{M}{L_s}\right) I_{rd} + \frac{M \varphi_s}{L_s} = \left(L_r - \frac{M^2}{L_s}\right) I_{rd} + \frac{M V_s}{\omega_s L_s} \\ \varphi_{rq} = \left(L_r - \frac{M^2}{L_s}\right) I_{rq} \end{cases} \quad (10)$$

By injecting (10) into (6) a new system of direct and quadrature rotor voltages is obtained:

$$\begin{aligned} V_{rd} &= R_r I_{rd} + \left(L_r - \frac{M^2}{L_s}\right) \frac{dI_{rd}}{dt} - g \omega_s \left(L_r - \frac{M^2}{L_s}\right) I_{rq} \\ V_{rq} &= R_r I_{rq} + \left(L_r - \frac{M^2}{L_s}\right) \frac{dI_{rq}}{dt} + g \omega_s \left(L_r - \frac{M^2}{L_s}\right) I_{rd} + g \end{aligned} \quad (11)$$

2.1.3 The power converters and filter modelling

The DFIG's output is connected to the grid through two power converter as shown in the figure 1.

The simple voltages given at the output of the converter are [15,16,17]:

$$\begin{pmatrix} V_a \\ V_b \\ V_c \end{pmatrix} = \frac{E}{6} \begin{pmatrix} 2 & -1 & -1 \\ -1 & 2 & -1 \\ -1 & -1 & 2 \end{pmatrix} \begin{pmatrix} S_1 \\ S_2 \\ S_3 \end{pmatrix} \quad (12)$$

2.1.4 The DC link modelling

It consists of a capacitor C placed between the converters. It is governed by the following electrical equation:

$$\frac{dU_{dc}}{dt} = \frac{1}{C} (I_{GSC} - I_{RSC}) \quad (13)$$

2.1.5 The filter modelling

The filter is composed of a resistor R in series with an inductance L called respectively the total resistance and inductance of the line.

The line voltages are given by:

$$\begin{cases} V_{t1} = R I_{t1} + L \frac{dI_{t1}}{dt} + V_a \\ V_{t2} = R I_{t2} + L \frac{dI_{t2}}{dt} + V_b \\ V_{t3} = R I_{t3} + L \frac{dI_{t3}}{dt} + V_c \end{cases} \quad (14)$$

2.2 THE CONTROL PART

- The RSC's and FSC's Control

Different control techniques exist, control using PI correctors remains the most basic, backstepping and sliding mode are more efficient in terms of the produced energy quality.

The purpose of this paragraph is to synthesize a control law based on the sliding mode technique applied to the rotor and flywheel side converter to control the active and reactive powers generated by the DFIG at the desired values. This technique is detailed in [1, 18,20].

The model of the DFIG's control used is the oriented stator flux, the electrical quantities which are all expressed in a fixed reference frame linked to the stator. (d, q). eq (6,7,8,9).

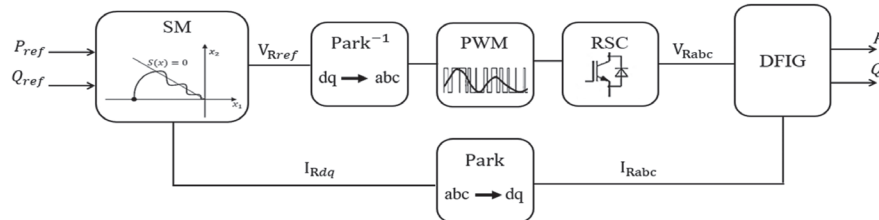


Fig. 3. Principal block diagram of the sliding mode control

The block diagram of the control used is illustrated in figure 3, it is a control of the active and reactive power through the rotor currents, by actuating the rotor voltages, therefore the elaboration of the control law results by determining the expression of the reference voltages of the PWM block which controls the converter connected to the rotor of the DFIG.

2.2.1 The Switching Surface Choice

The sliding mode technique uses a switching surface on which the control will slide.

The switching surface's expression is as follows:

$$s(P) = I_{rq}^{ref} - I_{rq} \quad (16)$$

$$s(Q) = I_{rd}^{ref} - I_{rd} \quad (17)$$

From equation 15 we can define

$$\begin{aligned} I_{rq}^{ref} &= -\frac{L_s}{MV_s} p^{ref} \\ I_{rd}^{ref} &= -\frac{L_s}{MV_s} Q^{ref} + \frac{V_s}{\omega_s M} \end{aligned} \quad (18)$$

2.2.2 Calculation of the vector's control

The vector's control is given by the rotor voltages as shown in figure 3. The sliding mode is performed provided that the Lyapunov attractiveness relation is less than zero, so the surfaces' derivatives are given by:

$$\dot{s}(P) = \dot{I}_{rq}^{ref} - \dot{I}_{rq} \quad (19)$$

$$\dot{s}(Q) = \dot{I}_{rd}^{ref} - \dot{I}_{rd} \quad (20)$$

By replacing the currents derivatives of the equation 18 by their expressions (equation: 11) we have:

$$\dot{s}(P) = \left(-\frac{L_s}{MV_s} \dot{p}^{ref} - \frac{1}{\sigma L_r} \left(V_{rq} - R_r I_{rq} - g w_s L_r I_{rd} - g \frac{MV_s}{L_s} \right) \right) \quad (21)$$

The sliding command used is given by the sign function, as specified in the following equation:

The powers' control is equivalent to the rotor currents' control, so we deduce the following rotor currents expressions.

$$\begin{aligned} I_{rq} &= -\frac{L_s}{MV_s} P \\ I_{rd} &= -\frac{L_s}{MV_s} Q + \frac{V_s}{\omega_s M} \end{aligned} \quad (15)$$

$$\dot{s}(P) = -v_1 \text{sgn}(s(P)) \quad (22)$$

$$\begin{aligned} V_{rq} &= -\frac{L_s \sigma L_r}{MV_s} \dot{p}^{ref} + R_r I_{rq} + \\ &g w_s L_r \sigma I_{rd} + g \frac{MV_s}{L_s} + L_r \sigma v_1 \text{sgn}(s(P)) \end{aligned} \quad (23)$$

$$V_{rq_{eq}} = -\frac{L_s \sigma L_r}{MV_s} \dot{p}^{ref} + R_r I_{rq} + g w_s L_r \sigma I_{rd} + g \frac{MV_s}{L_s} \quad (24)$$

$$V_{rq_{com}} = L_r \sigma v_1 \text{sgn}(s(P)) \quad (25)$$

we have to redo the same calculation to find the control vector of the reactive power.

$$V_{rd_{eq}} = L_r \sigma \left(-\frac{L_s}{MV_s} \dot{Q}^{ref} + \frac{V_s}{M w_s} \right) + R_r I_{rd} - g w_s L_r \sigma I_{rq} \quad (26)$$

$$V_{rd_{com}} = L_r \sigma v_2 \text{sgn}(s(Q)) \quad (27)$$

v_1 and v_2 are constants determined using the genetic algorithm in order to have the closest response to its reference.

The sliding mode block illustrated by figure 4 is detailed in figure 5.

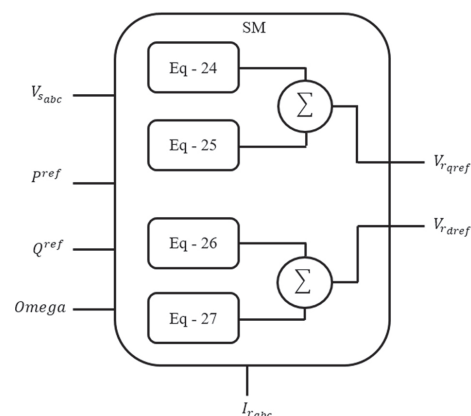


Fig. 4. Vector's control block diagram of the sliding mode

2.2.3 The GSC's control

The purpose of the grid side converter's control is to control two large quantities; therefore, the control can be divided into two parts:

Controlling the grid side converter consists in:

- Regulating the DC bus voltage to follow its reference.
- Keeping the reactive power's reference to zero to ensure a unit power factor.

In fact, in the same way and using the equations 13 and 14, we elaborate a control law based on the SM to control the GSC.

3. THE ACTIVE POWER SMOOTHING TECHNIQUES

The active power smoothing techniques discussed in this paper are: the use of an ESS and the blades orientation system. The first one consists on storing the active power in case of excess or recovering it if necessary. The second one limits power only in case of excess.

3.1 FLYWHEEL ENERGY STORAGE SYSTEM

Storing electrical energy involves converting it into another form and then storing it [21,22,23]. The inertial energy storage system is based on a dual power machine that converts electrical power into inertial power which is then stored in a flywheel as shown in the figure 5.

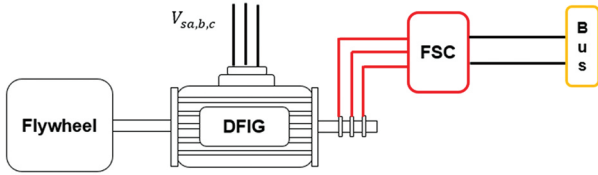


Fig.5. Block diagram of the flywheel energy storage system

Wind turbines are considered as negative loads for the electrical grid, because they do not consume electrical energy so the active power produced by the overall system is negative, its expression is given by:

$$P_{grid} = P_{DFIG} + P_{ESS} \quad (28)$$

The P_{DFIG} is the power of the wind converted by the DFIG into electrical power, it presents several fluctuations because of the source. P_{ESS} is the power of the storage system, the exchange of this power is done in both directions, towards the storage system in the event that there are losses of the produced power in relation to the setpoint (we speak of load of the flywheel, or from the storage system in the event of a need to reach the setpoint (discharge of the flywheel) as shown in the figure 6.

The ESS active power's expression is given by:

$$P_{ESS} = P_{grid,ref} - P_{DFIG} \quad (29)$$

$$E_{ESS} = E_{ESS0} + \int P_{ESS} dt \quad (30)$$

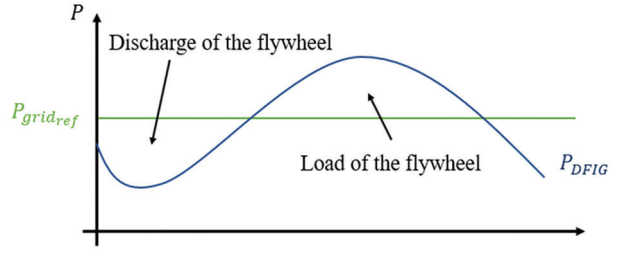


Fig. 6. charge and discharge of the flywheel depending on the produced power and the desired power

The literature has proposed several configurations of the FESS [24,25,26,27,28]. In this paper, the electric motor used to drive the flywheel is a DFIG. The energy stored in a flywheel is expressed by:

$$E_{ESS} = 0.5 \cdot J_{ESS} \cdot \Omega_{ESS}^2 \quad (31)$$

$$\Omega_{ESS} = \sqrt{\frac{2 \cdot E_{ESS}}{J_{ESS}}} \quad (32)$$

3.2 THE BLADES' ORIENTATION SYSTEM

It is a system which acts on the pitch angle of the blades to a reference value β_{ref} desired, this angle's choice generally used to adjust the speed of the turbine and the mechanical power generated. adjusting blades, the turbine's performances are modified more precisely the power coefficient. The blades are facing the wind at low wind speed and tilt for high wind speeds to reduce the power coefficient [9]. Generally, the blade orientation system is approximated by a transfer function of 1st order with a time constant T_{β} .

The aim is to limit and maintain the produced power at its nominal value P_{nom} in order to preserve all the elements of the conversion chain around this power. The pitch control makes it possible to reduce the power coefficient and thus limit thus the converted power afterwards the produced one [29,30].

To obtain the reference angle β_{ref} we correct the generated power P_T to its reference P_{ref} using a PI regulator.

The whole blades' orientation system is shown in figure 7.

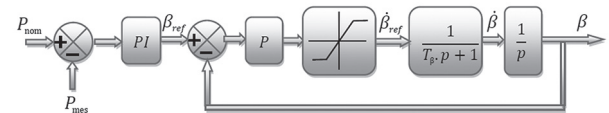


Fig. 7. The block diagram of the pitch control

4. THE SIMULATION RESULTS

The simulation studies are carried out with the characteristics of the system presented in the appendix. All the simulations are run with the same wind profile with an average speed of 8 m / s for a duration of 50 s, as shown in figure 8.

The figure 9 shows the stator voltage, which is a balanced three-phase system of frequency 50Hz and effective value 400V.

For this first part of simulation, we present the results of the solution based on the use of an ESS. Figure 12 shows the produced electric power P_{DFIG} which has the same form of fluctuations present in the wind, since in the equation 1 the power captured by the turbine is proportional to the cube of the wind. And always in the same figure, we have the reference power $P_{gridref}$

The utility of the ESS is to provide power when needed or to store it in case of excess, as shown in figure 13. From 8 to 9s the produced power P_{DFIG} is less than the desired power $P_{gridref}$. The ESS produced the difference power, in the interval [9s, 10s] P_{DFIG} is greater than the power $P_{gridref}$. The difference is stored as kinetic energy, as shown in figure 14, clearly sees between 8 and 9s that the kinetic energy increases following the loading of the flywheel.

The total active power injected into the grid faithfully follows its reference $P_{gridref}$ except a very small oscillations as shown in figure 15, while the one using the pitch control technique presents some important fluctuations as shown in figure 18. More precisely, the pitch control technique limits the power so as not to exceed its reference, if on the other hand the power is lower than its reference, it unchanged. So, this technique keeps the power fluctuations lower than the reference and eliminates the higher ones.

In figure 19 we can see the two powers injected into the grid using the two techniques explained previously, the goal is to follow $P_{gridref}$. Note that the pitch control technique is less efficient compared to the use of the ESS, power P_{ESS} which is well smoothed.

Figures 10 and 16 show the stator's currents. Comparing the two, we notice that the technique using the ESS gives a current which reaches very large values, unlike the current of the second technique which remains limited. The same observation for the rotor's currents shown in figure 11 and 17.

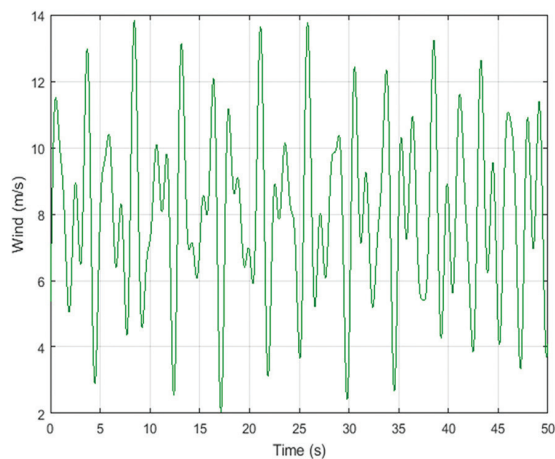


Fig. 8. The wind profile

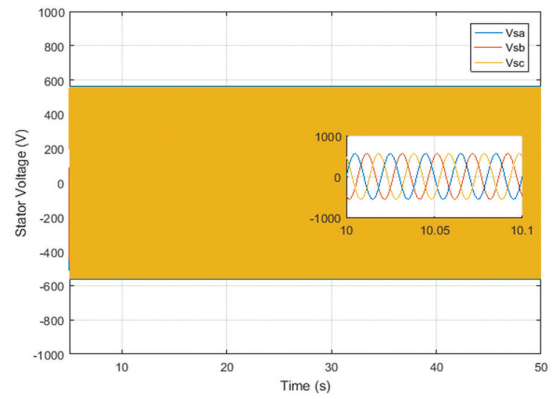


Fig. 9. The stator's Voltages

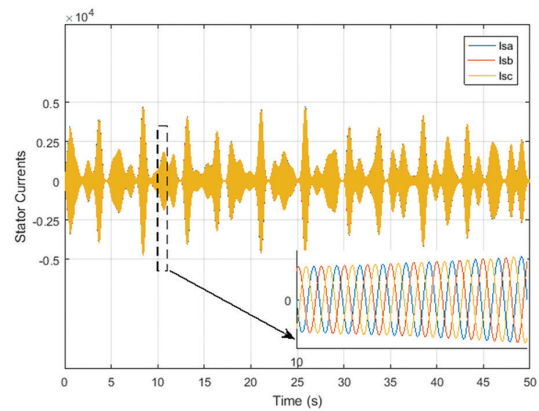


Fig. 10. The stator's currents using the ESS

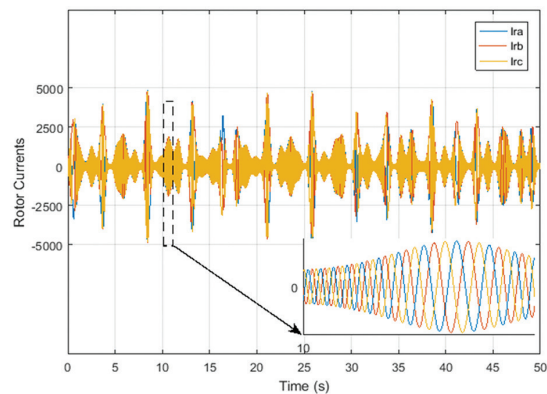


Fig. 11. The rotor's currents using the ESS

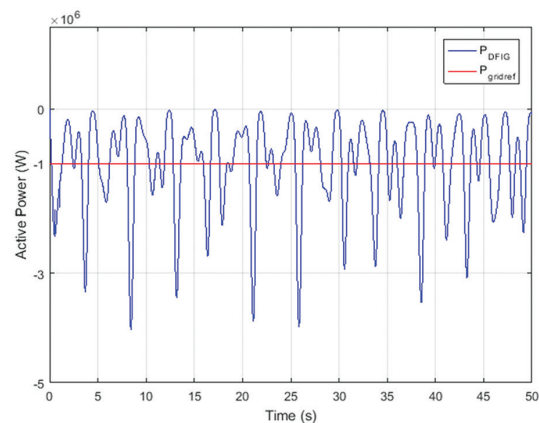


Fig. 12. The DFIG's active power with the grid reference one

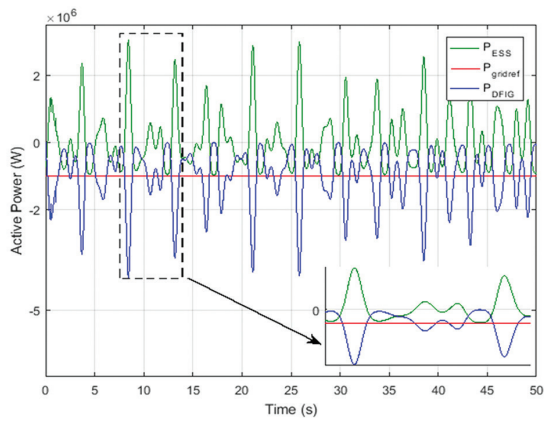


Fig. 13. The ESS's active power

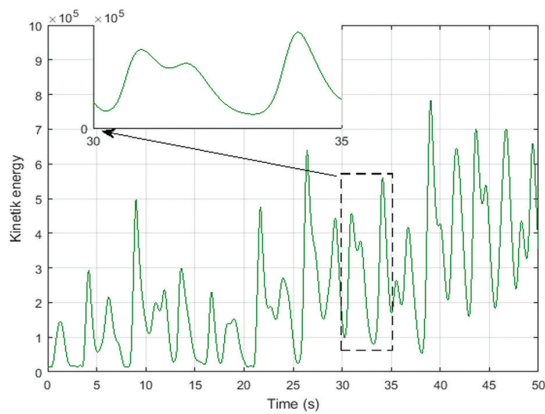


Fig. 14. The flywheel's Kinetic energy

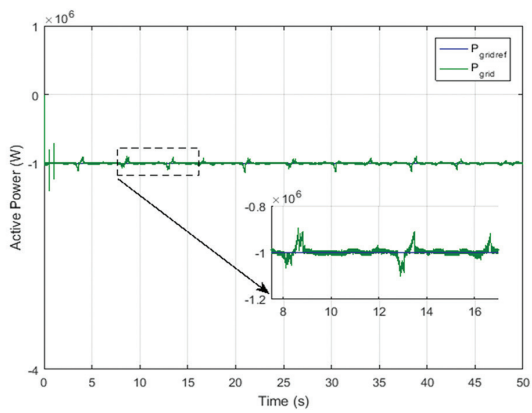


Fig. 15. The active power injected in the grid and its reference using the ESS

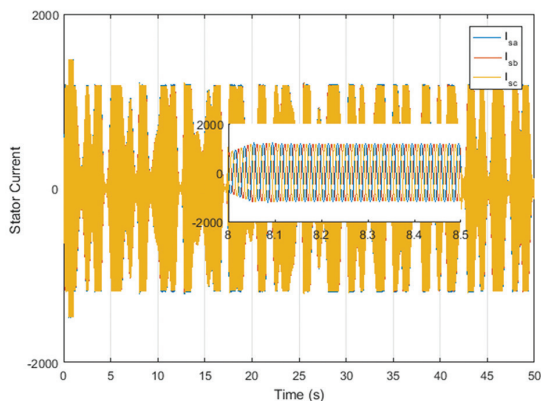


Fig. 16. The stator's current using the pitch control

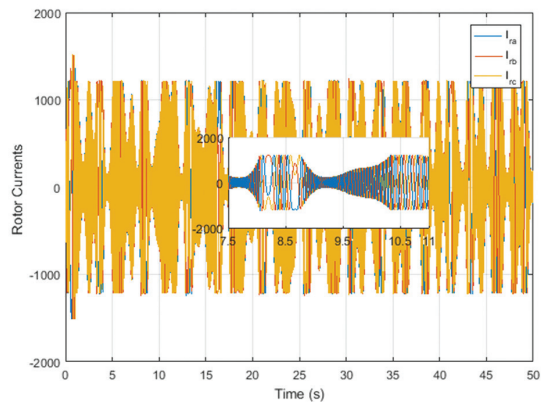


Fig. 17. The rotor's currents using the pitch control

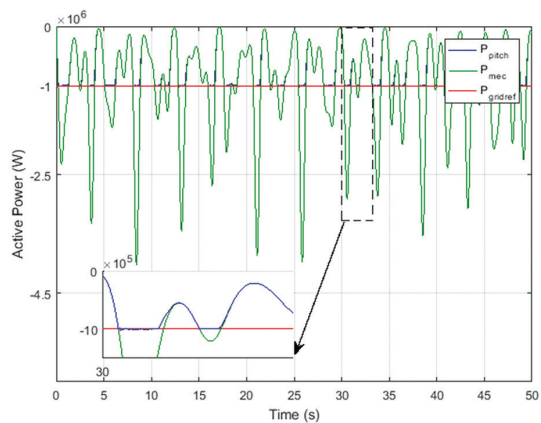


Fig. 18. The active power injected in the grid and its reference using the pitch control

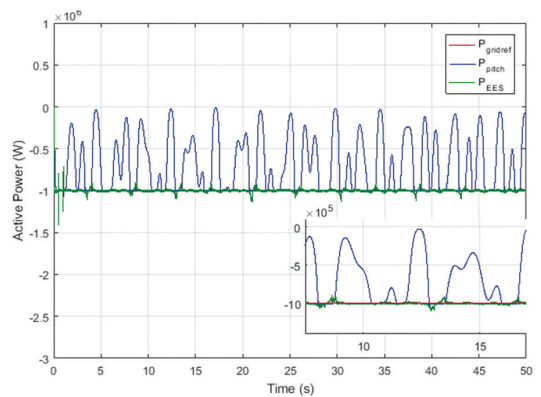


Fig. 19. The produced power injected in the grid

5. CONCLUSION

The purpose of this study is to smooth the produced power of the WECS, so that when injected into the grid it's more stable for the wind fluctuations. The work done in this paper consists of making a comparison between two power smoothing techniques, which are the ESS and the pitch control. First a modelling of all the parts of the conversion chain was made. Then, in order to smooth the injected power into the grid, the first method consisted of the use of a second DFIG associated with a flywheel for the storage device. There-

fore, in the case of excess power, it is stored, recovered in the reverse case. As a control technique of the flywheel side converter, the sliding mode was used, when the second technique is the pitch control, which consists of orienting the blades' angle β according to the power's reference. The simulation results showed that the use of an ESS gives a smoother power but with peaks of rotor and stator currents, whereas in pitch control, the rotor and stator currents are limited but the injected power is not smooth enough. Otherwise, if we try to smooth the power, the use of an ESS and resizing the converters' components withstanding the peaks of the currents is needed, however the use of the second solution limits the currents but is not efficient for the power smoothing.

6. APPENDIX

DFIG's Parameter

$P_n=300$ Kw, $f=50$ Hz, $R_s=8.9$ m Ω resistor, $R_r=13.7$ m Ω , $L_s=12.9$ mH, $L_r=12.7$ mH, $L_m=M=12.672$ mH, $\sigma=0.0198$, $P=2$

Filter and grid parameters

$L=0.005$ H, $R=0.25$ Ω , $C=4400$ μ F

The wind-swept turbine surface's expression:

$$S = \pi R_T^2$$

The Aerodynamic coefficient's expression:

$$C_p(\lambda, \beta) = 0.5176 \left(\frac{116}{\lambda_i} - 0.4\beta - 5 \right) e^{-\frac{21}{\lambda_i}} + 0.0068 \lambda$$

$$\text{Where } \left\{ \begin{array}{l} \lambda_i = \left(\frac{1}{\lambda + 0.08\beta} - \frac{0.035}{\beta^3 + 1} \right)^{-1} \\ \lambda = \frac{\Omega_T R_T}{v} \end{array} \right.$$

The total inertia's expression:

$$J = (J_{Turbine}/G^2) + J_{generator}$$

The viscous friction torque's expression:

$$T_{vis} = f \Omega_{mec}$$

7. NOMENCLATURE

Ω_T : Turbine speed.

v : the wind profil.

Ω_{mec} : Mecanic speed.

T_T : Turbine torque.

T_{mec} : Mecanic torque.

ρ : Air density;

S : Wind-swept turbine surface.

$C_p(\beta, \lambda)$: Aerodynamic efficiency of the turbine often referred to as a power factor.

J : The total inertia

T_{vis} : The viscous friction torque.

J_{ESS} : The ESS inertia.

V_{sd}, V_{sq} : the dq axis stator voltages.

I_{sd}, I_{sq} : the dq axis stator current.

$\varphi_{sd}, \varphi_{sq}$: the Stator d and q axis fluxes.

V_{rd}, V_{rq} : the dq axis rotor voltages.

I_{rd}, I_{rq} : the dq axis rotor current.

$\varphi_{rd}, \varphi_{rq}$: the rotor d and q axis fluxes.

R_s, R_r : stator and rotor resistances.

L_s, L_r : stator and rotor inductance.

M : Mutuel inductance.

ω_s, ω_r : the supply and rotor angular frequency.

$V_{a,b,c}$: are the single voltages from the converter.

U_{dc}, E : is the DC voltage that comes from the DC link.

$V_{\ell 1,2,3}$ are the three-phase system of the source (the grid).

$I_{\ell 1,2,3}$: are the line currents coming from the source.

$I_{GSC}, I_{RSC}, I_{FSC}$: are respectively the current at the converter outputs on the grid side, rotor side and the flywheel side converter.

P, Q : active and reactive power.

P_{grid} : The grid's active power.

P_{DFIG} : the DFIG's active power.

P_{ESS} : The active power of the energy storage system.

$S_{1,2,3}$: the PWM's commands.

8. REFERENCES

- [1] H. Elaimani, A. Essadki, N. Elmouhi, R. Chakib, "Comparative Study of the Grid Side Converter's Control during a Voltage Dip", Journal of Energy, Vol. 2020, 2020, pp. 1–11.
- [2] L. Jerbi, L. Krichen, A. Ouali, "A fuzzy logic supervisor for active and reactive power control of a variable speed wind energy conversion system associated to a flywheel storage system", Electric Power Systems Research, Vol. 79, No. 6, 2009, pp. 919–925.
- [3] M. Nadour, A. Essadki, T. Nasser, M. Fdaili, "Robust coordinated control using backstepping of flywheel energy storage system and DFIG for power smoothing in wind power plants", International Journal of Power Electronics and Drive Systems, Vol. 10, No. 2, 2019, pp. 1110–1122.

- [4] S. Ghosh and S. Kamalasan, "An integrated dynamic modeling and adaptive controller approach for flywheel augmented DFIG based wind system", *IEEE Transactions on Power Systems*, Vol. 32, No. 3, 2017, pp. 2161–2171.
- [5] S. A. Belfedhal, E. M. Berkouk, Y. Meslem, Y. Soufi, "Modeling and control of wind power conversion system with a flywheel energy storage system and compensation of reactive power", *International Journal of Renewable Energy Research*, Vol. 2, No. 3, 2012, pp. 528–534.
- [6] F. Díaz-González, A. Sumper, O. Gomis-Bellmunt, F. D. Bianchi, "Energy management of flywheel-based energy storage device for wind power smoothing", *Applied Energy*, Vol. 110, 2013, pp. 207–219.
- [7] X. Luo, J. Wang, M. Dooner, J. Clarke, "Overview of current development in electrical energy storage technologies and the application potential in power system operation", *Applied Energy*, Vol. 137, 2015, pp. 511–536.
- [8] G.-O. Cimuca, "Système inertiel de stockage d'énergie associé aux générateurs éoliens", 2005.
- [9] R. Riyadh, "Contrôle des puissances générées par un système éolien à vitesse variable basé sur une machine asynchrone double alimentée", 2016.
- [10] R. Chakib, "Commande avancée d'une éolienne à base de la MADA en vue de sa participation aux services système : réglage de fréquence, réglage de tension et tenue aux creux de tension", 2017.
- [11] M. Smaili, "Par modélisation et commande d'un aérogénérateur à machine asynchrone à double alimentation en vue de simulation des problèmes de cogénération", 2013.
- [12] H. Elaimani, A. Essadki, N. Elmouhi, R. Chakib, "Comparative Study of the Grid Side Converter's Control during a Voltage Dip", *Journal of Energy*, Vol. 2020, 2020, pp. 1–11.
- [13] R. Chakib, A. Essadki, M. Cherkaoui, "Active Disturbance Rejection Control for Wind System Based On a DFIG", *International Journal of Electrical and Computer Engineering*, Vol. 8, No. 8, 2014, pp. 1249–1258.
- [14] T. Ghennam, "Supervision d'une ferme éolienne pour son intégration dans la gestion d'un réseau électrique, Apports des convertisseurs multi niveaux au réglage des éoliennes à base de machine asynchrone double alimentation", Vol. 072, 2011, pp. 1–19.
- [15] Y. Djeriri, "Commande directe du couple et des puissances d'une MADA associée à un système éolien par les techniques de l'intelligence artificielle", 2015.
- [16] K. Belgacem, A. Mezouar, A. Massoum, "Sliding Mode Control of a Doubly-fed Induction Generator for Wind Energy Conversion", *International Journal of Scientific & Engineering Research*, Vol. 2013, No. 1, 2013, pp. 30–36.
- [17] B. Beltran, "High-Order Sliding Mode Control of a DFIG-Based Wind Turbine for Power Maximization and Grid Fault Tolerance", *Proceedings of the IEEE International Electric Machines and Drives Conference*, Miami, FL, USA, 3-6 May 2009, pp. 183–189.
- [18] M. Elazzaoui, H. Mahmoudi, K. Boudaraia, C. Ed-dahmani, "FPGA Implementation of Super Twisting Sliding Mode Control of the Doubly Fed Induction Generator", *Proceedings of the 14th International Multi-Conference on Systems, Signals & Devices*, Marrakech, Morocco, 28-31 March 2017.
- [19] H. Elaimani, A. Essadki, "The study of the PI controller and the sliding mode of DFIG used in a WECS", *Proceedings of the International Renewable and Sustainable Energy Conference*, Tangier, Morocco, 4-7 December 2017.
- [20] H. Elaimani, A. Essadki, N. Elmouhi, R. Chakib, "The Modified Sliding Mode Control of a Doubly Fed Induction Generator for Wind Energy Conversion During a Voltage Dip", *Proceedings of the International Conference on Wireless Technologies, Embedded and Intelligent Systems*, Fez, Morocco, 3-4 April 2019.
- [21] L. Jerbi, L. Krichen, A. Ouali, "A fuzzy logic supervisor for active and reactive power control of a variable speed wind energy conversion system associated to a flywheel storage system", *Electric Power Systems Research*, Vol. 79, No. 6, 2009, pp. 919–925.
- [22] X. Luo, J. Wang, M. Dooner, J. Clarke, "Overview of current development in electrical energy storage technologies and the application potential in power system operation", *Applied Energy*, Vol. 137, 2015, pp. 511–536.

- [23] M. Nadour, A. Essadki, T. Nasser, M. Fdaili, "Robust coordinated control using backstepping of flywheel energy storage system and DFIG for power smoothing in wind power plants", *International Journal of Power Electronics and Drive Systems*, Vol. 10, No. 2, 2019, pp. 1110–1122.
- [24] S. Ghosh and S. Kamalasan, "An integrated dynamic modeling and adaptive controller approach for flywheel augmented DFIG based wind system", *IEEE Transactions on Power Systems*, Vol. 32, No. 3, 2017, pp. 2161–2171.
- [25] S. A. Belfedhal, E. M. Berkouk, Y. Meslem, Y. Soufi, "Modeling and control of wind power conversion system with a flywheel energy storage system and compensation of reactive power", *International Journal of Renewable Energy Research*, Vol. 2, No. 3, 2012, pp. 528–534.
- [26] F. Díaz-González, A. Sumper, O. Gomis-Bellmunt, F. D. Bianchi, "Energy management of flywheel-based energy storage device for wind power smoothing", *Applied Energy*, Vol. 110, 2013, pp. 207–219.
- [27] G.-O. Cimuca, "Système inertiel de stockage d'énergie associé aux générateurs éoliens", 2005.
- [28] B. Hamane, M. L. Doumbia, M. Bouhamida, A. Draou, H. Chaoui, M. Benghanem, "Comparative Study of PI, RST, Sliding Mode and Fuzzy Supervisory Controllers for DFIG based Wind Energy Conversion System", *International Journal of Renewable Energy Research*, Vol. 5, No. 4, 2015, pp. 1174–1185.
- [29] S. ELAimani, "Modelisation de differentes technologies d'éoliennes integrees dans un reseau de moyenne tension", 2004.
- [30] N. El Ouanjli, M. Taoussi, A. Derouich, A. Chebabhi, A. El Ghzizal, B. Boussofi "High Performance Direct Torque Control of Doubly Fed Induction Motor using Fuzzy Logic", *Gazi university journal of science*, Vol. 31, No. 2, 2018, pp. 532-542.
- [31] N. El Ouanjli, A. Derouich, A. El Gzizal, Y. El Mourabet, B. Bossoufi, M. Taoussi, "Contribution to the performance improvement of Doubly Fed Induction Machine functioning in motor mode by the DTC control", *International Journal Power Electronics and Drive System*, Vol.8, No.3, 2017, pp. 1117-1127.

INTERNATIONAL JOURNAL OF ELECTRICAL AND COMPUTER ENGINEERING SYSTEMS

Published by Faculty of Electrical Engineering, Computer Science and Information Technology Osijek,
Josip Juraj Strossmayer University of Osijek, Croatia.

About this Journal

The International Journal of Electrical and Computer Engineering Systems publishes original research in the form of full papers, case studies, reviews and surveys. It covers theory and application of electrical and computer engineering, synergy of computer systems and computational methods with electrical and electronic systems, as well as interdisciplinary research.

Topics of interest include, but are not limited to:

- Power systems
- Renewable electricity production
- Power electronics
- Electrical drives
- Industrial electronics
- Communication systems
- Advanced modulation techniques
- RFID devices and systems
- Signal and data processing
- Image processing
- Multimedia systems
- Microelectronics
- Instrumentation and measurement
- Control systems
- Robotics
- Modeling and simulation
- Modern computer architectures
- Computer networks
- Embedded systems
- High-performance computing
- Parallel and distributed computer systems
- Human-computer systems
- Intelligent systems
- Multi-agent and holonic systems
- Real-time systems
- Software engineering
- Internet and web applications and systems
- Applications of computer systems in engineering and related disciplines
- Mathematical models of engineering systems
- Engineering management
- Engineering education

Paper Submission

Authors are invited to submit original, unpublished research papers that are not being considered by another journal or any other publisher. Manuscripts must be submitted in doc, docx, rtf or pdf format, and limited to 30 one-column double-spaced pages. All figures and tables must be cited and placed in the body of the paper. Provide contact information of all authors and designate the corresponding author who should submit the manuscript to <https://ijeces.ferit.hr>. The corresponding author is responsible for ensuring that the article's publication has been approved by all coauthors and by the institutions of the authors if required. All enquiries concerning the publication of accepted papers should be sent to ijeces@ferit.hr.

The following information should be included in the submission:

- paper title;
- full name of each author;
- full institutional mailing addresses;
- e-mail addresses of each author;
- abstract (should be self-contained and not exceed 150 words). Introduction should have no subheadings;
- manuscript should contain one to five alphabetically ordered keywords;
- all abbreviations used in the manuscript should be explained by first appearance;
- all acknowledgments should be included at the end of the paper;
- authors are responsible for ensuring that the information in each reference is complete and accurate. All references must be numbered consecutively and citations of references in text should be identified using numbers in square brackets. All references should be cited within the text;
- each figure should be integrated in the text and cited in a consecutive order. Upon acceptance of the paper, each figure should be of high quality in one of the following formats: EPS, WMF, BMP and TIFF;
- corrected proofs must be returned to the publisher within 7 days of receipt.

Peer Review

All manuscripts are subject to peer review and must meet academic standards. Submissions will be first considered by an editor-

in-chief and if not rejected right away, then they will be reviewed by anonymous reviewers. The submitting author will be asked to provide the names of 5 proposed reviewers including their e-mail addresses. The proposed reviewers should be in the research field of the manuscript. They should not be affiliated to the same institution of the manuscript author(s) and should not have had any collaboration with any of the authors during the last 3 years.

Author Benefits

The corresponding author will be provided with a .pdf file of the article or alternatively one hardcopy of the journal free of charge.

Units of Measurement

Units of measurement should be presented simply and concisely using System International (SI) units.

Bibliographic Information

Commenced in 2010.
ISSN: 1847-6996
e-ISSN: 1847-7003

Published: semiannually

Copyright

Authors of the International Journal of Electrical and Computer Engineering Systems must transfer copyright to the publisher in written form.

Subscription Information

The annual subscription rate is 50€ for individuals, 25€ for students and 150€ for libraries.

Postal Address

Faculty of Electrical Engineering,
Computer Science and Information Technology Osijek,
Josip Juraj Strossmayer University of Osijek, Croatia
Kneza Trpimira 2b
31000 Osijek, Croatia

IJECES Copyright Transfer Form

(Please, read this carefully)

This form is intended for all accepted material submitted to the IJECES journal and must accompany any such material before publication.

TITLE OF ARTICLE (hereinafter referred to as "the Work"):

COMPLETE LIST OF AUTHORS:

The undersigned hereby assigns to the IJECES all rights under copyright that may exist in and to the above Work, and any revised or expanded works submitted to the IJECES by the undersigned based on the Work. The undersigned hereby warrants that the Work is original and that he/she is the author of the complete Work and all incorporated parts of the Work. Otherwise he/she warrants that necessary permissions have been obtained for those parts of works originating from other authors or publishers.

Authors retain all proprietary rights in any process or procedure described in the Work. Authors may reproduce or authorize others to reproduce the Work or derivative works for the author's personal use or for company use, provided that the source and the IJECES copyright notice are indicated, the copies are not used in any way that implies IJECES endorsement of a product or service of any author, and the copies themselves are not offered for sale. In the case of a Work performed under a special government contract or grant, the IJECES recognizes that the government has royalty-free permission to reproduce all or portions of the Work, and to authorize others to do so, for official government purposes only, if the contract/grant so requires. For all uses not covered previously, authors must ask for permission from the IJECES to reproduce or authorize the reproduction of the Work or material extracted from the Work. Although authors are permitted to re-use all or portions of the Work in other works, this excludes granting third-party requests for reprinting, republishing, or other types of re-use. The IJECES must handle all such third-party requests. The IJECES distributes its publication by various means and media. It also abstracts and may translate its publications, and articles contained therein, for inclusion in various collections, databases and other publications. The IJECES publisher requires that the consent of the first-named author be sought as a condition to granting reprint or republication rights to others or for permitting use of a Work for promotion or marketing purposes. If you are employed and prepared the Work on a subject within the scope of your employment, the copyright in the Work belongs to your employer as a work-for-hire. In that case, the IJECES publisher assumes that when you sign this Form, you are authorized to do so by your employer and that your employer has consented to the transfer of copyright, to the representation and warranty of publication rights, and to all other terms and conditions of this Form. If such authorization and consent has not been given to you, an authorized representative of your employer should sign this Form as the Author.

Authors of IJECES journal articles and other material must ensure that their Work meets originality, authorship, author responsibilities and author misconduct requirements. It is the responsibility of the authors, not the IJECES publisher, to determine whether disclosure of their material requires the prior consent of other parties and, if so, to obtain it.

- The undersigned represents that he/she has the authority to make and execute this assignment.
- For jointly authored Works, all joint authors should sign, or one of the authors should sign as authorized agent for the others.
- The undersigned agrees to indemnify and hold harmless the IJECES publisher from any damage or expense that may arise in the event of a breach of any of the warranties set forth above.

Author/Authorized Agent

Date

CONTACT

International Journal of Electrical and Computer Engineering Systems (IJECES)
Faculty of Electrical Engineering, Computer Science and Information Technology Osijek
Josip Juraj Strossmayer University of Osijek
Kneza Trpimira 2b
31000 Osijek, Croatia
Phone: +38531224600,
Fax: +38531224605,
e-mail: ijeces@ferit.hr